

Abstract

This work investigates the effect of anisotropy in interface energy on orientation selection during repeated nucleation in the polycrystalline film growth and the implications for the formation of crystallographic texture. For this purpose, a methodology was developed, which allowed to obtain the nucleation probability as function of the substrate and nucleus orientation. For every pair of these orientations, the nucleation probability was derived from the equilibrium stable shape of the nucleus at those conditions. In order to determine the arbitrarily oriented nucleus shape, a multi-phase field model incorporating anisotropic interface energy was extensively developed.

Multiple model variants were developed and methodology modified several times to solve various difficulties emerging due to inherent limitations of the models. Own solver for the governing equations was written in MATLAB. Two model-independent benchmark problems were developed to quantitatively compare performance of the developed models in terms of how they reproduced a) the anisotropic curvature driving force and b) the anisotropic curvature driving force when combined with strong anisotropy in kinetic coefficient. In both cases the system consisted of a shrinking grain with a well-defined shape (Wulff shape in a) and circle in b)). Even though the models were comparably consistent in simulations of shrinking Wulff shapes and circles, an additional benchmark problem concerning triple junction angles revealed thermodynamic inconsistency in two of the three models, causing them to be reliable only in isotropic or weakly anisotropic systems.

Analytic solution to the geometric problem was found, which allowed to implement a simpler and more efficient algorithm. So-called shape factor-orientation maps were constructed with high resolution and were used as input in a Monte Carlo simulation of growing polycrystal to demonstrate how the nucleation with anisotropic interface energy may affect the course of texture evolution. New modes of texture evolution were identified and the insight was used to qualitatively explain an experimentally observed peculiar texture evolution in electrodeposited nickel.

Contents

Abstract	a
Contents	c
1 Introduction	1
1.1 General introduction	1
1.2 Textures in coatings and interface energy anisotropy	2
1.3 TODO Goals of the thesis	3
2 Particles with anisotropic interface energy	5
2.1 Isolated particle with anisotropic interface energy	5
2.2 Particle with anisotropic interface energy on a plane (Winterbottom construction)	9
2.3 Inverted solution in Winterbottom construction	11
2.4 Contact point stability	13
2.5 Selected geometric properties of Wulff shape	14
2.6 Shrinkage rate of a Wulff shape	15
2.7 Summary and the author’s contribution	16
3 Phase field method	17
3.1 General introduction	17
3.2 Allen-Cahn equation for two-phase system	18
3.3 Allen-Cahn equation for two-phase system including anisotropic interface energy	21
3.3.1 Fundamentals	21
3.3.2 Challenges and limitations	23
3.4 Allen-Cahn equations for multi-phase systems	24
3.4.1 Historical context	24
3.4.2 Challenges and limitations	25
3.5 Benchmarking of phase field models	26

4	Extended multi-phase field model	29
4.1	Introduction	30
4.2	Isotropic model	31
4.3	Anisotropic model and parameters assignment strategies	32
4.3.1	Systems with pair-wise isotropic IE	32
4.3.2	Systems with inclination-dependent interface energy . .	34
4.3.3	Interface profiles in different models	38
4.4	General Neumann boundary conditions to control interface inclination at domain boundary	39
4.5	Volume conserving multi phase field models	41
4.5.1	Fictitious concentration field	41
4.6	Summary and the author's contribution	43
5	Phase field model benchmarking	45
5.1	Introduction	45
5.2	Numerical implementation	46
5.3	Methodology	48
5.3.1	Used anisotropy function and its Wulff shape	51
5.3.2	Quantifying the match in shape	51
5.3.3	Quantifying match in shrinkage rate	52
5.3.4	Wulff shape	52
5.3.5	Kinetically compensated anisotropic circle shrinkage . .	53
5.3.6	Triple junction angles	54
5.4	Results	55
5.4.1	Wulff shapes	55
5.4.2	Kinetically compensated anisotropic circle shrinkage . .	58
5.4.3	Equilibrium triple junction angles	60
5.5	Conclusions	61
6	Nucleation probability assessment - a phase field methodology	63
6.1	Introduction	63
6.2	Some fundamentals	64
6.3	Methodology	65
6.4	Numerical implementation	67
6.5	Validations	68
6.5.1	Tilted straight line	68
6.6	Results	69
6.6.1	Particle on a plane (isotropic interface energy)	70
6.6.2	Particle on a grain boundary (isotropic interface energy)	72
6.7	TODO Conclusion	74
7	Analytic nucleation probability assessment and Monte Carlo simulations	77

7.1	Introduction	77
7.1.1	Terminology in heterogeneous nucleation	78
7.1.2	Heterogeneous spatial nucleation and shape factor . . .	78
7.2	Nucleation probability assessment	81
7.2.1	Problem statement	81
7.2.2	Stability as function of the bottom grain orientation . .	83
7.2.3	Shape factor-orientation maps	83
7.3	Monte Carlo simulations	86
7.3.1	Algorithm description	86
7.3.2	Validation of anisotropic growth	90
7.3.3	Methodology	91
7.3.4	Results	93
7.4	Comparison to experiment and discussion	97
7.5	Conclusion	99
8	Conclusion	101
8.1	TODO Conclusion	101
8.2	TODO Outlook	101
A	Functional derivative	103
B	Supporting derivations in Moelans' model	107
C	Model parameters determination - best practices	109
C.1	Polynomial expressions for determination of γ	109
C.2	IWvG	110
C.3	IWc	112
C.4	IWvK	113
D	Implementation of finite difference method	115
D.1	General information	115
D.2	Ghost nodes in Neumann boundary condition	116
D.2.1	Zero Neumann BCs	116
D.2.2	General Neumann BCs	116
D.3	First-order derivatives in FD	117
D.3.1	Periodic boundary conditions	117
D.3.2	Neumann boundary conditions	118
D.3.3	Mixed boundary conditions	119
D.4	Laplacian in 2D	119
D.4.1	Periodic boundary conditions	120
D.4.2	Neuman boundary conditions	121
D.4.3	Mixed boundary conditions	123
D.5	Anisotropic driving force terms	124

E	Volume conservation using Lagrange multipliers	127
E.1	Phase field equations under equality constraint - Lagrange multipliers	127
E.2	Lagrange multipliers for volume conservation in multi-phase field models	129
E.2.1	Concept - single conserved phase field	129
E.2.2	Multiple conserved phase fields	131
	List of publications	143

Chapter 1

Introduction

1.1 General introduction

Irrespective of the deposition method, it is known that the process parameters often have pronounced effect on crystallographic texture and microstructure of polycrystalline deposits. Evaporation, sputtering, chemical vapour deposition or electrodeposition are just examples of these methods. Each is tied with a unique combination of physical and chemical interactions at the interface between the deposit and parent phase. The as-deposited texture is the result of synergy of many factors. However, the anisotropy on the deposit/parent phase interface during the film growth certainly plays an important role.

Typically, nucleation in film deposition is studied as a phenomenon occurring on substrates, rather than on the deposit itself. However, there seems to be no obvious reason to neglect such an option, given the complicated anisotropy of grain boundary energy and local deposition conditions, varying possibly in both space and time.

Despite the fact, that the anisotropy in interface energy is widely accepted to be one of the fundamental texture-forming factors, its effect on the orientation selection in nucleation remains fundamentally unclear.

1.2 Textures in coatings and interface energy anisotropy

A widely accepted theory by Thompson [65] suggests that the texture in deposits is controlled by two main factors: minimization of interface energy and minimization of strain energy. The first favors growth of grains with low-energy interfaces facing the parent phase and the second aligns the grains in the deposit to accommodate the stress. The energy densities are explicitly expressed for an abstracted columnar microstructure and compared as functions of the film thickness. He concluded that thin enough deposits have the texture controlled by minimization of interface energy. Above certain thickness, the strain energy overtakes. Later, additional factors contributing to the strain energy were included in the theory [14], allowing sensible interpretation of textures observed in sputter-deposited CdTe and electrodeposited Cu, but the results of some others are in agreement with the theory as well [61, 62].

A more phenomenological work by Rasmussen et al. [58] studied Cu electrodeposits on crystalline and amorphous substrates and proposed that in electrodeposition, the two competing texture-forming factors are the influence of the substrate and that of deposition conditions. Through the film thickness, three zones are defined: A (substrate-controlled texture), B (mixed) and C (deposition-conditions-controlled texture). The effect of the substrate in zone A can be e.g. epitaxy or chemical reactions, in zone C the anisotropy modifications are believed to be due to specific adsorption of different species [4, 53]. A more recent study of Ni electrodeposition [2] investigated the texture evolution through thickness with microscopic detail and showed, that the transition zone B does not seem to always occur as a simple mixture of A and C.

Two different theories by Pangarov [55, 56] and Kozlov [30] suggested that the textures of the electrodeposits are originated in the anisotropy of the nucleation barrier (*work of formation*), but each used a different reasoning. Pangarov treated 2D nuclei only and made the work of formation depending exclusively on overpotential and lattice parameters. This theory was inconsistent with experimental observation of nuclei character as function of overpotential [9]. Kozlov studied the formation of initial texture on amorphous substrates in fcc metals by means of atomistic nucleation theory. Specifically, he computed the nucleation barriers and sizes of nuclei with three significant orientations. His prediction of initial $\langle 111 \rangle$ texture is in agreement with Thompson. It can thus be deduced, that in the initial stages of growth in fcc metals on amorphous substrates, both the nucleation and growth may lead to the same fiber texture by means of interface energy minimization.

In practice, the interface energy anisotropy or deposition rate anisotropy cannot

be measured directly during the deposition, which complicates the interpretation of the observed textures and microstructures. Additionally, the effect of the two above physical quantities on the polycrystalline deposit growth was shown to be equivalent in phase-field simulations to some extent [69]. It seems analogical to equilibrium Wulff shapes and kinetic Wulff shapes, which are geometrically similar [29]. However, this makes the fundamental discussion about how the growth is affected by interface anisotropy in general even more challenging, because the growth rate and interface energy are very different quantities, taking part in different processes. This highlights the utility of simulation tools, which allow to set the anisotropy in interface energy and kinetic coefficient independently, because in practice the individual effects may be hard or impossible to distinguish. Among such tools is (multi-)phase field method.

1.3 TODO Goals of the thesis

This thesis explores the effect of anisotropic interface energy on nucleation and growth of polycrystalline deposits in various simulation concepts. It is known that the anisotropy in interface energy affects the equilibrium stable shape of a particle (on a plane). Also, it is known that the nucleation probability is proportional to the particle area (in 3d to its volume).

The goals of the thesis are:

1. Develop a methodology which would allow comparison of nucleation probability of differently oriented nuclei on an arbitrarily oriented substrate in 2D
2. Create a program which will
 1. Develop a methodology to simulate the equilibrium stable shapes of particles with anisotropic interface energy on a plane using the multi-phase field method
 - 2.

A perspective approach for simulation of a growing film including nucleation is multi-phase field method, which allows inclusion of anisotropic interface energy, but also anisotropy of the kinetic coefficient (deposition rate).

The goal

An established multi-phase field method was extended so that the equilibrium stable shapes could be obtained.

Chapter 2

Particles with anisotropic interface energy

2.1 Isolated particle with anisotropic interface energy

It was already discovered in 1901, how to determine the stable equilibrium shape of a particle with crystalline anisotropy [73]. The chemical potential $\mu(\theta)$ must be constant along the surface of equilibrium shape [5]. Assuming that the surface is only under the influence of anisotropic capillary force, the chemical potential on the curved surface in 3D space depends on the local principal curvatures and interface energy anisotropy as follows from the Herring equation [24, 27]. In 2D the surfaces become curves and the expression for the chemical potential is simplified to

$$\mu(\theta) = \tilde{\sigma}(\theta)K, \quad (2.1)$$

with local interface normal angle θ and local curvature K . The interface stiffness $\tilde{\sigma}(\theta)$ is the thermodynamic driving force for the capillary motion and the local curvature κ is the thermodynamic coordinate. The interface stiffness is

$$\tilde{\sigma}(\theta) = \sigma_0[h(\theta) + h''(\theta)], \quad (2.2)$$

where $h(\theta)$ and $h(\theta)''$ stand for the anisotropy function and its second derivative, respectively. The anisotropy function defines the interface energy $\sigma(\theta)$

$$\sigma(\theta) = \sigma_0 h(\theta), \quad (2.3)$$

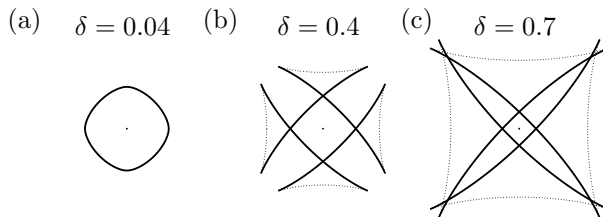


Figure 2.1: Examples of full Wulff plots (i.e. $-\pi \leq \theta \leq \pi$) of 4-fold symmetry with indicated strengths of anisotropy. The dotted segments are the forbidden orientations, solid lines are the allowed ones. The "ears" in b) do not contribute to the isolated particle shape. However, at even stronger anisotropy in c) another intersection occurs among the branches, which introduces new solutions to the equilibrium shape.

where σ_0 is a constant with physical dimensions of interface energy (i.e. J/m^2). In this chapter it is assumed, that the anisotropy function takes the following form

$$f(\theta - \alpha) = 1 + \delta \cos(n(\theta - \alpha)), \quad (2.4)$$

where $0 \leq \delta < 1$ is the strength of anisotropy, n the order of symmetry and α the angle rotating the anisotropy function, representing the 2D crystal orientation. A normalized strength of anisotropy $0 \leq \Omega < (n^2 - 1)$ can be defined as $\Omega = \delta(n^2 - 1)$. In this paper, weak anisotropy will specifically refer to $\Omega < 1$ and strong anisotropy to $\Omega \geq 1$.

The interface stiffness then reads

$$\tilde{\sigma}(\theta) = \sigma_0 \{1 - \Omega \cos[n(\theta - \alpha)]\}. \quad (2.5)$$

The isolated particle with anisotropic interface energy takes on the well-known Wulff shape, which in 2D can be described as a parametric curve $\mathbf{w}(\theta) = [w_x(\theta), w_y(\theta)]^T$ [10, 17, 29]

$$w_x(\theta) = R_W [h(\theta) \cos(\theta) - h'(\theta) \sin(\theta)] \quad (2.6)$$

$$w_y(\theta) = R_W [h(\theta) \sin(\theta) + h'(\theta) \cos(\theta)]. \quad (2.7)$$

See Figure 2.1 for examples of 4-fold symmetry at various strengths of anisotropy δ .

From equation (2.5), it is easily seen that for $\Omega > 1$, there are such θ s, for which the interface stiffness is negative. These normal angles are unstable [5, 17, 29], hence they do not occur on the stable equilibrium Wulff shape (see the dotted

segments in Figure 2.1) and are called missing or forbidden. Closer inspection of the anisotropy function (2.4) and its derivatives reveals that the forbidden angles correspond to interface energies near maxima of the anisotropy function. In fact, the latter is a general observation, independent on the particular anisotropy function (2.4).

For $\Omega > 1$, the equations (2.6)-(2.7) must be understood in a piece-wise fashion for the intervals of allowed θ s. Each of these allowed-angles interval produces a single branch in the Wulff curve. The discontinuity in allowed angles causes that the Wulff shape is no longer a smooth and continuous closed curve (like in Figure 2.1a). Instead, it is a piece-wise continuous and self-intersecting curve (Figure 2.1b-c), where the individual branches enclose a polygon-like closed curve with corners. In the case of Figure 2.1b, the outer parts of the shape (so-called ears) cannot contribute to the (isolated) crystal shape, but for strong enough anisotropy (like in Figure 2.1c) the ears cross again, giving rise to a multitude of other stable equilibrium solutions. That is because every single of the four spikes can be part of the solution but does not need to be. This repeated crossing of the ears and its implications for the equilibrium shapes have not been reported in any work known to the author, hence it will be elaborated on in detail.

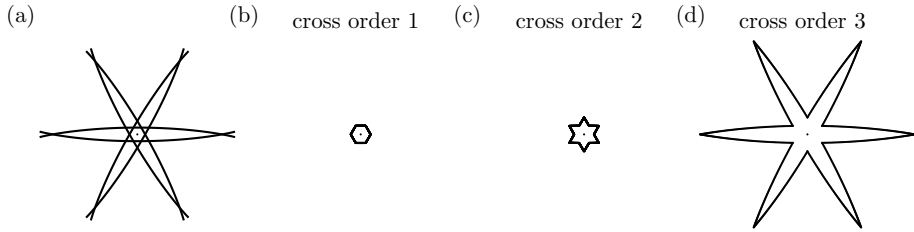


Figure 2.2: Orders of corners, defined by the branches intersections, shown for 6-fold anisotropy and $\delta = 0.7$. In a) there are all the allowed angles, in b)-d) are the stable equilibrium shapes defined by the b) first order, c) second order and d) third order of the corners. Any closed curve is a stable equilibrium shape, which connects these corners along the allowed-angles branches and has the interface normals pointing outwards in every point.

To emphasize the general features of this "crossed-ears" type of solutions, the Figure 2.2a provides another example of very strong, but 6-fold anisotropy, where the ears cross even twice behind the polygon-like isolated Wulff shape. Then, Figures 2.2b-d show the different possible shapes, where the outer corners always correspond to branch intersection of the same type. The type of intersection can be characterized by the radial distance from the center, based on which they can

be ordered. Practically, the corner of the first order is a corner on the polygon-like shape, where two branches forming adjacent sides of the polygon-like shape cross (Figure 2.2b). A corner of the second order is farther from the center and is the intersection of two branches forming two polygon sides separated by a single side (Figure 2.2c). A corner of the third order (Figure 2.2d) is the intersection of two branches separated by two sides etc.

For convenience, the shapes in Figures 2.2b-d will be called isolated Wulff shapes of first, second and third order, respectively.

Below, a summary of some key points is given:

- for $n \geq 2$ and $\delta \geq 1/(n^2 - 1)$ the Wulff shape comprises of n mutually crossing branches and the isolated shape (of first order) exhibits corners,
- for $n \geq 4$ multiple branches intersections occur for sufficiently large δ ,
- the branches intersections (corners) can be characterized by their radial distance from the center,
- the upper limit on the number of intersections of a single branch with others depends on the total number of branches, i.e. on the order of symmetry n ,
- as long as the orientation of the curve is respected (i.e. interface normal of all segments on the shape points outwards), any closed curve connecting the above mentioned corners along the branches is a stable equilibrium shape,
- the shape of higher order contains all the lower-order shapes and has larger area than any of them. The first-order shape thus has the smallest area and, consequently the least total interface energy.

n	order of corner		
	1	2	3
4	0.06667 (1.00000)	0.60000 (9.00000)	x
6	0.02857 (1.00000)	0.16422 (5.74773)	0.62136 (21.74773)

Table 2.1: The approximate minimal strengths of anisotropy at which the corners of indicated order appear on the Wulff shapes in 4-fold and 6-fold anisotropy. The first number is the strength of anisotropy δ and in parenthesis is the corresponding normalized strength of anisotropy $\Omega = \delta(n^2 - 1)$.

In Table 2.1, there are provided the minimal strengths of anisotropy at which the corners of indicated order appear on the Wulff shape in 4-fold and 6-fold anisotropy. Of these, only the first-order corners have an analytic expression, the higher-order corners were obtained numerically and thus are only approximate.

2.2 Particle with anisotropic interface energy on a plane (Winterbottom construction)

The problem of equilibrium shape of a particle with anisotropic interface energy on a planar substrate was treated in various works. It can either be derived from variational principles by total interface energy minimization [36, 72] or by the Cahn-Hoffman vector formalism [11].

The shape is strongly determined by the force balance of the three meeting interfaces: substrate-parent phase (σ_1), particle-parent phase (σ_2) and particle-substrate (σ_3). There are two such contact points in 2D (in 3D it is a triple line) and both must be in force balance in order to sustain a stable equilibrium shape.

Winterbottom construction identifies which segments on the full Wulff shape are (or can be) part of the equilibrium shape of a particle with anisotropic interface energy on a plane.

For tractability of the general solution (of the particle shape), it is essential to assume co-planarity of the particle-substrate and substrate-parent phase interfaces [5, 11, 72].

In 2D, the stability of the shape derives from the stability of the two contact points. In this geometry, all interface energies are known and the orientations of two of the interfaces are known (the former substrate plane). The orientation of the last interface (the particle) in the left and right contact points are expressed by normal angles θ_c^L, θ_c^R , respectively. These are found using the Young's equation with inclination dependence, solved in every contact point

$$\sigma_1 - \sigma_3 = \sigma_2(\theta_2) \sin(\theta_2) + \sigma_2'(\theta_2) \cos(\theta_2), \quad (2.8)$$

which can be written in a non-dimensional form

$$\Gamma = h(\theta_2) \sin(\theta_2) + h'(\theta_2) \cos(\theta_2), \quad (2.9)$$

where $\Gamma = [\sigma_1 - \sigma_3]/\sigma_2^0$ will be denoted *wetting parameter* in this paper. It can be both positive or negative.

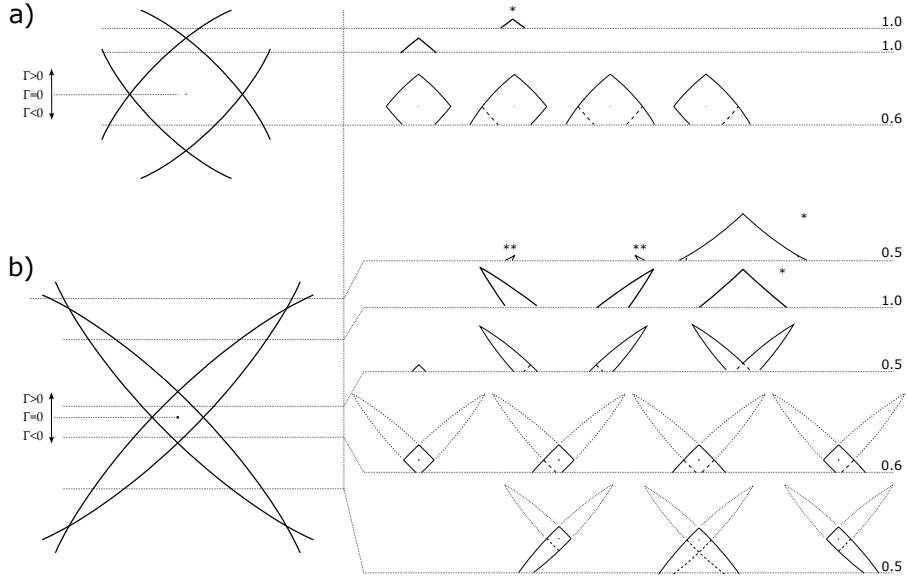


Figure 2.3: Complete list of non-trivial equilibrium shapes of a particle with anisotropic interface energy on a plane (right part of the sketches) as derived from full Wulff shapes (left part of the sketches) using generalized Winterbottom construction. In a) for strength of anisotropy $\delta = 0.3$, in b) with $\delta = 0.7$. The horizontal dotted lines indicate different truncating lines for the Wulff shape and at the same time the substrate for the equilibrium shapes. The scale of the equilibrium shapes relative to the full Wulff shapes on the left is provided on the right on every respective line. Inverted shape solutions of first order are indicated by asterisk *, of the second order by **. The dashed lines within some of the the equilibrium shapes show the segments on the Wulff shape which were enclosed by the equilibrium shape. The dotted lines above the equilibrium shapes in b) indicate the crossed-ears solutions, which either may be present both, separately or both be absent. The new solutions can be seen in b).

The solutions are from the ranges $3\pi/2 > \theta_c^L > \pi/2$ and $\pi/2 > \theta_c^R \geq -\pi/2$ and must be allowed angles. When (2.9) is compared to (2.7), it is obvious that the solutions θ_c^L, θ_c^R are found as normal angles in points with y coordinate equal to Γ on an unit-radius Wulff shape. Thus, the resulting particle shape is a segment of the isolated shape, where the position of the sectioning plane Γ is determined by the force balance. That is the Winterbottom construction. Originally, it served to find the shape of the least interface energy, but Bao [5] generalized it for any stable equilibrium shape. For illustration of the generalized

Winterbottom construction depending on the position of the truncating line see Figure 2.3.

When the anisotropy is strong, multiple stable equilibrium shapes may exist even when the isolated shape has only a single equilibrium stable shape. All these solutions are illustrated in Figure 2.3a for 4-fold anisotropy, moderately strong [5]. In Figure 2.3b all possible solutions are presented for very strong 4-fold anisotropy, which involves the new solutions derived from the second-order corners.

If multiple solutions existed in the isolated particle in the above-truncating-line part, this multiplicity is present in the possible solutions on the plane too (Figure 2.3b). Compared to the isolated case, additional solutions are present, when the truncating line passes below the center of the isolated shape, with the shape being defined also by the "ears" extending behind the corners (in both Figure 2.3a and 2.3b).

An exceptional class of the solutions is the *inverted shape solution* (indicated by asterisk in Figure 2.3), which is found *below* the sectioning plane, as described by Bao [5] on a shape like in Figure 2.3a. However, due to the inverted shape symmetry, it is not clear, what operation(s) of symmetry the "inversion" refers to according to Bao and how to construct the solution in a general case. More detailed characterization of this solution type was given in the following section 2.3. It should be noted that in systems with corners of higher order, multiple orders of the inversion shape are possible (also indicated in Figure 2.3 by asterisk * and described in more detail in 2.3).

2.3 Inverted solution in Winterbottom construction

The inverted shape in a Winterbottom construction with single plane was described by [5] in a highly symmetric case. The same idea was used much sooner in the Winterbottom construction in a corner (meaning Wulff shape resting on two lines at once, intersecting in a corner) by Zia et al. [77] ("Summertop construction"). Below, the inverted shape construction is described, taking into account the higher-order intersection solutions and arbitrary rotations.

Let the Wulff shape exhibit strong anisotropy, i.e. be there at least corners of first order. Further, let the wetting parameter Γ be such, that the truncating line passes at least above the isolated shape of the first order, i.e. the first-order shape is submerged below the substrate plane.

Then it may happen, that the truncating line intersects two branches, which crossed below it (see Figure 2.4a1). Such situation allows a solution, where the

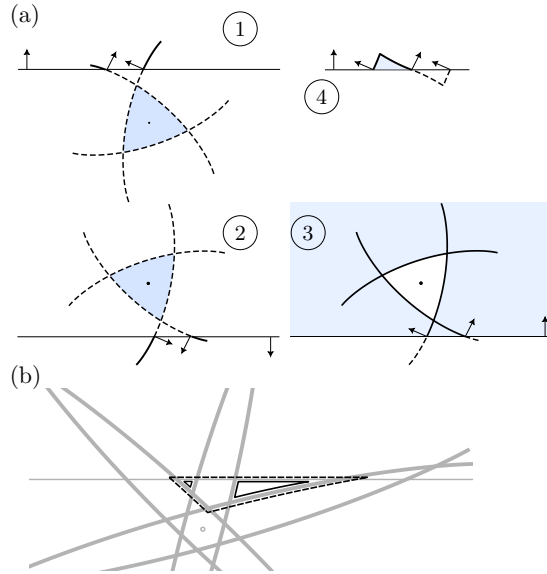


Figure 2.4: Illustration of the inverted Winterbottom construction. In (a) explained in 4 steps and in (b) illustration of inverted solutions of higher orders. In (a) the plane normal points from the substrate to the parent phase, the solid lines of the Wulff plot are thus above the substrate plane and the dashed ones are below. Interface normals in the contact points are indicated as well. In 1 is the initial state, in 2 after center inversion, in 3 after the curve orientation flip and in 4 is the resulting shape next to the original part of the Wulff plot. In (b) the dashed black line indicates inverted shape of the first order, the solid line that of second order.

equilibrium shape is the part *below* the substrate plane, but *above* the corner where the two branches intersect. Two steps must be followed to obtain the inverted equilibrium shape:

1. point inversion of the whole system (Wulff plot + truncating line) about the center of the Wulff shape (see Figure 2.4a2)
2. flip orientation of both the inverted Wulff plot and inverted truncating line, i.e. flip the inverted inward and outwards directions (see Figure 2.4a3)

The first operation places the truncating line below the said corner, where the two branches intersect. At the same time, the whole shape is inverted. The second operation turns the outside of the Wulff plot to be inside - i.e. instead

of having a crystal in the shape of inverted Wulff plot in some medium, we have a medium in the shape of Wulff plot surrounded by the crystal.

Then, the resulting inverted shape as in Figure 2.4a4 is obtained as an enclosed intersection of the anisotropic Wulff plot and a half-space above the line. All the interface normal orientations on the surface of the inverted shape are the same as on the non-inverted part of the Wulff plot. Importantly, this includes the normal angles in the contact points, as can be seen in Figure 2.4a4.

The order of the intersection in which the two Wulff branches intersect, determines the order of the inverted shape. Figure 2.4b shows an example of strong 6-fold anisotropy with such truncation, that it allows two orders of inverted shapes at once.

2.4 Contact point stability

The contact points mentioned above are essentially triple junctions. The Young's equation with inclination dependence (2.8) represents equilibrium of the tractions due to the interfaces on the junction in the x direction. It concerns a special case, where the position of two of the three interfaces are fixed to lay on the x axis and the third has inclination-dependent interface energy. However, the *stability* of the triple junction configuration is not guaranteed by Young's equation alone [37]. In the present case, the configuration means a solution θ_2 to (2.8). Technically, the solutions to (2.8) are stationary points of the triple junction energy as function of virtual translations, but not necessarily its minimum (i.e. the stable configuration). Stability of the found solutions should be thus tested using additional conditions derived from second-order derivatives of the triple junction energy with respect to the virtual translations [37]:

$$0 < \tilde{\sigma}_1 s_1 + \tilde{\sigma}_2 s_2 + \tilde{\sigma}_3 s_3 \quad (2.10)$$

$$0 < \tilde{\sigma}_1 \tilde{\sigma}_2 S_{12} + \tilde{\sigma}_2 \tilde{\sigma}_3 S_{23} + \tilde{\sigma}_1 \tilde{\sigma}_3 S_{13}, \quad (2.11)$$

where $\tilde{\sigma}_i$ are the respective interface stiffnesses, $s_i = \cos^2(\theta_i)/d_i$, $S_{ij} = \sin^2(\theta_i - \theta_j)/d_i d_j$. In the present geometry, interfaces 1 and 3 are fixed with $\theta_1 = \pm\pi/2$ and $\theta_3 = \mp\pi/2$, hence it follows that $s_1 = s_3 = 0$ and also that $S_{13} = 0$. Note also that $s_2 > 0$ and $S_{12} = S_{23} = S > 0$. By the geometry alone, the conditions are thus simplified to

$$0 < \tilde{\sigma}_2 \quad (2.12)$$

$$0 < \tilde{\sigma}_1 \tilde{\sigma}_2 + \tilde{\sigma}_2 \tilde{\sigma}_3, \quad (2.13)$$

where only the interface stiffnesses matter. Using the first equation, the second one may further be simplified

$$0 < \tilde{\sigma}_1 + \tilde{\sigma}_3. \quad (2.14)$$

The condition (2.12) implies, that the particle-parent phase interface must be oriented under allowed angle in the contact point. That is fulfilled automatically by the truncated Wulff shape solution, because it contains only the allowed angles.

Note that the interfaces 1 and 3 have fixed orientations and are assumed to be planar. The condition (2.14) is surely fulfilled when both interfaces 1 and 3 have positive interface stiffness in their orientations. That holds automatically in weak or no anisotropies. When either or both of the two interfaces exhibit strong anisotropy, it means that there are normal angles where the interface stiffness is negative, hence the condition (2.14) may be violated and must be verified in the given configuration.

2.5 Selected geometric properties of Wulff shape

With $h(\theta) = 1 + \delta \cos(n\theta)$, the minimal distance R_{min} between the Wulff shape center and the contour can be related to R_W as

$$R_{min} = R_W(1 - \delta), \quad (2.15)$$

which holds for arbitrarily strong anisotropy because the minimal-radius point normal is always inclined under a non-missing angle. This formula was used to find the radius R_W of the phase field contour. Then, the phase field contour was scaled to unit radius and compared to the analytic Wulff shape (by means of Hausdorff distance, see the next subsection).

The radius of curvature $\varrho(\theta)$ of Wulff shape is locally

$$\varrho(\theta) = R_W[h''(\theta) + h(\theta)], \quad (2.16)$$

which may technically get negative for some θ . Because that does not have any geometric interpretation, the Wulff shape does not contain such oriented segments and the angles θ_m fulfilling $\varrho(\theta_m) \leq 0$ are called missing or forbidden.

For a given radius R_W , the area of a Wulff shape A_W differs from the area of a circle $A = \pi R_W^2$ by the anisotropy-dependent factor $C_W(\Omega, n) = A_W/A$. For weak anisotropy $\Omega < 1$ there is an analytic expression

$$C_W = 1 - \frac{\Omega^2}{n^2 - 1}, \quad (2.17)$$

but there is none for strong anisotropy $\Omega > 1$. The factor $C_W(\Omega, n)$ was obtained numerically for $n = 4$ in the range $0 \leq \Omega \leq 7.5$ (the Wulff shape was plotted, its area numerically computed and divided by πR^2). There, the Ω -dependence was fitted very well by a polynomial of 4-th order $C_W(\Omega, 4) = \sum_{i=0}^4 a_i \Omega^{N-i}$ with $a_0 = -0.00032, a_1 = 0.00639, a_2 = -0.04219, a_3 = 0.00034, a_4 = 1.00000$.

2.6 Shrinkage rate of a Wulff shape

The normal velocity of anisotropic curvature-driven interface in 2D is [1]

$$v_n(\theta, t) = -\frac{\mu}{\varrho(\theta, t)} \sigma_0 [h''(\theta) + h(\theta)] \quad (2.18)$$

where μ is the interface mobility and $\sigma_0 [h''(\theta) + h(\theta)]$ is interface stiffness. When it is the Wulff shape shrinking, the radius of curvature $\varrho(\theta, t)$ can be expressed as in equation (2.16) and the inclination-dependent part of the interface stiffness is cancelled out. The normal velocity is then constant along the perimeter

$$v_n(t) = -\frac{\mu \sigma_0}{R_W(t)}. \quad (2.19)$$

The sign is such that the interface moves towards the center of curvature.

Because the area of a Wulff shape is $A_W = \pi R_W^2 C_W(\Omega, n)$, the shrinkage rate of a Wulff shape is

$$\begin{aligned} \frac{dA_W}{dt} &= \frac{d}{dt} [\pi R_W^2(t) C_W(\Omega, n)] \\ &= 2\pi C_W(\Omega, n) R_W(t) \frac{dR_W}{dt}. \end{aligned} \quad (2.20)$$

Because the normal velocity is constant along the perimeter, the point R_{min} from equation (2.15) moves also by $v_n(t)$. Importantly, the normal of interface in R_{min} is aligned with the radial direction of the polar coordinates, hence we can write $v_n = dR_{min}/dt$. From equation (2.15) then must be

$$\frac{dR_W}{dt} = \frac{1}{1-\delta} \frac{dR_{min}}{dt} = \frac{1}{1-\delta} v_n(t), \quad (2.21)$$

which together with 2.19 implies in 2.20

$$\frac{dA_W}{dt} = 2\pi \mu \sigma_0 \frac{C_W(\Omega, n)}{1-\delta} \quad (2.22)$$

Taylor and Cahn [64] proved that the shrinkage rate for the equilibrium shape must be a constant, which is met by the final expression.

2.7 Summary and the author's contribution

This chapter contained fundamental information about the equilibrium stable shapes of particles with anisotropic interface energy, assuming absence of other driving forces which might affect their shape. Isolated particles as well as those on a plane were assessed in 2D. New stable equilibrium shapes were described in the case of very strong anisotropy, where the Wulff plot may self-intersect multiple times, thus giving rise to the solutions containing parts formed by crossed "ears". The notion of "order of the intersection" was introduced to generalize the description of the emerging solution type.

Regarding the particle on a plane, the inverted solution type was described in detail allowing its construction for arbitrary nucleus orientation and wetting. Inverted solutions of higher orders were described as well.

The author is not aware of another work applying the stability conditions for the triple junction configuration to the nucleus contact points. Later, it is shown that for particles with strongly anisotropic interface energy, the stability condition is a very strong influence on the orientation selection in repeated nucleation.

Some basic geometric properties of the Wulff shapes were reviewed, which were later utilized in the phase-field model benchmarking. Specifically, the steady-state shrinkage rate of a Wulff shape is a useful formula derived by the author.

Chapter 3

Phase field method

3.1 General introduction

Phase field method is a diffuse-interface approach to solving moving-boundary problems. In materials science it is usually used as meso-scale method. It has numerous applications such as e.g. (multi-component) solidification, grain growth, Ostwald ripening, solid-solid phase transitions (martensitic, precipitation, spinodal...), two-phase flow, nucleation, wetting and much more.

The method is based on the principle of total system energy minimization. The free energy density of the system is a function of all the possibly mutually coupled physical fields, including the fields representing the phases. These are typically called phase fields, order parameters or continuum fields. The other (bulk) physical fields can be e.g. concentration, temperature, electric charge or others. The total energy of the system is then spatial integral of the free energy density over the simulation domain - the free energy functional.

The governing equation(s) for the phase fields are derived using principles of variational calculus, which ensure the fields evolution so that the free energy functional is minimized along the direction of steepest descent, i.e. the most likely way towards the equilibrium. Additionally, the curvature driving force and the possible coupling with the bulk fields are represented. That is the reason for high versatility of the method and its capability to simulate coupled multiphysics.

Due to the thermodynamic nature of the method, the interface energy is naturally included as an input parameter. Multigrain or multiphase systems

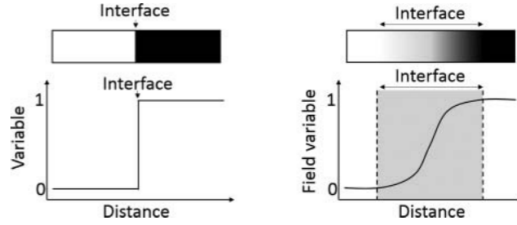


Figure 3.1: Illustration of the diffuse interface in phase field method (on the right) and the comparison to an actual, sharp interface (on the left). [6]

with interfaces of various properties can be simulated with multi phase field models. Some of these allow to include also inclination dependence of interface energy. In fact, it was phase field simulation which revealed the paramount importance of interface energy anisotropy in pattern formation during dendritic solidification [28].

A phase (or phases) in an inhomogeneous system is described by a continuous function (called phase field, order parameter or continuum field), having different constant values in the bulk of the phases (typically 1 and 0 or 1 and -1). At the interface between phases, the phase field varies smoothly between the values and the interface region is thus characterized by a certain width, as sketched in Figure 3.1. This interface width is an important input parameter in phase field models. In quantitative phase field models, the model behavior is in principle not affected by the particular value of interface width chosen, which allows to make quantitative simulations at mesoscale (whereas the real interface width is in the order of units of nm).

The governing equations for the phase fields are typically either conservative (Cahn-Hilliard type of equation, conserving volume) or non-conservative (Allen-Cahn type of equation). The latter is more relevant for this work. In the following, no coupling to other physical fields is assumed.

3.2 Allen-Cahn equation for two-phase system

It was shown that the Alen-Cahn equation is a diffuse-interface approximation of a curvature-driven system. It represents evolution of a non-conserved field

$\eta(\mathbf{r})$ in a domain $\Omega \in \mathbb{R}^3$ with boundary $\partial\Omega$ and can be written as

$$\frac{\partial \eta}{\partial t} = -L \frac{\delta F}{\delta \eta} \quad \text{in } \Omega \quad (3.1)$$

$$\nabla \eta \cdot \mathbf{n} = 0 \quad \text{at } \partial\Omega, \quad (3.2)$$

where L is a positive constant and the function $\frac{\delta F}{\delta \eta}$ stands for functional derivative of the free energy functional F . The functional is an integral with free energy density $f(\eta, \nabla \eta) = f_{hom}(\eta) + f_{int}(\nabla \eta)$ comprising of the homogeneous and interfacial free energy densities

$$F = \int_V f_{hom}(\eta) + f_{int}(\nabla \eta) dV \quad (3.3)$$

$$= \int_V m\eta^2(1-\eta)^2 + \frac{\kappa}{2} |\nabla \eta|^2 dV \quad (3.4)$$

with positive constants m, κ being the double barrier height and gradient energy coefficient, respectively. The homogeneous free energy density f_{hom} in the form of the double-well function assures two stable states for the field variable in values 0 and 1. The gradient energy contribution is lessened by the diffuse interface widening, whereas conversely the homogeneous free contribution is lessened by its narrowing. When minimizing the full integral, a balance between the two effects is reached in equilibrium.

As described in more detail in the Appendix A, the functional derivative is computed as

$$\frac{\delta F}{\delta \eta} = \left[\frac{\partial f}{\partial \eta_p} - \nabla \cdot \frac{\partial f}{\partial (\nabla \eta_p)} \right] \quad (3.5)$$

where $\nabla \cdot \partial f / \partial (\nabla \eta_p)$ is divergence of vector field $\partial f / \partial (\nabla \eta_p)$ defined by relation

$$\frac{\partial f}{\partial (\nabla \eta_p)} = \frac{\partial f}{\partial (\partial_x \eta_p)} \mathbf{n}_x + \frac{\partial f}{\partial (\partial_y \eta_p)} \mathbf{n}_y + \frac{\partial f}{\partial (\partial_z \eta_p)} \mathbf{n}_z \quad (3.6)$$

with $\partial_x, \partial_y, \partial_z$ being operators for unidirectional derivatives in the corresponding directions and $\mathbf{n}_x, \mathbf{n}_y, \mathbf{n}_z$ coordinate base vectors.

When applied applied to the above functional, it will result in the Allen-Cahn equation

$$\frac{\partial \eta}{\partial t} = -L[f'_{hom}(\eta) - \kappa \nabla^2 \eta] \quad (3.7)$$

$$= -L[2m\eta(1-\eta)(1-2\eta) - \kappa \nabla^2 \eta]. \quad (3.8)$$

In equilibrium, the interface is static, $\partial\eta/\partial t = 0$, which means that the forces narrowing and widening the interface are in balance, i.e. $f'_{hom}(\eta) = \kappa \nabla^2 \eta$, or equivalently (in 1D)

$$2\eta(1-\eta)(1-2\eta) = \frac{\kappa}{m} \frac{\partial^2 \eta}{\partial x^2}. \quad (3.9)$$

Solution to this equation provides the equilibrium profile of the phase field (centered in $x = 0$), which in this case is the following sigmoid function

$$\eta(x) = \frac{1}{2} \tanh \left(\sqrt{\frac{m}{2\kappa}} x \right). \quad (3.10)$$

The equilibrium also implies, that the homogeneous and interfacial energies are equal except for a constant, i.e. $f_{hom} = f_{int} + C$, which can be shown to be zero $C = 0$ (see e.g. [47]).

Interface width l_{int} (unit m) can be defined using the reciprocal maximal slope in the interface (present in $\eta = 0.5$)

$$l_{int} = \frac{1}{d\eta/dx|_{max}} = \frac{1}{\sqrt{2f_{hom}/\kappa}} \Big|_{\eta=0.5} = 2\sqrt{2} \sqrt{\frac{\kappa}{m}}, \quad (3.11)$$

where the relation $d\eta/dx = \sqrt{2f_{hom}/\kappa}$ is derived from $f_{hom} = f_{int}$.

The excess free energy σ (the *interface energy*, unit J/m²) at a flat interface can be computed as an 1D integral of the free energy density along perpendicular line through the interface

$$\sigma = \int_{-\infty}^{+\infty} f_{hom} + \frac{\kappa}{2} |\nabla \eta|^2 dx. \quad (3.12)$$

From $f_{hom} = f_{int}$ it can be written $dx = \sqrt{\kappa/2f_{hom}} d\eta$, which allows to solve (3.12) by substitution as follows

$$\sigma = \int_{-\infty}^{+\infty} 2f_{hom} dx \quad (3.13)$$

$$= \int_0^1 \sqrt{2f_{hom}\kappa} d\eta \quad (3.14)$$

$$= \frac{\sqrt{2}}{6} \sqrt{m\kappa}. \quad (3.15)$$

In practice, the model is parameterized by the interface width l_{int} and interface energy σ , from which the model parameters m, κ must be computed. The

necessary formulas are obtained from (3.11) and (3.15) as

$$\kappa = \frac{3}{2}\sigma l_{int} \quad (3.16)$$

$$m = 12\frac{\sigma}{l_{int}} \quad (3.17)$$

The l_{int} is chosen depending on the scale of the problem, disregarding the real physical interface width.

As shown in [47], the following equality between the model parameters and the interface mobility μ holds

$$\mu\sigma = L\kappa, \quad (3.18)$$

which allows to express the phase field kinetic coefficient as

$$L = \frac{2}{3}\frac{\mu}{l_{int}}, \quad (3.19)$$

where the equation (3.16) was used.

3.3 Allen-Cahn equation for two-phase system including anisotropic interface energy

3.3.1 Fundamentals

The most straightforward way to introduce anisotropy in the interface energy in the model is to make either of the model parameters κ, m a function of the inclination angle respecting both the anisotropy function and the defining parameter relations.

Tschukin [68] proposes the terminology of *classical* and *natural* models (corresponding to the notation VIW and VIE, respectively, as used by Fleck [18], standing for *Variable Interface Width* and *Variable Interface Energy*). The classical models [17, 28, 38, 64, 70], introduce anisotropy in the gradient energy coefficient κ , whereas the natural models [18, 35, 47, 66] in both the gradient energy coefficient κ and homogeneous energy density barrier m . The main difference between the classical and natural formulations is that in the first case the diffuse interface width varies proportionally to the local interface energy (see equation (3.11)), whereas in the latter the interface width can be decoupled from the interface energy and the interface width maintained constant (see (3.11) and (3.15)). Below, more details are provided on both model formulations.

Let's assume that the interface energy is inclination-dependent in the following form (in 2D)

$$\sigma(\theta) = \sigma_0 h(\theta), \quad (3.20)$$

with the inclination angle θ of the interface normal $\mathbf{n} = [n_x, n_y]^T$ being defined as $\theta = \text{atan2}(n_y/n_x)$ and σ_0 constant with physical dimensions J/m². The interface normal is defined from phase field as

$$\mathbf{n} = \frac{\nabla \eta}{|\nabla \eta|}. \quad (3.21)$$

First, a classical model with anisotropy only in κ will be developed. The equations (3.15) and (3.20) are combined

$$\sigma(\theta) = \sigma_0 h(\theta) = \frac{\sqrt{2}}{6} \sqrt{m \kappa(\theta)} \quad (3.22)$$

and allow to express the anisotropic $\kappa(\theta)$

$$\kappa(\theta) = \kappa_0 [h(\theta)]^2 \quad \text{and} \quad \sigma_0 = (\sqrt{2}/6) \sqrt{m \kappa_0}, \quad (3.23)$$

which recovers the interface energy anisotropy (3.20).

Recall that $\theta = \theta(\mathbf{n}(\nabla \eta))$, hence the θ dependence in (any) model parameter implies that in the governing equations new terms arise from the divergence part of the functional derivative $\nabla \cdot \partial f / \partial (\nabla \eta_p)$, where the free energy density is taken derivative of with respect to the gradient components.

This anisotropy implementation implies that the interface width l_{int} varies proportionally to the interface energy (see (3.11)) and this in turn introduces nonphysical anisotropy in the kinetic coefficient L (see (3.19)). The latter is should be compensated, the first must be taken into account in practical simulations so that there are no excessively large or narrow interfaces in the domain.

In strongly anisotropic systems, the variable interface width poses a practical problem. However, it can be prevented by including the anisotropy also in the parameter m . When the anisotropy is assigned in the natural model formulation as

$$\kappa(\theta) = \kappa_0 h(\theta) \quad (3.24)$$

$$m(\theta) = m_0 h(\theta), \quad (3.25)$$

the interface width is constant $l_{int} = 2\sqrt{2} \sqrt{\frac{\kappa_0}{m_0}}$ (see (3.11)) and the following relation holds as well

$$\sigma_0 h(\theta) = \frac{\sqrt{2}}{6} \sqrt{m(\theta) \kappa(\theta)}. \quad (3.26)$$

Because both κ, m depend on θ , even more terms derive from the divergence in the functional derivative, as described earlier.

Another notable approach uses Finsler geometry to replace the Euclidean metric in the simulation domain by an anisotropic one [7, 8]. Formally, the anisotropic Allen-Cahn equation is then not much more complicated than the isotropic one, even though new terms arise as well. The interface width is constant, though.

3.3.2 Challenges and limitations

The main challenges come from the type of anisotropy function and from the strength of anisotropy. So far, it was implicitly assumed that the anisotropy function is continuous and twice-differentiable homogeneous function of order 1. In chapter 2 the problem arising from forbidden angles was worked in some detail, but here it will be put into a context specific for phase field method.

Generally, two types of singularities may occur on the Wulff shapes of the first order (for the terminology see section 2.1): corners and facets. These two depend on the following properties of the particular anisotropy function

1. (non-)convexity of the Frank's plot, i.e. $1/h(\theta)$ and
2. (non-)differentiability with respect to the polar angle (typically presence of a cusp).

The first produces corners (when non-convex) and the second facets (when non-differentiable).

The easiest solution to the non-differentiability is to replace the anisotropy function by such one, in which the cusps are a smooth tips. These functions are typically formulated in such a way, that the sharpness of the tip is scalable, but formally the function is always smooth. This allows to approximate the former anisotropy close enough while assuring validity of the formulas relying on the differentiability. This was employed for example in [16, 34, 45].

The non-convexity of the Frank's plot does not have so easy solution. It causes the governing equations to be ill-posed, which means that the solution to is either not existing, unique or does not depend continuously on the initial/boundary conditions. In this case the uniqueness is the problem, because it is not clear, whether a certain segment on the surface should align with the "ear" orientation or some on the Wulff plot of the first order. In practice, it causes corrugations of the phase field contour near the corners, see e.g. [68]. The ill-posedness can be removed by regularization (and thus the match in corners improved), the following approaches are known to the author

1. regularization of the anisotropy function [17, 29, 64],
2. inclusion of higher order terms in expansion of interface energy in the free energy functional [66, 68, 70],
3. models incorporating the Finsler geometry do not need regularization [7, 8],
4. one study reports numerical regularization which occurred after using spectral solver [67].

All of the above approaches were successful in delivering cornered or faceted Wulff shapes of the first order and anisotropic crystals grown in either temperature or concentration field. These were the main applications of these models so far. Very likely, each of these will have its own limitations in the future applications, but currently the author is unaware of any systematic comparison of these in the literature and himself only implemented the first approach.

3.4 Allen-Cahn equations for multi-phase systems

3.4.1 Historical context

Multi-phase field models emerged from the need to simulate systems with more than two phases. At first, these models were developed to simulate ideal grain growth in systems with isotropic grain boundary energy. That is a natural choice, because the grain coarsening is curvature driven and the Allen-Cahn equation approximates the mean curvature flow. The main characteristic of the multi-phase field models is that every grain or phase is characterized by its own field variable, which implies that these systems may contain many governing equations, even tens of thousands in large scale grain growth simulations [75].

Even though there were published many model formulations, all those known to the author can be attributed to one of two main branches of development: one initiated by the work of Long-Qing Chen in 1994 [13] and the other by Steinbach in 1996 [63]. The most fundamental difference is that in Steinbach's branch, the field variables are interpreted as local phase fractions, whereas in the Chen's there is no direct physical interpretation of the field variables. For this reason, it is not accurate to call the latter multi-phase-field models (MPF), but the difference is rather technical and not obvious to broader scientific community. When there is the need to differentiate the two groups of models, the multi-continuum-field (CF) or multi-order-parameter model are the options to call the models in Chen's legacy.

Both multi-phase-field and multi-continuum-field models were extensively developed beyond the ideal grain growth, and nowadays the two model families are comparable in terms of maturity and applicability. The models offer anisotropy in interface energy and kinetic coefficient (pair-wise isotropic as well as the inclination dependence), coupling to multi-component systems using the Onsager's theory, possibly employing the thermodynamic databases to express the concentration dependence of the free energy density.

Real interfaces (including the grain boundaries) exhibit anisotropic (inclination-dependent) interface energies [9, 54], hence a significant effort was made to introduce this feature in some multi-phase field [19, 60, 67, 69] and continuum-field models [26, 47].

Toth provided structured and rational fundamental criteria to assess thermodynamic consistency of a multi-phase field model [67], most of which are applicable to the multi-continuum-field models as well. They include e.g. the requirement that the

- results should not depend on the fields numbering
- model should be scalable in the number of simulated fields
- model should allow assignment of binary interface properties (interface energy and kinetic coefficient) independently to every possible pair of fields
- total system energy decreases monotonically (second law of thermodynamics)
- ghost phases do not appear

and some others. Both model families have models which fulfill most of the criteria or even all of them.

3.4.2 Challenges and limitations

One of pragmatic requirements on these models not listed in [67] is that they must correctly reproduce force balance in triple and higher-order junctions. Despite high maturity of the models and great relevance of triple junctions for the grain coarsening, only very recently there was a structured attempt to quantify the performance of different models in how they reproduced the triple junction behavior in well defined scenarios [15].

This study emphasized, that probably the largest challenge for both CF and MPF models are the ghost phases. These manifest as a finite amount of a third phase within a binary interface between two other fields. Ghost phases are unphysical and their amount was correlated with the (poorer) quality of match of dihedral angles in the triple junctions benchmark problems [15].

The ghost phases mitigation strategies include in the first place reformulation of either homogeneous or gradient energy contributions to avoid problematic driving force terms emerging from the functional derivative, then additions of ternary terms, or even neglecting the problematic driving force terms. In continuum-field models, the ghost phases were eliminated by specific way the model parameters were made anisotropic, but at the cost of having variable interface width.

The community has just acquired for itself the tools to quantify the models performance in triple junctions of interfaces with isotropic interface energies [15]. Certainly, a challenge ahead are the triple junctions of interfaces with inclination-dependent interface energy. First, a benchmark problem must be developed and then used to compare the models. However, before such study, no simulation of grain growth with inclination dependent interfaces including the triple junctions is reliable. In the multi-phase field models including the inclination dependent interface energy there are many more terms in the governing equations, which makes the ghost phases prevention by model reformulation significantly more complicated than in the pair-wise isotropic case.

3.5 Benchmarking of phase field models

The community produces many applications of the phase field method, often involving complicated multi-physics, to deliver solutions to complex engineering and scientific problems. However, the know-how related to the individual modeling approaches seems to be rather fragmented into the individual groups and works comparing different models are rather exceptional. Different models for the same purpose may have different formulations, but the differences in their behavior are not obvious, especially because there is no unified, generally accepted validation procedure for quantitative assessment of performance in terms of represented physics.

Another source of confusion about the limits of phase field method in general is that some works claim to bring "quantitative" or "thermodynamically consistent" phase field models of complicated multiphysics problem (e.g. electrodeposition of lithium [12]) after doing some lower-dimensional check on a not coupled problem. This way of presentation makes the impression that everything is

possible, when in fact the more equations are coupled, the easier it is to hit reasonable limits of applicability for the model.

Where exactly lay the limits of the current models is also partially obscured by the fact, that it is not a norm to publish the codes used to produce published results, which significantly affects their reproducibility.

Systematic and reproducible parametric studies in well-defined problems are needed for quantitative assessment of phase field models reliability. The lack of benchmarking is present in terms of physics and also of models comparison. It is critical especially in models coupling many physical driving forces. In order to confidently and honestly interpret results of quantitative phase field simulations, both physical models and numerical implementations must be validated and verified [25]. Recent initiative PFHub addresses the need for benchmarking of the multitude of software and numeric approaches for solving the phase field governing equations.

Usually, the validation of models with inclination-dependent interface energy was carried out by visual comparison of the phase field contours to corresponding Wulff shapes for single or several values of strength of anisotropy [17–19, 35, 68]. Such approach does not reveal the limits of reliability of these models, though.

The cited study comparing the MPF and MCF models in the triple junctions benchmarks [15] was initiated by the author and he believes that using the presented benchmarks for assessment of the new models or implementations performance adds more reliability whenever the tested multi-phase field models will be used.

Chapter 4

Extended multi-phase field model

The multi-phase field model by Moelans [47] is an established [46] quantitative phase field model of grain growth with anisotropic grain boundary properties. Using asymptotic analysis, Moelans derived that in the original model [47], the local interface energy and width are related to three model parameters. Because these are two equations of three variables, the system is undetermined and one of the model parameters is free. This degree of freedom introduces the possibility of many different parameters assignment strategies, all of which represent the same physical input. The effect of different but equivalent parameters choices can thus be investigated in this model. Moelans proposed such parameters assignment strategy [47], which assured constant interface width irrespective of the strength of anisotropy in interface energy (a kind of *natural* formulation). Two of the three model parameters (γ and κ) were made anisotropic in order to achieve such behavior. However, this approach (here denoted IWc - *Interface Width constant*) does not reproduce well the angles between interfaces in triple junctions for stronger anisotropies. This was already first noted by Moelans in [48]. An alternative parameters assignment strategy with only parameter γ anisotropic was used in [46, 59], but no systematic comparison was made. In this approach, the interface width is not constant in anisotropic systems, but it is not simply classifiable as *classical* anisotropy formulation, because the gradient energy coefficient is constant. It will be denoted IWvG (*Interface Width variable and Gamma anisotropic*). The third compared parameters assignment strategy is the *classical* formulation, varying only gradient energy coefficient κ to achieve the desired interface energy anisotropy (denoted IWvK - *Interface*

Width variable and Kappa anisotropic). Additionally, the inclination dependence of interface energy in IWvG and IWvK have not yet been addressed in the framework of Moelans' model.

4.1 Introduction

The system consists of n non-conserved continuous-field variables (further denoted phase fields) $\eta_1(\mathbf{r}, t), \eta_2(\mathbf{r}, t), \dots, \eta_n(\mathbf{r}, t)$, which are functions of space and time. The total free energy of the system is expressed as functional of the phase fields and their gradients $\nabla\eta_1(\mathbf{r}, t), \nabla\eta_2(\mathbf{r}, t), \dots, \nabla\eta_n(\mathbf{r}, t)$

$$F = \int_V \left\{ m f_0(\vec{\eta}) + \frac{\kappa}{2} \sum_{i=1}^n (\nabla\eta_i)^2 \right\} dV, \quad (4.1)$$

where the homogeneous free energy density $f_0(\vec{\eta}) = f_0(\eta_1, \eta_2, \dots, \eta_n)$ is expressed as

$$f_0(\vec{\eta}) = \sum_{i=1}^n \left(\frac{\eta_i^4}{4} - \frac{\eta_i^2}{2} \right) + \gamma \sum_{i=1}^n \sum_{i>j} \eta_i^2 \eta_j^2 + \frac{1}{4}. \quad (4.2)$$

The parameters m, κ, γ are model parameters, which together define interface energy and interface width (see the following section for more details).

The governing equations for each phase field η_p are obtained based on the functional derivative of the free energy functional with respect to η_p , assuming that the phase-fields are non-conserved, i.e.

$$\frac{\partial\eta_p}{\partial t} = -L \frac{\delta F}{\delta\eta_p} = -L \left[\frac{\partial f}{\partial\eta_p} - \nabla \cdot \frac{\partial f}{\partial(\nabla\eta_p)} \right], \quad (4.3)$$

where L is the kinetic coefficient (also dependent on the model parameters), f is the full integrand in (4.1) and $\nabla \cdot \partial f / \partial(\nabla\eta_p)$ is divergence of vector field $\partial f / \partial(\nabla\eta_p)$ defined by relation

$$\frac{\partial f}{\partial(\nabla\eta_p)} = \frac{\partial f}{\partial(\partial_x\eta_p)} \mathbf{n}_x + \frac{\partial f}{\partial(\partial_y\eta_p)} \mathbf{n}_y + \frac{\partial f}{\partial(\partial_z\eta_p)} \mathbf{n}_z \quad (4.4)$$

with $\partial_x, \partial_y, \partial_z$ being operators for unidirectional derivatives in the corresponding directions and $\mathbf{n}_x, \mathbf{n}_y, \mathbf{n}_z$ coordinate base vectors.

4.2 Isotropic model

In a system with uniform grain boundary properties, the interface energy is equal for all interfaces and hence the phase-field model parameters m, κ, γ (and interface width l) are constant in the system.

Then, using the expression (4.3), the governing equation for each phase field η_p takes the following form

$$\frac{\partial \eta_p}{\partial t} = -L \left[m \left(\eta_p^3 - \eta_p + 2\gamma \eta_p \sum_{j \neq p} \eta_j^2 \right) - \kappa \nabla^2 \eta_p \right] \quad (4.5)$$

The interface energy σ of the system is related to the model parameters via

$$\sigma = g(\gamma) \sqrt{m\kappa}, \quad (4.6)$$

where $g(\gamma)$ is a non-analytic function of parameter γ . The interface width l is expressed as

$$l = \sqrt{\frac{\kappa}{m f_{0c}(\gamma)}}, \quad (4.7)$$

where $f_{0c}(\gamma)$ is the value of $f_0(\eta_{i,cross}, \eta_{j,cross})$ in the points where the two phase fields η_i, η_j cross. $f_{0c}(\gamma)$ is a non-analytic function too. Values of both $g(\gamma)$ and $f_{0c}(\gamma)$ were tabulated and are available in [59]. Both functions are positive and monotonously rising.

Usually, the interface energy σ is known as material property and l is chosen for computational convenience, together with γ . Then, the parameter values are assigned from the following formulae

$$\kappa = \sigma l \frac{\sqrt{f_{0c}(\gamma)}}{g(\gamma)} \approx \frac{3}{4} \sigma l \quad (4.8)$$

$$m = \frac{\sigma}{l} \frac{1}{g(\gamma) \sqrt{f_{0c}(\gamma)}} \approx 6 \frac{\sigma}{l} \quad (4.9)$$

$$L = \frac{\mu}{l} \frac{g(\gamma)}{\sqrt{f_{0c}(\gamma)}} \approx \frac{4}{3} \frac{\mu}{l} \quad (4.10)$$

The symbol μ stands for interface mobility. The approximate relations above hold exactly when $\gamma = 1.5$ and are well applicable when $0.9 \leq \gamma \leq 2.65$ [47].

4.3 Anisotropic model and parameters assignment strategies

Two cases of interface energy anisotropy may occur, together or separately. Firstly, in the system there may be multiple interfaces with different interface energies (termed *misorientation dependence* in [47], here *pair-wise isotropy* for greater generality). Secondly, there may be an interface with inclination-dependent interface energy. Additionally, the kinetic coefficient L can be inclination dependent.

In both cases of anisotropy in interface energy, some of the model parameters m, κ, γ must become spatially dependent in order to assure correct local representation of the interface energy and width. In other words, the equations (4.6) and (4.7) must hold in every point of the anisotropic system. These two equations locally form an undetermined system of three variables, hence one of the model parameters is free and many different parameters assignment strategies are possible.

In this paper, the parameter m is always a constant, because when m was spatially varied [47], the model behavior in multijunctions was reported to be strongly affected by the interface width. Such model would be non-quantitative and thus will not be further regarded in this paper.

Three different parameters assignment strategies are considered, which differ in value of m and further in which of parameters κ, γ is constant and which varies in space to keep equation (4.6) valid. The three strategies are denoted: IWc (variable γ, κ so that interface width is constant [47]), IWvG (variable interface width and γ [59]) and IWvK (variable interface width and κ). Table 4.1 summarizes, which parameters are kept constant and which vary to capture the anisotropy in the different strategies. The detailed procedure of the parameters assignment and ways to control the width of the narrowest interface are described in Appendix C. Note that for the IWc model we propose a single-step parameters determination procedure, which is more predictable and simpler than the original iterative one [47]. The two are equivalent, though.

Below follow details about the incorporation of pair-wise isotropy and inclination-dependence in the model.

4.3.1 Systems with pair-wise isotropic IE

In the system with n phase fields, there are $n(n-1)/2$ possible pair-wise interfaces, each of which may have different (mean) interface energy $\sigma_{i,j}$. The indices i, j denote interface between phase fields η_i, η_j . A set of parameters

Table 4.1: Characterization of the three parameter assignment strategies: the one with constant interface width (IWc), with variable interface width and all anisotropy in γ (IWvG) and with variable interface width and all anisotropy in κ (IWvK). In the latter, it is inconvenient to choose other value of γ than $\gamma = 1.5$. IW stands for interface width, other symbols have meaning as in the text.

	IWc	IWvG	IWvK
fixed parameters	IW, m	κ, m	γ, m
varying parameters	γ, κ	IW, γ	IW, κ

$m, \kappa_{i,j}, \gamma_{i,j}, L_{i,j}$ (all scalars) is obtained by appropriate procedure (depending on the strategy, see Appendix C) so that the relations (4.6) and (4.7) are valid for each interface independently (equations (4.8)-(4.10) hold for each interface (i - j)). Then, these are combined together to produce the model parameter fields $\kappa(\mathbf{r}), \gamma(\mathbf{r}), L(\mathbf{r})$:

$$\kappa(\mathbf{r}) = \frac{\sum_{i=1}^n \sum_{j>i}^n \kappa_{i,j} \eta_i^2 \eta_j^2}{\sum_{i=1}^n \sum_{j>i}^n \eta_i^2 \eta_j^2} \quad (4.11)$$

$$\gamma(\mathbf{r}) = \frac{\sum_{i=1}^n \sum_{j>i}^n \gamma_{i,j} \eta_i^2 \eta_j^2}{\sum_{i=1}^n \sum_{j>i}^n \eta_i^2 \eta_j^2}, \quad (4.12)$$

$$L(\mathbf{r}) = \frac{\sum_{i=1}^n \sum_{j>i}^n L_{i,j} \eta_i^2 \eta_j^2}{\sum_{i=1}^n \sum_{j>i}^n \eta_i^2 \eta_j^2} \quad (4.13)$$

which stand in place of κ, γ in the functional in equation (4.1) and in place of L in the governing equation (4.3).

Notice that from Table 4.1 stems that in IWvG is $\kappa(\mathbf{r}) = \text{const}$ by definition (i.e. all the $\kappa_{i,j}$ s are equal) and similarly in IWvK $\gamma(\mathbf{r}) = \text{const} = 1.5$ (i.e. all $\gamma_{i,j}$ s are equal).

The free energy functional for IWc is then (those for IWvG and IWvK are equal, only with either $\kappa(\mathbf{r})$ or $\gamma(\mathbf{r})$ being constants, respectively):

$$F = \int_V \left\{ m f_0(\vec{\eta}) + \frac{\kappa(\mathbf{r})}{2} \sum_{i=1}^n (\nabla \eta_i)^2 \right\} dV, \quad (4.14)$$

$$f_0(\vec{\eta}) = \sum_{i=1}^n \left(\frac{\eta_i^4}{4} - \frac{\eta_i^2}{2} \right) + \sum_{i=1}^n \sum_{i>j} \gamma_{i,j} \eta_i^2 \eta_j^2 + \frac{1}{4}. \quad (4.15)$$

Both parameter fields $\kappa(\mathbf{r}), \gamma(\mathbf{r})$ are functions of phase fields $\vec{\eta}$. This dependence should produce new terms in the governing equations (from $\partial f / \partial \eta_p$ in

equation (4.3)). However, because the denominator of $\gamma(\mathbf{r})$ cancels out in the functional, the new terms only arise from $\partial\kappa/\partial\eta_p$.

The governing equations then are

$$\begin{aligned} \frac{\partial\eta_p}{\partial t} = -L(\mathbf{r}) \left[m \left(\eta_p^3 - \eta_p + 2\eta_p \sum_{j \neq p} \gamma_{p,j} \eta_j^2 \right) \right. \\ \left. + \frac{1}{2} \frac{\partial\kappa}{\partial\eta_p} \sum_{i=1}^n (\nabla\eta_i)^2 - \kappa(\mathbf{r}) \nabla^2 \eta_p \right] \end{aligned} \quad (4.16)$$

The above procedure is fully variational, nevertheless inclusion of the term proportional to $\partial\kappa/\partial\eta_p$ enables the model to reduce the total energy of the system by introduction of so called third phase contributions (also ghost or spurious phases) at diffuse interfaces. [47] That is a common problem in multi-phase field models [67], where a third phase field attains non-zero value within an interface of two other phase fields. This mathematical artefact affects triple junction angles and in general is not physically justified. Several ways of elimination or suppression of ghost phases were described in [67] and the references therein.

In this work, the ghost phases were eliminated by neglecting the term proportional to $\partial\kappa/\partial\eta_p$. However, because such model is not fully variational, the thermodynamic consistency can no longer be guaranteed in IWc and IWvK. This does not affect IWvG, because there is $\partial\kappa/\partial\eta_p = 0$ anyway. That accounts for a clear advantage of the IWvG model, as no ghost phases appear even when fully variational.

4.3.2 Systems with inclination-dependent interface energy

The orientation of an interface in 2D system is given by interface normal, inclined under the angle θ . Local value of interface energy may be a function of local interface inclination, i.e. $\sigma = \sigma(\theta)$. In Moelans' model [47], the normal at interface between η_i, η_j , denoted $\hat{\mathbf{n}}_{i,j}$, is defined as

$$\hat{\mathbf{n}}_{i,j} = \frac{\nabla\eta_i - \nabla\eta_j}{|\nabla\eta_i - \nabla\eta_j|} = \begin{bmatrix} (\hat{n}_{i,j})_x \\ (\hat{n}_{i,j})_y \end{bmatrix} \quad (4.17)$$

and the definite inclination of that normal

$$\theta_{i,j} = \text{atan2}[(\hat{n}_{i,j})_y, (\hat{n}_{i,j})_x], \quad (4.18)$$

Table 4.2: Inclination dependence of the variable parameters in the respective models. The interface energy is $\sigma_{i,j}(\theta_{i,j}) = \sigma_{i,j}^0 h_{i,j}(\theta_{i,j})$. Symbols $\kappa_{i,j}^0$, $\gamma_{i,j}^0$ stand for scalar values of the parameters determined from $\sigma_{i,j}^0$ (see C in [44]). Expressions for $\gamma_{i,j}(\theta_{i,j})$ follow the so called *weak anisotropy approximation* [47], i.e. they assume that the values of $\gamma_{i,j}(\theta_{i,j})$ do not diverge far from 1.5, so that the approximation $g^2[\gamma_{i,j}(\theta_{i,j})] \approx 16[2\gamma_{i,j}(\theta_{i,j}) - 1]/9[2\gamma_{i,j}(\theta_{i,j}) + 1]$ is applicable (see [47] for details). Second row contains expressions used in equations 4.23 and 4.24.

model	IWc	IWvG	IWvK
variable parameter(s)	$\kappa_{i,j}(\theta_{i,j}) = \kappa_{i,j}^0 h_{i,j}(\theta_{i,j})$ $\gamma_{i,j}(\theta_{i,j}) = -\frac{\frac{9}{2}g^2(\gamma_{i,j}^0)h_{i,j}(\theta_{i,j})+1}{\frac{9}{2}g^2(\gamma_{i,j}^0)h_{i,j}(\theta_{i,j})-2}$	$\gamma_{i,j}(\theta_{i,j}) = -\frac{\frac{9}{2}[g(\gamma_{i,j}^0)h_{i,j}(\theta_{i,j})]^2+1}{\frac{9}{2}[g(\gamma_{i,j}^0)h_{i,j}(\theta_{i,j})]^2-2}$ $\kappa_{i,j}(\theta_{i,j}) = \kappa_{i,j}^0 [h_{i,j}(\theta_{i,j})]^2$	
$\partial\kappa_{i,j}/\partial h_{i,j}$ and $\partial\gamma_{i,j}/\partial h_{i,j}$	$\partial\kappa_{i,j}/\partial h_{i,j} = \kappa_{i,j}^0$ $\partial\gamma_{i,j}/\partial h_{i,j} = \frac{9g^2(\gamma_{i,j}^0)}{[\frac{9}{2}g^2(\gamma_{i,j}^0)h_{i,j}(\theta_{i,j})-2]^2}$	$\partial\gamma_{i,j}/\partial h_{i,j} = \frac{18g^2(\gamma_{i,j}^0)h_{i,j}(\theta_{i,j})}{\{\frac{9}{2}[g(\gamma_{i,j}^0)h_{i,j}(\theta_{i,j})]^2-2\}^2}$ $\partial\kappa_{i,j}/\partial h_{i,j} = 2\kappa_{i,j}^0 h_{i,j}(\theta_{i,j})$	

which is the standard 2-argument arctangent function.

In 2D, the inclination-dependence of interface energy can be expressed as

$$\sigma_{i,j}(\theta_{i,j}) = \sigma_{i,j}^0 h_{i,j}(\theta_{i,j}) \quad (4.19)$$

where $\sigma_{i,j}^0$ is a scalar and $h_{i,j}(\theta_{i,j})$ is anisotropy function. The used anisotropy function was

$$h_{i,j}(\theta_{i,j}) = 1 + \delta \cos(n\theta_{i,j}), \quad (4.20)$$

with δ being strength of anisotropy and n the order of symmetry. Some properties of this anisotropy function and the resulting Wulff shapes are given in 2.5.

The inclination dependence of $\sigma_{i,j}$ implies that some of the model parameters $\gamma_{i,j}, \kappa_{i,j}$ must be taken inclination-dependent too. Depending on the model used (IWc, IWvG or IWvK), the local validity of equation (4.6) is achieved using different inclination dependence of the variable parameters (see Table 4.2 for details).

Because the inclination-dependent $\kappa_{i,j}, \gamma_{i,j}$ are functions of components of gradients $\nabla\eta_i, \nabla\eta_j$, the divergence term in the functional derivative (equation (4.3)) produces additional driving force terms. In the general case with multiple inclination-dependent interfaces, the divergence term equals

$$\begin{aligned} \nabla \cdot \frac{\partial f}{\partial(\nabla\eta_p)} &= 2m\eta_p \nabla\eta_p \cdot \left[\sum_{j \neq p} \eta_j^2 \frac{\partial \gamma_{p,j}}{\partial(\nabla\eta_p)} \right] \\ &\quad + 2m\eta_p^2 \sum_{j \neq p} \left[\eta_j \nabla\eta_j \cdot \frac{\partial \gamma_{p,j}}{\partial(\nabla\eta_p)} \right] \\ &\quad + m\eta_p^2 \sum_{j \neq p} \eta_j^2 \left[\nabla \cdot \frac{\partial \gamma_{p,j}}{\partial(\nabla\eta_p)} \right] \\ &\quad + \frac{1}{2} \left[\nabla \cdot \frac{\partial \kappa}{\partial(\nabla\eta_p)} \right] \sum_{i=1}^n (\nabla\eta_i)^2 \\ &\quad + \frac{1}{2} \frac{\partial \kappa}{\partial(\nabla\eta_p)} \cdot \left[\nabla \sum_{i=1}^n (\nabla\eta_i)^2 \right] \\ &\quad + \nabla\kappa(\mathbf{r}) \cdot \nabla\eta_p + \kappa(\mathbf{r}) \nabla^2 \eta_p. \end{aligned} \quad (4.21)$$

The vector field $\partial\kappa/\partial(\nabla\eta_p)$ is

$$\frac{\partial\kappa}{\partial(\nabla\eta_p)} = \frac{\sum_{j \neq p}^n \left(\frac{\partial\kappa_{p,j}}{\partial(\nabla\eta_p)} \right) \eta_p^2 \eta_j^2}{\sum_{k=1}^n \sum_{l>k} \eta_k^2 \eta_l^2} \quad (4.22)$$

where the sum in the numerator goes through all pair-wise interfaces of $\eta_p(\mathbf{r})$. The vector fields $\partial\kappa_{p,j}/\partial(\nabla\eta_p)$ are expressed

$$\frac{\partial\kappa_{p,j}}{\partial(\nabla\eta_p)} = \frac{1}{|\nabla\eta_i - \nabla\eta_j|} \frac{\partial\kappa_{p,j}}{\partial h_{p,j}} \frac{\partial h_{p,j}}{\partial \theta_{p,j}} \begin{bmatrix} -(\hat{n}_{i,j})_y \\ (\hat{n}_{i,j})_x \end{bmatrix}. \quad (4.23)$$

Note, that the above vector field is nonzero only in IWc and IWvK models at the interfaces $(p-j)$ with inclination-dependent IE. Likewise, the below vector field is nonzero only in IWc and IWvG

$$\frac{\partial\gamma_{p,j}}{\partial(\nabla\eta_p)} = \frac{1}{|\nabla\eta_i - \nabla\eta_j|} \frac{\partial\gamma_{p,j}}{\partial h_{p,j}} \frac{\partial h_{p,j}}{\partial \theta_{p,j}} \begin{bmatrix} -(\hat{n}_{i,j})_y \\ (\hat{n}_{i,j})_x \end{bmatrix}. \quad (4.24)$$

The multipliers $\partial\kappa_{p,j}/\partial h_{p,j}$ and $\partial\gamma_{p,j}/\partial h_{p,j}$ differ in individual models and are also provided in Table 4.2. The term $\partial h_{p,j}/\partial \theta_{p,j}$ is defined by the inclination-dependence at the interface $(p-j)$.

The governing equation then is

$$\begin{aligned} \frac{\partial\eta_p}{\partial t} = -L(\mathbf{r}) \left[m \left(\eta_p^3 - \eta_p + 2\eta_p \sum_{j \neq p} \gamma_{p,j}(\theta_{p,j}) \eta_j^2 \right) \right. \\ \left. - \nabla \cdot \frac{\partial f}{\partial(\nabla\eta_p)} \right]. \end{aligned} \quad (4.25)$$

Note, that the term proportional to $\partial\kappa/\partial\eta_p$ was neglected here.

In models with variable interface width (IWvG, IWvK), at the interfaces with inclination-dependent interface energy, the interface width is a function of the inclination, i.e. $l_{i,j} = l_{i,j}(\theta_{i,j})$. Because the kinetic coefficient $L_{i,j}$ is inversely proportional to the interface width $l_{i,j}$ (see equation (4.10)), the kinetic coefficient is inclination-dependent as well (even for *constant* grain boundary mobility $\mu_{i,j}$). The inclination dependence of $L_{i,j}(\theta_{i,j})$ due to interface width variation is in the IWvG model

$$L_{i,j}(\theta_{i,j}) = L_{i,j} h_{i,j}(\theta_{i,j}) \quad (4.26)$$

and in the IWvK model

$$L_{i,j}(\theta_{i,j}) = L_{i,j}/h_{i,j}(\theta_{i,j}), \quad (4.27)$$

where $h_{i,j}(\theta_{i,j})$ is the anisotropy function in interface energy (4.19).

The equations (4.26),(4.27) were derived from an alternative expression for the kinetic coefficient $L_{i,j}$

$$L_{i,j} = \frac{\mu_{i,j}\sigma_{i,j}(\theta_{i,j})}{\kappa_{i,j}(\theta_{i,j})}, \quad (4.28)$$

where the inclination dependencies of the right-hand side were expressed correspondingly to the model (see Table 4.2 for $\kappa_{i,j}(\theta_{i,j})$).

Due to varying number of driving force terms in the three parameter assignment strategies, the governing equations are different in each and hence it is justified to call them different models.

Systems with inclination-dependent mobility

Let the interface (i - j) have isotropic interface energy and inclination-dependent grain boundary mobility with anisotropy function $h_{i,j}^\mu(\theta_{i,j})$, i.e. $\mu_{i,j} = \mu_{i,j}(\theta_{i,j}) = \mu_{i,j}^0 h_{i,j}^\mu(\theta_{i,j})$. From equation (4.10) we can see that the kinetic coefficient must have the same anisotropy, i.e. $L_{i,j}(\theta_{i,j}) = L_{i,j}^0 h_{i,j}^\mu(\theta_{i,j})$, where $L_{i,j}^0 = \mu_{i,j}^0 g(\gamma_{i,j})/l_{i,j} f_{0c}(\gamma_{i,j})$.

If the interface energy is inclination-dependent as well and a model with variable interface width is used (either IWvG or IWvK), the inclination dependence in $L_{i,j}(\theta_{i,j})$ due to the interface width variation must be included similarly like in (4.26) and (4.27). The physical inclination-dependence is independent from the one due to interface width variation, implying the following expression for IWvG model

$$L_{i,j}(\theta_{i,j}) = L_{i,j}^0 h_{i,j}(\theta_{i,j}) h_{i,j}^\mu(\theta_{i,j}) \quad (4.29)$$

and for the IWvK model analogically

$$L_{i,j}(\theta_{i,j}) = L_{i,j}^0 \frac{h_{i,j}^\mu(\theta_{i,j})}{h_{i,j}(\theta_{i,j})}, \quad (4.30)$$

where $h_{i,j}(\theta_{i,j})$ is the interface energy anisotropy function.

4.3.3 Interface profiles in different models

The main difference in the model modifications is how the interface width varies as function of local interface energy. Obviously, in IWc the width is constant.

In IWvK (with $\gamma = 1.5$) the width of interface i - j can be computed as

$$l_{i,j} = 6 \frac{\sigma_{i,j}}{m}. \quad (4.31)$$

Apparently, in IWvK model the interface width is proportional to the interface energy, i.e. the larger the interface energy, the larger the interface width.

In IWvG the width can be expressed from (4.7) and (4.6) assuming $\frac{4}{3}\sqrt{f_{0,c}}(\gamma_{i,j}) = g(\gamma_{i,j})$ (which holds for small values of $\gamma_{i,j}$). Then, it goes approximately

$$l_{i,j} \approx \frac{\kappa}{\sigma_{i,j}}, \quad (4.32)$$

and apparently the larger interface energies are associated with lower interface widths in IWvG.

4.4 General Neumann boundary conditions to control interface inclination at domain boundary

This model extension was inspired by [20]. It allows to control the interface inclination angle ϕ at the boundary, which thus becomes an input parameter. The principle is explained using a single phase field $\eta(\mathbf{r})$. First, we remark that the Neumann BCs $\nabla\eta \cdot \mathbf{n}_D = 0$ must be a special case of the general BC (\mathbf{n}_D is the domain boundary normal). The Neumann BC implies perpendicularity of the PF gradient and domain boundary normal. In other words, the interface is perpendicular to the domain boundary. Generally, we can write $\mathbf{n}_D \cdot \nabla\eta = |\nabla\eta| \cos(\phi)$. In the model by Granasy [20], the local magnitude of phase field gradient may be expressed using the local phase field value, giving rise to expression of the boundary condition as

$$\mathbf{n}_D \cdot \nabla\eta = \frac{\cos(\phi)}{\delta\sqrt{2}}\eta(1-\eta), \quad (4.33)$$

where δ is the interface width. At the domain boundary, the gradient $\nabla\eta$ is expressed as a polynomial, which allows straightforward implementation of the condition, especially in rectangular simulation domains.

In Moelan's model the interface normal between the phase fields η_i, η_j denoted $\mathbf{n}_{i,j}$ is defined as local difference in neighboring PF gradients (see equation 4.17). In the spirit of the introductory example we can write

$$\mathbf{n}_D \cdot \mathbf{n}_{i,j} = \cos(\phi) \implies \mathbf{n} \cdot (\nabla\eta_i - \nabla\eta_j) = |\nabla\eta_i - \nabla\eta_j| \cos(\phi). \quad (4.34)$$

Now we have single BC with the correct physical interpretation (fixed inclination angle at the boundary) but because the governing equations are solved for the phase fields, a set of equivalent boundary conditions (one for each phase field) must be derivable from the above. In these independent BC, it must be possible to express the gradient magnitude (the introductory example finds a polynomial of local PF values equal to the gradient magnitude).

The first problem (coupling in the BC) would be solved if one gradient could be written as a function of the other and vice versa. However, this dependence is non-analytical for all $\gamma_{i,j} \neq 1.5$. For $\gamma_{i,j} = 1.5$ it is simply $\eta_i = 1 - \eta_j$ and therefore also $\nabla\eta_i = -\nabla\eta_j$. [47]

The second problem (the expression for gradient magnitude) is also enabled by the choice $\gamma = 1.5$, as in such case there were derived analytic expressions for the gradients $\nabla\eta_i, \nabla\eta_j$. [47] In 1D system with 2 phase fields holds

$$\begin{aligned} \frac{d\eta_i}{dx} &= \sqrt{\frac{2m}{\kappa_{i,j}}} \eta_i (1 - \eta_i) \stackrel{2D,3D}{=} |\nabla\eta_i| \\ \frac{d\eta_j}{dx} &= \sqrt{\frac{2m}{\kappa_{i,j}}} \eta_j (1 - \eta_j) \stackrel{2D,3D}{=} |\nabla\eta_j|. \end{aligned} \quad (4.35)$$

Validity of the last equation sign in 2D and 3D (in systems with 2 phase fields) can be checked using the expressions in [47] as follows. Write the equation 7 from [47] for 2D. From it one gets 2D equivalents of equations 8a and 8b, where $\frac{d\eta}{dx}$ is replaced by $|\nabla\eta|$. Further, because the equation 19 does not depend on problem dimensionality, we obtain here the expressions in equation 4.35. In systems with more than two phase fields the general expression for the gradient magnitude is more complex. However, the same relations are satisfied at a pair-wise interface not close to the triple junction.

With the above and assuming that there is no triple junction near the domain boundary, we can thus write

$$\begin{aligned} \mathbf{n} \cdot (\nabla\eta_i - \nabla\eta_j) &= 2\mathbf{n} \cdot \nabla\eta_i = 2|\nabla\eta_i| \cos(\phi) \\ &= -2\mathbf{n} \cdot \nabla\eta_j = -2|\nabla\eta_j| \cos(\phi), \end{aligned} \quad (4.36)$$

which provides very similar BC like in the introductory example for each of the two phase fields.

The only way how to use these relations is to have $\gamma_{i,j} = 1.5$. In the case of inclination-dependent interface energy $\sigma_{i,j}(\theta_{i,j}) = \sigma_{i,j}^0 h_{i,j}^\sigma(\theta_{i,j})$, it is necessary to express the anisotropy fully by the parameter $\kappa_{i,j}(\theta_{i,j})$.

4.5 Volume conserving multi phase field models

There are several approaches which accomplish the volume conservation of some species or phases. Each has its drawbacks though. It was not clear which of the possible approaches was the most convenient for coupling with inclination-dependent interface energy in curvature-driven systems.

Three conceptual solutions can be used in a multi-phase field model, which are known to the author: Cahn-Hilliard equation, Lagrange multipliers and fictitious concentrations field.

Given the intended application with anisotropic interface energy and the complicated driving force, a less computationally demanding option than the Cahn-Hilliard equation was sought, because that one is a partial differential equation of 4-th order in space.

The approach using Lagrange multipliers to conserve volume was thoroughly considered, but eventually it was found out that in Moelan's model is not a suitable solution. The reason is that the volume of a single phase/grain is defined using all other phase fields, which introduces excessive computational complexity in application of the principles leading to volume conservation. These findings were documented in Appendix E.

The approach using fictitious concentration field is not new in combination with Moelans' multi-phase field model (see e.g. [74, 76]), but it will be reviewed.

4.5.1 Fictitious concentration field

The idea is to couple the AC equation to conserved concentration field in such a way that the change in phase fraction is only possible with exchange of species between phases. If the concentration of the independent species is set to equilibrium value no phase transformation occurs and the volume of the phase fraction should be conserved.

In the description below, it is assumed that there are two phases, one solid and the other liquid.

The free energy functional is then

$$F_{cons} = \int_V [f_{hom}(\vec{\eta}, \nabla \vec{\eta}, c) + f_{grad}(\vec{\eta}, \nabla \vec{\eta})] dV, \quad (4.37)$$

with

$$f_{hom}(\vec{\eta}, \nabla \vec{\eta}, c) = f_0(\vec{\eta}, \nabla \vec{\eta}) + f_{chem}(\vec{\eta}, c) \quad (4.38)$$

$$f_{chem}(\vec{\eta}, c) = h_S(\vec{\eta})f_S(c) + h_L(\vec{\eta})f_L(c) \quad (4.39)$$

$h_S(\vec{\eta}), h_L(\vec{\eta})$ are solid and liquid interpolation functions. Assuming that the solid phase is composed of s phase fields $\eta_{S1}, \eta_{S2}, \dots, \eta_{Ss}$ and the liquid phase of l phase fields $\eta_{L1}, \eta_{L2}, \dots, \eta_{Ll}$ we can write

$$h_S(\vec{\eta}) = \frac{\sum_i^s \eta_{Si}^2}{\sum_i^s \eta_{Si}^2 + \sum_j^l \eta_{Lj}^2} \quad (4.40)$$

$$h_L(\vec{\eta}) = \frac{\sum_j^l \eta_{Lj}^2}{\sum_i^s \eta_{Si}^2 + \sum_j^l \eta_{Lj}^2} \quad (4.41)$$

Parabolic energy approximation will be used for the concentration dependence of the homogeneous phase free energy densities $f_S(c), f_L(c)$ as

$$f_S(c_S) = A(c_S - c_{S,eq})^2 \quad (4.42)$$

$$f_L(c_L) = B(c_L - c_{L,eq})^2 \quad (4.43)$$

An ideal solution approximation is adopted.

The governing equations for two phase fields are then

$$\frac{\partial \eta_1}{\partial t} = -L \left[\frac{\partial f_0}{\partial \eta_1} - \nabla \cdot \frac{\partial F}{\partial (\nabla \eta_1)} + \frac{\partial h_S}{\partial \eta_1} [f_S(c_S) - f_L(c_L) - (c_S - c_L)\mu] \right] \quad (4.44)$$

$$\frac{\partial \eta_2}{\partial t} = -L \left[\frac{\partial f_0}{\partial \eta_2} - \nabla \cdot \frac{\partial F}{\partial (\nabla \eta_2)} + \frac{\partial h_S}{\partial \eta_2} [f_S(c_S) - f_L(c_L) - (c_S - c_L)\mu] \right] \quad (4.45)$$

$$\mu = 2A(c_L - c_{L,eq}) \quad (4.46)$$

$$\frac{\partial c}{\partial t} = \frac{D}{A} \Delta \mu = 2D\Delta(c_L - c_{L,eq}) \quad (4.47)$$

where the diffusion coefficient D is a constant.

The interpolation functions have the following property

$$\frac{\partial h_S}{\partial \eta_p} = -\frac{\partial h_L}{\partial \eta_p} \quad (4.48)$$

4.6 Summary and the author's contribution

The author extended the multi-phase field model by Moelans [47]. The work [47] promoted usage of the model variant with constant interface width (here denoted IWc) with not-fully-variational formulation and described it in great detail.

At the beginning of the author's work, it was already known that IWc was not reliably reproducing the angles in triple junctions of interfaces with different interface energies [49] (i.e. in pair-wise isotropic systems). The model variant with variable interface width and all anisotropy in the parameter γ (here IWvG) was used in one grain growth study [59], but its better reliability in triple junction angles had not been documented yet.

As provided below with all details, the model extensions included

1. Description of another model variant with all anisotropy in the parameter κ and variable interface width (IWvK)
2. Derivation of the governing equation for all the three model variants in both 2D and 3D for the case of inclination-dependent interface energy
3. The model behavior depends heavily on proper parametrization of the equations. Best practices in parameters determination were developed and described (different in each model variant) in order to assure control over both the local interface width and local interface energy.
4. In the IWvK model variant such boundary conditions were incorporated, which allowed to control the angle under which the interface intersecting the domain boundary will align.

Besides the listed model extensions, the author also implemented two approaches adding the volume conservation to the system based on Allen-Cahn type of equations, namely one using Lagrange multipliers to conserve the volume and one using fictitious concentration field. Volume conservation would be necessary in simulations, where the nucleus interacted dynamically with its surroundings, but these simulations were not needed eventually. Regardless, the model modifications including volume conservation were described in Appendix.

Chapter 5

Phase field model benchmarking

5.1 Introduction

This chapter proposes two benchmarks for quantitative assessment of a) the anisotropic curvature driving force, and b) the anisotropic curvature driving force in combination with anisotropic kinetic coefficient. Both are 2-phase systems, hence could be simulated using a single phase field model. Nevertheless, because the multi-phase field models allow simulations of multiple phases, they have wider application potential than single phase models. For this reason, the validations are demonstrated on a multi-phase field model from chapter 4. However, the nature of these benchmarks is independent on the model formulation.

In order to provide more complete comparison of the model variants, another supplementary benchmark was carried out, which determined equilibrium triple junction angles.

Throughout this chapter the term "Wulff shape" is used in place of "Wulff shape of the first order" (see section 2.1), i.e. the smallest of the possible equilibrium stable shapes.

This chapter first provides details on the numerical implementation of the model(s) in MATLAB, then the methodology is explained and the models quantitatively compared. The first two benchmarks involve quantitative matching of the shrinking shape to the analytic one and also the determination of shrinkage rate. In the third benchmark, the triple junction angles are determined

from the phase field contour using two different approaches. For all simulations the effect of interface width and number of grid points through the interface are investigated by re-running the simulations using different numerical settings.

5.2 Numerical implementation

All models were implemented in a single MATLAB function, where the governing equations were solved by centered finite differences of second order, explicit Euler time stepping and boundary conditions implemented using ghost nodes. For more details on the used finite difference schemes, refer to the Appendix D. The minimal code to run the simulations is available in the dataset [40].

During the parameters assignment in models with variable interface width (IWvG, IWvK), there was assured control over the minimal interface width, i.e. that there would be no interface narrower than the user-specified one. That is to prevent unphysical behavior of the interface due to too small grid resolution. Different strategies had to be adopted in IWvK and IWvG, respectively. They are described in Appendix C together with other best practices in parameters determination for the respective models. The MATLAB functions which were used for parameters determination were also included in the dataset [40].

In the simulations with inclination-dependent interface energy, the vector field $\partial\kappa/\partial(\nabla\eta_p)$ was computed as in equations (4.22) and (4.23), the fields $\partial\gamma_{p,j}/\partial(\nabla\eta_p)$ as in equation (4.24) and their divergences (see equation (4.21)) were computed numerically (by centered differences), as well as the gradient $\nabla\kappa(\mathbf{r})$. All the above terms were computed in the IWc model, whereas in the models with variable interface width some of them could be omitted (as explained in section 4.3.2).

When the anisotropy in inclination-dependent interface energy was strong (i.e. $\delta > 1/(n^2 - 1)$ or $\Omega > 1$), the anisotropy function had to be regularized as described in [17] in order to avoid ill-posedness of the governing equations for interfaces with missing inclination.

In finite difference method, the ratio of the time step Δt to the grid spacing Δx determines the numeric stability of the simulation. Specifically, the so-called Courant number C must be $0 < C < 0.5$, where in this model

$$C = \min[\kappa(\mathbf{r})L]\Delta t/(\Delta x)^2. \quad (5.1)$$

In practice, the time step was computed using equation (5.1) assuming the value of $C \leq 0.3$. For stronger anisotropies C had to be reduced farther. When $0.129 \leq \sigma_{min}/\sigma_{max} \leq 0.2$, the value $C = 0.12$ was used, when $0.2 < \sigma_{min}/\sigma_{max} \leq 0.3$, $C = 0.17$ and for $\sigma_{min}/\sigma_{max} > 0.3$ the used Courant number

Table 5.1: Parameters from equation (5.2) describing anisotropic dependence of the Courant number C in simulations with inclination-dependent interface energy and strong anisotropy $\Omega > 1$.

	IWc	IWvG	IWvK
a	1.38	1.43	0.98
b	1.95	1.91	2.35

was $C = 0.3$. The latter value of Courant number was also applied in simulations with inclination-dependent interface energy and smooth Wulff shapes ($\Omega \leq 1$). For cornered Wulff shapes ($\Omega > 1$), the following dependence was obtained from visual inspection of the interface normal inclination field $\theta(\mathbf{r})$ defined in equation (18) ($\theta(\mathbf{r})$ was sensitive to the numeric instabilities) during the simulation

$$C(\Omega) = \frac{1}{a\Omega + b}. \quad (5.2)$$

The Table 5.1 contains the values of a, b in the respective model modifications.

The following 9-point stencil was used for computation of the laplacian in grid point (k, l)

$$\begin{aligned}
 (\nabla^2 \eta)_{k,l} = & \frac{1}{6h^2} [4(\eta_{k-1,l} + \eta_{k+1,l} \eta_{k,l-1} + \eta_{k,l+1}) \\
 & + \eta_{k+1,l+1} + \eta_{k-1,l-1} + \eta_{k-1,l+1} + \eta_{k+1,l-1} \\
 & - 20\eta_{k,l}]. \quad (5.3)
 \end{aligned}$$

When the interface energy is inclination-dependent, it can be seen in equations (4.23), (4.24) that some driving force terms are proportional to $1/|\nabla\eta_i - \nabla\eta_j|$. In fact, some are even proportional to $1/|\nabla\eta_i - \nabla\eta_j|^3$ when worked out analytically. Far enough from the interface, the magnitude $|\nabla\eta_i - \nabla\eta_j|$ inevitably gets smaller than the numeric resolution, which causes severe numeric instabilities due to locally very large driving forces. For this reason, all the driving force terms from equation (4.21) were only computed in a region close enough to the interface. Two such regions $\Gamma_{out}, \Gamma_{inn}$ (outer and inner) were selected based on local value of $|\nabla\eta_i - \nabla\eta_j|$ (see Figure 5.1). The region Γ_{inn} was a subset of Γ_{out} . The interface inclination field $\theta_{i,j}$ was computed in Γ_{out} , where $|\nabla\eta_i - \nabla\eta_j|^3(\Delta x)^3 > C_{out}^3$ and the driving force terms $\nabla \cdot \partial f / \partial (\nabla\eta_p)$ were computed in region Γ_{inn} where $|\nabla\eta_i - \nabla\eta_j|^3(\Delta x)^3 > C_{inn}^3$. The constants $C_{out} = 10^{-6}$ and $C_{inn} = 0.005$ have the meaning of minimal local change in value of phase field which is acceptable to the respective near-interface region (this is exactly true for $\gamma = 1.5$ and approximate otherwise). Note, that the driving force from homogeneous free energy density (i.e. $\partial f / \partial \eta_p$) and the

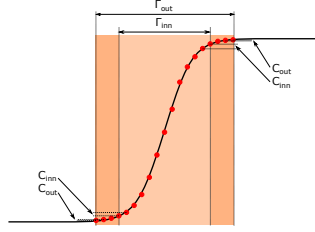


Figure 5.1: Illustration of the near-interface regions $\Gamma_{out}, \Gamma_{inn}$, defined by absolute values of difference in phase fields between neighbouring points.

laplacian term $\kappa(\mathbf{r})\nabla^2\eta_p$ were computed and applied in the whole simulation domain.

In the Wulff shape simulations, the accuracy of match to the analytical shape with IWvG phase field contour turned out to be sensitive to alignment of the shape within the numerical grid. For strong anisotropies $\Omega > 1$, when the corner laid exactly on some grid line, the IWvG contours were slightly deformed, making the model perform seemingly worse than IWc and IWvK (which were not affected by this). This problem was solved by shifting the center of the initial shape by half a pixel in both x and y direction. No corner than laid on any grid line and that solved the problem. Rotating the Wulff shape relative to the grid had similar effect. All the results in the main text were simulated with the shifted initial shape. This is not likely to play significant role in grain growth simulations as the corner motion along grid line is very unlikely with arbitrary grain structure and local grain orientation.

5.3 Methodology

Three different simulation experiments were performed: a shrinking Wulff shape, kinetically compensated anisotropic curvature-driven circle shrinkage and triple junction angles. The initial-state geometries and grid dimensions are in Figure 5.2. Except for the shrinking circles simulation, a parametric study was carried out in every experiment in order to validate the model behavior. Table 5.2 summarizes the variable parameters in every experiment.

Each of the experiments was simulated using all the three model modifications (IWc, IWvG and IWvK) successively and the results were quantitatively compared.

In order to distinguish the behavior of the model from the artefacts of numeric

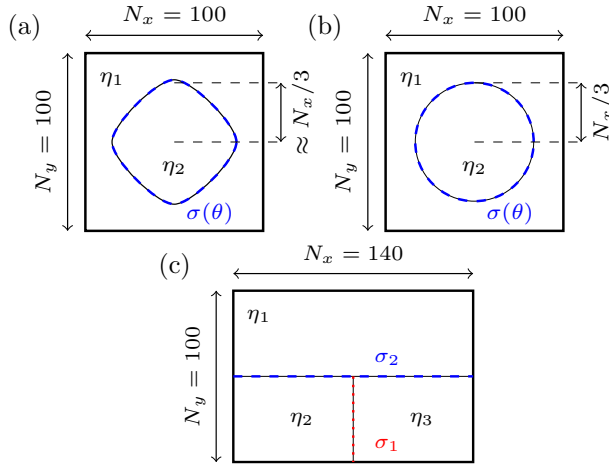


Figure 5.2: Initial conditions in the different numeric experiments with indicated interface energies. In a) Wulff shape shrinkage, b) kinetically compensated anisotropic curvature-driven circle shrinkage and c) measurement of triple junction angle. Grid dimensions correspond to the base run and 1000IW run (see text for details). All interfaces have equal mobilities.

Table 5.2: Overview of the simulations carried out in every simulation experiment. Note that these were carried out in every model modification (i.e. IWc, IWvG and IWvK) and simulation run (see Table 5.3). Number of simulations in every experiment is provided in the column Count. See text for more details.

Experiment	Varied par.	Values	Count
Wulff shape	Ω (-)	0.2, 0.4, 0.6, 0.8, 1.0, 2.3, 3.6, 4.9, 6.2, 7.5	10
Kin.comp.aniso. circle	Ω (-)	0.1, 0.3, 0.5, 0.7, 0.9	5
Triple junction	σ_1/σ_2 (-)	0.13, 0.2, 0.3, 0.4, 0.5, 0.6, 0.7, 0.8, 0.9, 1.0, 1.1, 1.2, 1.3, 1.4, 1.5, 1.6, 1.7, 1.8, 1.9, 2.0	20

Table 5.3: Numeric settings of different simulation runs (for each simulation experiment and model). l_{min} is the minimal interface width. N_x and N_y are grid dimensions in the base run as shown in Figure 5.2

	base run	IW/2	14IWpts	1000IW
grid dimensions	$N_x \times N_y$	$2N_x \times 2N_y$	$2N_x \times 2N_y$	$N_x \times N_y$
l_{min} (nm)	1	0.5	1	1000
points in l_{min}	7	7	14	7

discretization, the above described series of simulations was re-run for several numeric settings. Throughout the paper, these large series are called 'runs'.

Results of four runs are presented in this paper, the basic settings of which are summarized in Table 5.3. The difference between the runs were: a) the minimal set interface width l_{min} and b) the number of points in the interface. The runs are denoted base run, IW/2, 14IWpts and 1000IW. The base run had rather coarse grid and 7 points in the interface, which should in general be reliable yet not very computationally heavy settings. The minimal interface width was $l_{min} = 1$ nm. In the run IW/2 the interface width was halved ($l_{min} = 0.5$ nm) and the number of points in the interface was 7 again. In the 14IWpts run, the interface width was as in the base run but the points in the interface were doubled (to be 14). Physical dimensions of the simulated domain were equal in the described runs but the grid spacing was halved in IW/2 and 14IWpts runs. In the last 1000IW run, the grid was equal as in the base run, but the physical dimensions were scaled by a factor of 1000, meaning the minimal interface width $l_{min} = 1$ μ m. This is the practical settings for the actual grain growth simulations. The latter run validated that the meso-scale behavior of the model is equal to that one at the nanometer scale.

In the simulation experiments, position of the interface in the respective geometry was compared to the expected shape. Depending on the parameters assignment strategy, the phase field profiles may not be symmetric about the point 0.5 in Moelans' model. For this reason, it was considered that the position of the interface i - j was in points $\mathbf{r} = (x, y)$ of the domain, where $\eta_i(\mathbf{r}) = \eta_j(\mathbf{r})$, i.e. where the two profiles crossed. This way the contours were always well defined and could be quantitatively compared to appropriate analytical models even for Wulff shape simulations, where the profile shape varies along the interface.

The below subsections describe in detail the analytic solutions of the problems and results processing in the individual simulation experiments.

5.3.1 Used anisotropy function and its Wulff shape

The anisotropy function $h(\theta) = 1 + \delta \cos(n\theta)$ was used, together with the normalized strength of anisotropy $\Omega = \delta(n^2 - 1)$. Ω easily distinguishes weak from strong anisotropy, because for $0 < \Omega < 1$ the Wulff shape is smooth, whereas for $1 \leq \Omega < n^2 - 1$ it has corners. Section 2.5 provides more details about this anisotropy function. Fourfold symmetry was assumed (i.e. $n = 4$).

Ill-posedness of the governing equations for forbidden orientations on Wulff shapes for strong anisotropies ($\Omega > 1$) was treated by regularization of the anisotropy function as in [17].

For validation of the kinetics of shrinkage, an analytic expression for Wulff shape shrinkage rate was derived in 2.6. Measurement of area/volume occupied by a grain/phase is trivial in phase field method, hence the rate of its change (i.e. the shrinkage rate) can be easily used for validation or benchmark. The derivation in [44] delivers the expression

$$\frac{dA_W}{dt} = -2\pi\mu\sigma_0 \frac{C_W(\Omega, n)}{1 - \delta} \quad (5.4)$$

where $C_W(\Omega, n) = A_W/A_{circle}$ is an anisotropic factor relating the area of a Wulff shape and a circle of equal radius. For fourfold symmetry it was numerically computed and fitted by polynomial $C_W(\Omega, 4) = \sum_{i=0}^4 a_i \Omega^{N-i}$ with $a_0 = -0.00032, a_1 = 0.00639, a_2 = -0.04219, a_3 = 0.00034, a_4 = 1.00000$ (rounded to the relevant decimal digits). As can be seen, the analytic shrinkage rate is a constant, which is consistent with [64].

With isotropic interface energy ($\delta = \Omega = 0$) the steady state shape is a circle and the anisotropic factor is $C_W/(1 - \delta) = 1$, hence the isotropic curvature-driven shrinkage rate of a circle is (as also e.g. in [51])

$$\frac{dA}{dt} = -2\pi\mu\sigma_0. \quad (5.5)$$

5.3.2 Quantifying the match in shape

The *Hausdorff distance* was used for quantification of the match in shape. Let the 2D curves $\mathbf{w}, \mathbf{w}_{PF}$ be the analytic shape and the phase-field contour, respectively. The Hausdorff distance $d_H(\mathbf{w}, \mathbf{w}_{PF}) = \lambda$ between them implies, that λ is the smallest number such that \mathbf{w} is completely contained in λ -neighborhood of \mathbf{w}_{PF} and vice-versa [3]). Formally, it is defined between sets P and Q as

$$d_H(Q, P) = \max(\tilde{d}_H(P, Q), \tilde{d}_H(Q, P)), \quad (5.6)$$

where

$$\tilde{d}_H(P, Q) = \max_{x \in P} (\min_{y \in Q} ||x - y||) \quad (5.7)$$

is *directed Hausdorff distance*. It is always $d_H(\cdot, \cdot) \geq 0$, and the closer to zero, the more alike the compared sets are. It has been extensively used for image matching and pattern recognition [33].

For comparability in the two validation experiments with inclination-dependent interface energy, it is essential that the two curves $\mathbf{w}, \mathbf{w}_{PF}$ are co-centric and scaled to unit radius.

Note that the data set [40] includes also MATLAB functions for the contour shape matching.

5.3.3 Quantifying match in shrinkage rate

The shrinkage rate was obtained as mean value of shrinkage rates in simulation time interval where the area of the shape was in between 0.95-0.6 fraction of the initial area. This choice should prevent the diffuse interface from being too large compared to the shape itself, in which case it would affect the kinetics. Additionally, this approach turned out to be rather insensitive to the particular numeric settings, which is convenient for validations.

The results are presented as relative error δx , defined in the following convention

$$\delta x = 100 \frac{x_0 - x}{x} \%, \quad (5.8)$$

where x_0 is the measured value and x is the expected one. In this convention, the shrinkage was *slower* than expected when $\delta x < 0$, and *faster* when $\delta x > 0$.

5.3.4 Wulff shape

Shrinking Wulff shapes with different strengths of anisotropy were simulated. The match to the analytic shape was measured in Hausdorff distance. The shrinkage rate was expressed analytically and used for validation as well.

The Neumann boundary conditions were applied to all boundaries in a system with initial condition like in Figure 5.2a. The initial condition in every simulation was the analytic Wulff shape of the corresponding strength of anisotropy Ω as discretized by the grid. The radius was taken such that the initial shape occupied the area fraction in the domain of at least 0.25. Because the initial Wulff shape already minimized the interface energy, the shrinkage with constant

rate as in (5.4) was expected and any change in the shape was a departure from the analytic solution.

5.3.5 Kinetically compensated anisotropic circle shrinkage

This simulation experiment validates the inclination-dependence of the kinetic coefficient in combination with inclination-dependent interface energy. Specifically, the anisotropy of kinetic coefficient was chosen such that it compensated the anisotropic driving force so that the resulting interface motion was isotropic.

Again, the match to the steady-state shape (a circle) was quantified by Hausdorff distance and the mean shrinkage rate was measured when the shape area was a fraction 0.95-0.6 relative to the initial condition. Parametric study in Ω were carried out to validate the model.

The initial condition for the simulation experiment was as in Figure 5.2b, i.e. a two-phase-field system of a circular grain in a matrix.

Normal velocity v_n of a curvature-driven interface with inclination-dependent interface energy is [1]

$$v_n(\theta) = \frac{\mu}{\varrho} \sigma_0 [h(\theta) + h''(\theta)], \quad (5.9)$$

where μ is interface mobility, ϱ is local radius of curvature and $\sigma_0[h(\theta) + h''(\theta)]$ is the interface stiffness. With $h(\theta) = 1 + \delta \cos(n\theta)$ the inclination-dependent factor in (5.9) is $[h(\theta) + h''(\theta)] = 1 - \delta(n^2 - 1) \cos(n\theta) = 1 - \Omega \cos(n\theta)$.

When the interface mobility is set anisotropic as

$$\mu(\theta) = \frac{\mu_0}{1 - \Omega \cos(n\theta)}, \quad (5.10)$$

the resulting interface normal velocity v_n does not depend on interface inclination θ anymore, i.e. it is isotropic. The shrinkage rate is then (5.5).

The below presented simulations were all carried out with $\Omega < 1$, because the kinetic coefficient as in equation (5.10) is then positive for all interface inclinations.

The ratio of maximal to minimal interface velocity due to the anisotropic interface energy is $(1 + \Omega)/(1 - \Omega)$, which indicates rather strong kinetic anisotropy when Ω is close to 1. E.g. with $\Omega = 0.9$ the ratio of maximal to minimal interface velocity is 19 (assuming constant ϱ for all inclinations, which holds for a circle). Note that the corresponding ratio of maximal to minimal interface energy is only 1.0664 (with four-fold symmetry).

5.3.6 Triple junction angles

In this experiment triple junction angles are measured in systems with different combinations of pair-wise isotropic interface energies. This way it is validated how well the triple junction force balance is reproduced by the model.

The initial geometry was like in Figure 5.2b with periodic left and right boundaries, and Neumann boundary conditions on the top and bottom ones. The individual interfaces are isotropic but have different interface energies. The initially straight interface segments (1-2) and (1-3) with grain boundary energy σ_2 turn into circular arcs, which then move towards the center of curvature, i.e. downwards. The two grains η_2 and η_3 will shrink and in the steady state the angle α between the arcs (see Figure 5.7a) in the triple junction is described by Young's law [57] (section 3.3.3):

$$\alpha = 2\text{acos}(\sigma_1/2\sigma_2). \quad (5.11)$$

The ratio σ_1/σ_2 was varied in the parametric study to validate the model (see Table 5.2). It was always $\sigma_1 = 0.3 \text{ J/m}^2$ and σ_2 was computed from the ratio.

The phase field contours of interfaces (1-2) and (1-3) were analyzed by two methods in order to determine the triple junction angle α . First, the points on both the arcs nearest to the triple junction were fitted by a straight line (indicated by red segments in Figure 5.7a) and second, the remaining arc points were fitted by a circular arc (see green segments in Figure 5.7a). Simple geometric construction allows to determine the angle α from the fitted parameters in the latter case [51] as

$$\alpha = 2\text{acos}(x/R), \quad (5.12)$$

where R is the fitted circle arc radius and x is the horizontal distance from the triple junction (see the scheme in Figure 5.7a). Width of the interval in which the arcs were fitted by straight lines (width of pink rectangles in Figure 5.7a) was set to width of the interface (2-3) (i.e. half of the width on each side).

Accuracy of the lines fitting is affected especially by the width of the above interval and that of the circle arc fitting is mostly affected by the simulated arc shape.

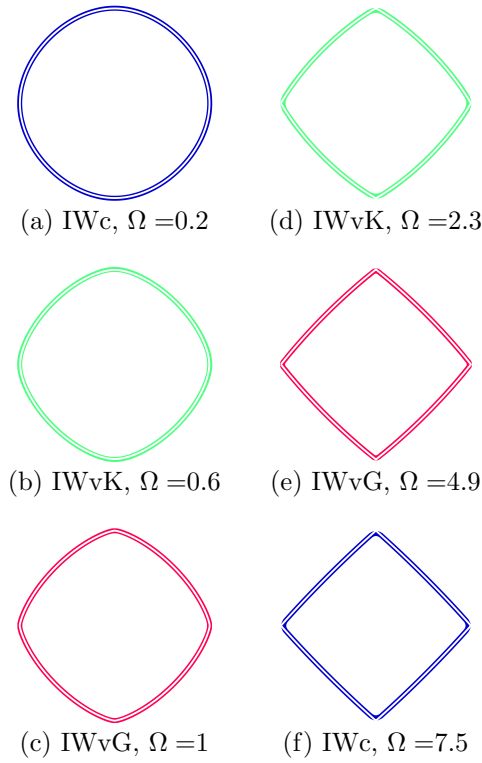


Figure 5.3: Demonstration of the simulated Wulff shapes for strengths of anisotropy Ω with the different models (base run). The white line is the analytic Wulff shape and the colored ones are the extracted phase field contours.

5.4 Results

5.4.1 Wulff shapes

The Figures 5.3a-5.3f visually compare the Wulff shapes obtained from simulation by the different models (in base run) to the analytic ones. As can be seen, the overall match is very good in all the three models, although a rather round contour near the corners in strong-anisotropy Wulff shapes are observed (this is more apparent in Figure 5.4b, which shows detail of the contours near a corner for $\Omega = 7.5$). That was expected, as no special finite difference scheme was used near corners (in [17] a one-sided finite difference scheme was proposed to avoid

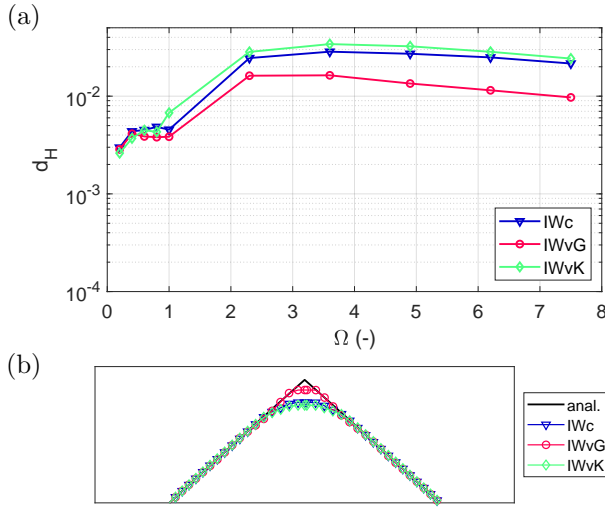


Figure 5.4: In (a) the match to Wulff shape for the model modifications in the base run as function of normalized strength of anisotropy Ω . In (b) a detail of the phase field contours near the Wulff shape corner for simulation with $\Omega = 7.5$.

corners rounding).

Figure 5.4a, shows the match to Wulff shape as function of normalized strength of anisotropy Ω in the base run. As can be seen, the IWvG model slightly outperformed the other two in strong anisotropies because it was able to resolve the corners the best (see Figure 5.4b). However, when the interface width was halved in the IW/2 run, all the models performed nearly equally well because with smaller interface width the rounding near the corners was reduced. Interestingly, the IWvG model performed comparably in the IW/2 and base runs, which is in contrast to IWc and IWvK, which improved markedly with narrower interface width.

The best results in match to Wulff shape were obtained in the 14IWpts run with IWvG model. IWc and IWvK models performed comparably in the 14IWpts and IW/2 runs.

The mean shrinkage rates of the Wulff shapes as function of strength of anisotropy are in Figure 5.5a for the base run. At first sight, all the models perform comparably well, following the analytical prediction within an absolute error of 3 %. The Figures 5.5b and 5.5c show the time evolution of shrinkage rate with $\Omega = 7.5$ in the base and IW/2 runs, respectively. It can be seen that

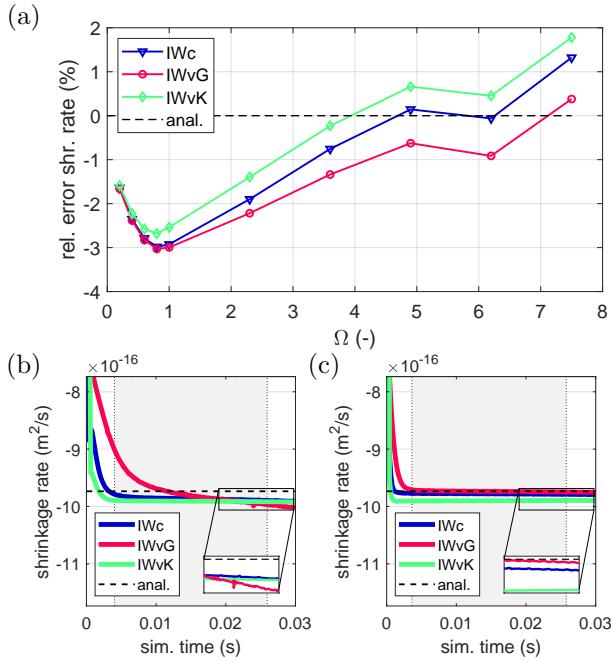


Figure 5.5: Wulff shape shrinkage rate results. In (a) the mean shrinkage rate in the base run as function of normalized strength of anisotropy Ω , in (b) and (c) there is time evolution of shrinkage rate for $\Omega = 7.5$ in the base and IW/2 runs, respectively. The shaded areas in b) and c) indicate the time interval from which the mean shrinkage rate was computed.

despite the mean shrinkage rates being near the prediction, in the base run, the shrinkage rate of IWvG model did not converge to the analytic prediction (see the inset of Figure 5.5b, where the IWvG curve clearly declines). In the IW/2 run the IWvG model did converge close to the analytic shrinkage rate (see also the inset of Figure 5.5c) and all the mean values are a little closer than in the base run. Note that in the IWvG model the lowest-energy interface has the widest interface width and that the cornered Wulff shape contains only interface orientations with lower energy. For this reason it required narrower interface width to reach constant shrinkage rate.

The relative error in mean shrinkage rate obtained with this methodology was nearly the same in the base and IW/2 runs though (both within $\pm 3\%$). Apparently, the difference is that with narrower interface the attained shrinkage rate is more steady. Additional run with even finer grid was carried out and no

improvement in the mean values of shrinkage rates was observed. It can thus be concluded that the methodology is robust enough to assess the shrinkage rate even in the domain 100x100 (i.e. base run).

In addition to the four simulation runs discussed so far, the Wulff shapes simulations were re-run also with 4 and 5 points in the interface. The match to Wulff shape was worse than with 7 or 14 points, but the shapes were resolved qualitatively well regardless. The shrinkage rates were smaller than expected though, due to grid pinning. Seven points in the interface were thus confirmed as a reasonable value for the validations and practical simulations.

No significant effect of interface width scaling in the run 1000IW was found.

5.4.2 Kinetically compensated anisotropic circle shrinkage

The quantified match to the circle and the mean shrinkage rate as functions of strength of anisotropy Ω are in Figures 5.6a and 5.6b, respectively (results of the base run showed). All models and runs retained the initial circle well or up to excellent geometrical match. Nevertheless, the IWvG model gave the best results, except for the strongest anisotropy, where the IWvK model was better. Only minor improvement in the match was achieved in the IW/2 run when compared to the base run. As with Wulff shapes simulations, the best match was obtained in the 14IWpts run, which also exhibited the best mean shrinkage rates (for all the three models).

The relative error in shrinkage rates in Figure 5.6b shows slightly decreasing trend with Ω for IWc and IWvG models (i.e. slowing down). The values of IWvK model were not affected and were constant. Apparently, the symmetric profiles of IWvK model provide an advantage for preserving the expected kinetics in simulations with strong kinetic anisotropy.

Time evolution of shrinkage rate for the strongest considered anisotropy (i.e. $\Omega = 0.9$) in Figures 5.6c and 5.6d (base and 14IWpts runs, respectively), shows that in both runs the lines slightly diverge (this being applicable to all Ω s). The convergence was better in IW/2 run, but the mean shrinkage rates were worse than in the 14IWpts run.

Apparently, optimal results would be obtained here with more points than 7 in the interface and with smaller interface-width-to-circle ratio than in the base run and 14IWpts runs. However, as noted earlier, the kinetic anisotropy is very strong in the case of $\Omega = 0.9$. For weaker anisotropy the discussed effects are less pronounced and there is little difference in the shrinkage rates among the models.

There was no significant difference between the results of base and 1000IW runs.

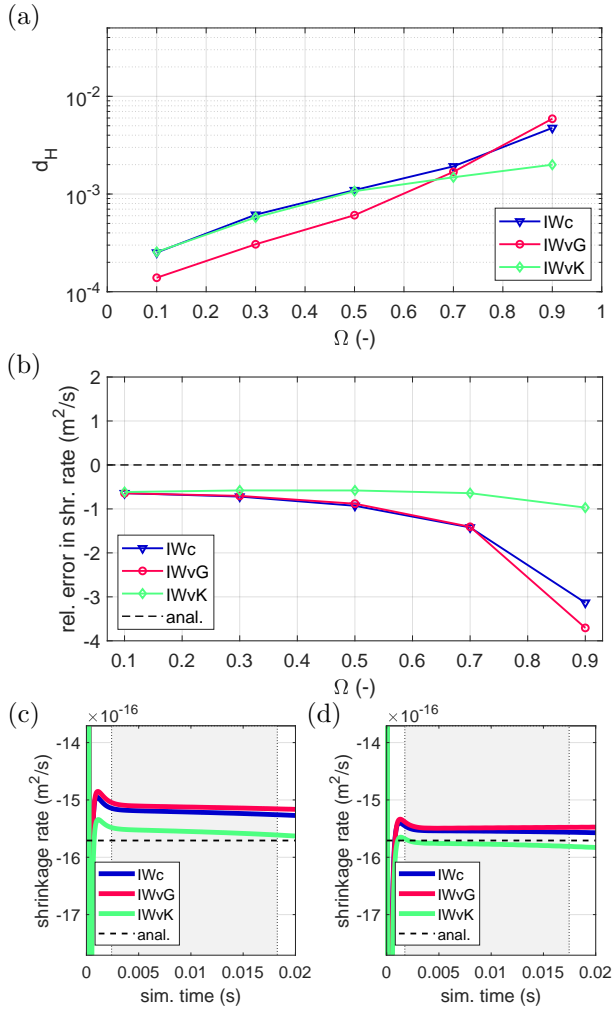


Figure 5.6: Results for kinetically compensated anisotropic shrinkage. In (a) the match to circle for the base run, in (b) the mean shrinkage rate for 14IWpts run, in (c) and (d) the shrinkage rate time evolution in simulation with $\Omega = 0.9$ in the base run and 14IWpts runs, respectively.

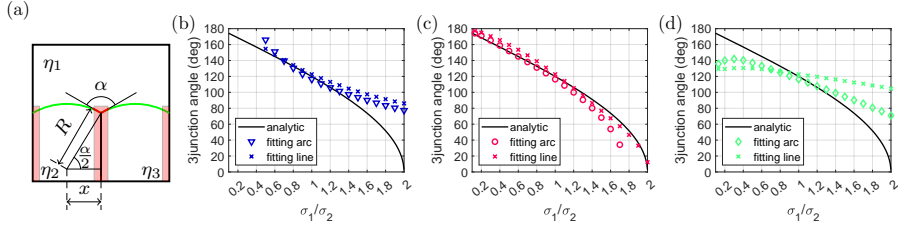


Figure 5.7: Triple junction angles. In a) the two methods for angles determination are illustrated (points fitted by straight lines in red and those fitted by circular arc in green). Subfigures b)-d) show the simulation results for different models, these being: in b) IWc, in c) IWvG and in d) IWvK. The hollow symbols correspond to the the angles determined by arc fitting and crosses to the lines fitting.

5.4.3 Equilibrium triple junction angles

Figures 5.7b-5.7d show the simulation results from the triple junction simulations as function of σ_1/σ_2 . Neither of IWc or IWvK models show good agreement to Young's law when deviating farther from an isotropic system (which has ratio $\sigma_1/\sigma_2 = 1$). The model IWvG, on the other hand, always shows very good agreement in at least one of the fitting methods along the whole range of probed ratios of interface energies. With σ_1/σ_2 closer to 2 in IWvG modification, the grains shape was slightly elongated in the vertical direction, resulting in too small radius of the fitted arcs to cross in the triple junction. The angles could not be determined this way then and the linear fit is more reliable.

For the ratios approximately $\sigma_1/\sigma_2 \leq 0.45$ the IWc model behaves non-physically. The triple junction was observed to move in the opposite than expected direction (i.e. upwards, as if the triple junction angle was larger then 180°). The overall shape of contours was not as in Figure 5.7a because the green arcs curved in the other way. In IWvK this behavior was not observed, but the Young's law is not followed. Qualitative explanation is that the IWc and IWvK models are not fully variational.

No significant change was observed in the results of the triple junction angles in runs IW/2, 14IWpts or 1000IW when compared to the base run. Quality of the results is thus not improved when more points in the interface than 7 are used. Also it implies, that the model behavior (for all parameters assignment strategies) is not affected by reducing the interface-width-to-feature ratio or the interface width scaling. The latter confirms that the model is quantitative.

5.5 Conclusions

This chapter presented a quantitative methodology for assessment of the anisotropic curvature driving force in phase field method. It was demonstrated in comparison of three different modifications of a multi-phase field model. The match to the expected shape and the shrinkage rate were quantified in two different benchmark problems. The methodology was sensitive enough to capture differences between the model modifications and is suitable for validation and benchmarking of different models and numerical solvers.

The overall performance of the three model modifications in the benchmarks was comparable. Both match to the steady-state shapes and the shrinkage rates followed the expected results as in the anisotropic mean curvature flow. However, a significant difference was noted in a supplementary benchmark simulation where triple junction angles were measured. It was observed that only the IWvG model modification (with only the parameter γ anisotropic) reproduced the triple junction angles in the full interval 0.13-2 of σ_1/σ_2 , whereas IWc and IWvK modifications failed for ratios farther from 1. It is noted that these two modifications were not fully variational in order to avoid ghost phases, whereas IWvG is fully variational and yet the ghost phases do not appear.

Even though the triple junction benchmark did not involve interfaces with inclination-dependent interface energies, one conclusion can be made about that case regardless. As the IWc and IWvK were shown unreliable in the simpler pair-wise isotropic case, there is no reason why they should be reliable in the more complicated one. Further development and validations should thus focus on the IWvG model modification.

No results were significantly affected by the interface width scaling. Also, it was confirmed that 7 points in the interface were sufficient for retaining the expected kinetics in most cases, unless the inclination dependence of the kinetic coefficient was very strong.

The results in this chapter are reproducible with codes provided in the data set [40].

Chapter 6

Nucleation probability assessment - a phase field methodology

6.1 Introduction

This chapter develops a methodology to obtain insight about the nucleation barrier from the stable shapes of particles on a planar support in 2D. The developed multi-phase phase field model is used to obtain the interface-energy-minimizing shapes and the below described domain scaling is then used to find shape factor of the shape.

The used model represents wetting of a plane by a crystal and combines the features developed by the author: volume conservation using the fictitious concentration field approach and the general Neumann boundary conditions to control the interface inclination at the domain boundary.

The method to obtain the shape factors utilizes that the interface in phase field method is implicitly tracked, i.e. it evolves without any assumption on its position. Additionally, it makes use of the fact, that in the simulated geometry, the total energy of the system is in fact the total particle-liquid interface energy. Advantage of the method is that it does not a-priori assume any shape, it is thus in principle usable for non-analytic cases, where the solution is not known, e.g. a particle on a grain boundary.

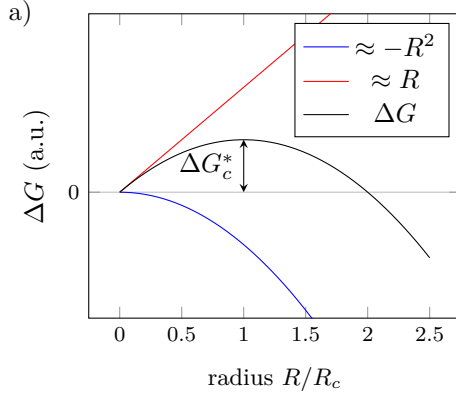


Figure 6.1: Schematic dependence of the total energy change on the radius of the inserted nucleus in 2D.

6.2 Some fundamentals

In 2D, the Gibbs free energy difference upon a nucleus insertion in the system is due to competition between area and line energy contributions (see also Figure 6.1). Be A_{hom} the nucleus area and its interface be described by a parametric curve \mathcal{C} . In the isotropic case, \mathcal{C} is a circle and the interfacial contribution is simply σL , where $L = 2\pi R$ is the interface length and σ the isotropic specific interface energy. The Gibbs free energy difference of a free nucleus is then (with ΔG_A being supersaturation)

$$\Delta G_{hom} = -\Delta G_A A_{hom} + \sigma L \quad (6.1)$$

$$= (-\Delta G_A R^2 + 2R\sigma)\pi, \quad (6.2)$$

which implies the critical radius

$$R_c = \frac{\sigma}{\Delta G_A} \quad (6.3)$$

and critical nucleation barrier

$$(\Delta G_c^*)_{hom} = \hat{A}_{hom} \frac{\sigma^2}{\Delta G_A}, \quad (6.4)$$

where the non-dimensional nucleus area is $\hat{A}_{hom} = A_{hom}/R^2 = \pi$.

In heterogeneous nucleation, the shape factor $S(\theta) = A_{het}/A_{hom}$ scales the homogeneous total energy change upon nucleus insertion ΔG_{hom} as

$$\Delta G_{het} = S(\theta) \Delta G_{hom}, \quad (6.5)$$

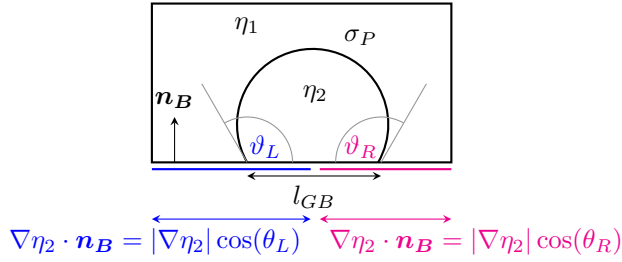


Figure 6.2: Sketch of the geometry in the phase-field simulations used in the domain scaling methodology for nucleation barrier assessment. The symbols ϑ_L, ϑ_R denote tangent angles in the contact points and θ_L, θ_R the normal ones. The intervals on the bottom domain boundary with the different interface inclination imposed are indicated (note that η_1 has analogous boundary conditions which must be consistent). l_{GB} is the length of the grain boundary interval between the contact points. σ_P is the particle-liquid interface energy.

which for the heterogeneous nucleation barrier implies

$$(\Delta G_c^*)_{het} = S(\theta)(\Delta G_c^*)_{hom}. \quad (6.6)$$

The nucleus radius is equal in both homogeneous and heterogeneous nucleation.

6.3 Methodology

The simulated system geometry is sketched in Figure 6.2. A two-phase system of a particle in a liquid was described by two phase field variables in Moelans' model, one representing the liquid parent phase (η_1) and the second (η_2) representing the particle (possibly with anisotropic interface energy). The bottom domain boundary then represents the substrate and the interface inclination ϑ_L, ϑ_R in the two contact points is controlled by the boundary condition as indicated in the figure.

Volume conservation was assured using the fictitious concentration field.

The particle-liquid interface energy σ_P was assumed, together with the contact angles ϑ_L, ϑ_R .

The domain scaling methodology is in fact a post-processing of the result of phase field simulation. By the result, it is meant the phase fields corresponding to the liquid and to the particle within the simulation grid. Then, the grid spacing is scaled and the model parameters are re-computed accordingly. The

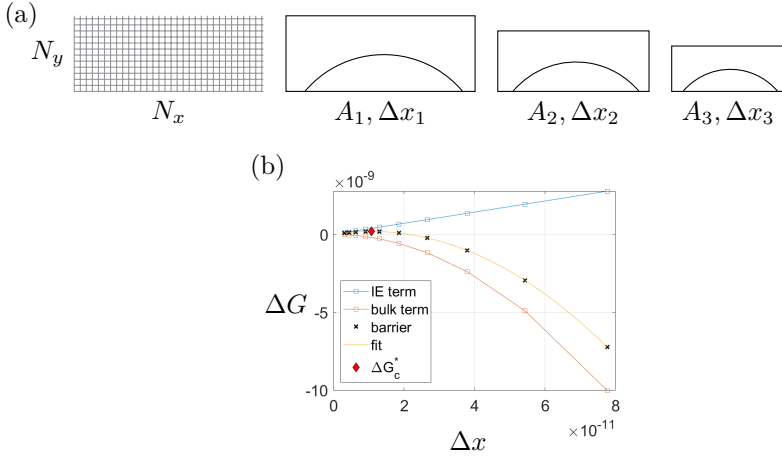


Figure 6.3: Nucleation barrier determination using domain scaling. In (a) sketch of domain scaling. The area fraction of the particle is preserved, as well as the number of grid points N_x, N_y . A_i are scaled areas of the domain and Δx_i is the i -th scaled grid spacing in meters. In (b) the energy contributions were plotted for each Δx_i , the barrier being denoted by black crosses and the critical nucleation barrier determined by fitting of parabolic function is indicated by red diamond.

particle area fraction $\xi = A_P/A_D$ in the scaled system remains the same, but its area A_P and perimeter are scaled accordingly. Using the (unchanged) phase fields and re-computed parameters, the total interface energy is re-evaluated by the free energy functional for the new scale. The domain scaling is sketched in Figure 6.3a.

Note that the free energy functional only accounts for the solid-liquid interface energy, but in the total energy change, there must be included also the term representing the replacement of the former planar substrate-liquid interface with specific energy σ_S by the grain boundary: $l_{GB}(\sigma_{GB} - \sigma_S)$. Because the Young's equation for triple junctions of isotropic interfaces reads

$$\sigma_S = \sigma_{GB} + \sigma_P \cos(\vartheta), \quad (6.7)$$

the grain-boundary-energy term can be thus re-written as $-l_{GB}\sigma_P \cos(\vartheta)$, which allows us to disregard the values of the substrate and grain boundary energy. In the phase field simulation, the distance between the contact points is interpreted as l_{GB} (see Figure 6.2) and the above term is added to the total interface energy change upon the nucleus insertion ΔG_σ , hence when denoting the free energy

functional as $F(\eta, \nabla\eta)$ it can be written

$$\Delta G_\sigma = F(\eta, \nabla\eta) - l_{GB}\sigma_P \cos(\vartheta). \quad (6.8)$$

Note that l_{GB} must be scaled as well.

The above procedure provided the total interface energy change upon the particle insertion as function of the length scale (Δx_i in Figure 6.3a). Even though it is not the particle radius as in (6.2), the same physical dimension (length) of the grid spacing assures that the order of the polynomial $\Delta G(\Delta x) = a(\Delta x) - b(\Delta x)^2$ is the same as in (6.2).

When the driving force ΔG_A is explicitly assumed, the bulk energy contribution can be computed using each of the absolute values of the scaled particle area A_P . Because the interface energy contribution was already computed for each scaled system, it is possible to subtract the two to obtain the total energy change in insertion of those particles, as is shown in Figure 6.3b. For illustration, multiple scaling steps were taken here, but with the simple parabolic dependence of ΔG in 2D, only 3 points would suffice to unambiguously determine its parameters. Finding the position of the maximum is then trivial.

The maximum parabola value is the critical nucleation barrier ΔG_c^* for the investigated equilibrium shape. However, more practical quantity is the corresponding shape factor S , which can be then obtained from equations (6.4) and (6.6) as

$$S = (\Delta G_c^*)_{hom} \frac{\Delta G_A}{\hat{A}_{hom}\sigma_0^2}. \quad (6.9)$$

Note, that one needs to know the non-dimensional area of the isolated equilibrium shape \hat{A}_{hom} .

Recall, that the contact angles of the particle with the substrate were the input to the phase field simulation, hence the obtained shape factor S is a function of the particular assumed conditions.

The domain scaling procedure does not depend on whether the interface energy was isotropic or anisotropic, because the used formulas are equal in the two cases [36]. Only in the case with inclination-dependent interface energy more steps are required in evaluation of the free energy functional $F(\eta, \nabla\eta)$.

6.4 Numerical implementation

The simulations were carried out using the same MATLAB programme, which was used in the previous chapter 5, hence only some extra considerations are commented here.

Table 6.1: Parameters in the phase field simulation (unless stated otherwise). The parameters in the top part correspond to the Moelans' model, in the bottom one to the diffusion equation used in the fictitious concentration field approach to conserve volume of the simulated particle. The not mentioned parameters m, κ, L in Moelans' model can be determined using the dedicated published MATLAB functions [40].

symbol	parameter	units	values
l_{IW}	interface width	m	1×10^{-9}
σ_P	particle-liquid isotropic interface energy	J/m ²	1
Δx	grid spacing	m	$l_{IW}/7$
C	Courant number	-	0.18
μ_P	particle-liquid interface mobility	m ⁴ /Js	7.5×10^{-16}
Δt	time step	s	using (5.1)
A	steepness of parabolas	J/m ³	3.1623×10^{-11}
D	diffusion coefficient	m ² /s	$0.3\Delta x^2/\Delta t$
$c_{L,eq}$	equilibrium molar fraction in liquid	-	0.02
$c_{S,eq}$	equilibrium molar fraction in solid	-	0.98
M	diffusion coefficient in C-H equation	m ⁵ /Js	$M = D/A$

The Appendix D contains the necessary modifications to the finite-difference algorithm when implementing the general Neumann boundary conditions. Eventually, the changes affected all the finite difference operators (standing in place of unidirectional or mixed derivatives and laplacian), but only in the parts of the matrices, which interact with the domain boundary.

The parameters of the phase field simulations needed to reproduce the results are in Table 6.1. Regarding the volume conservation, it was validated that with the listed parameters, the area of the conserved field would change no more than about 1 % from its initial value in practical simulations, which is sufficient for the equilibrium shape simulations and subsequent barrier determination.

The re-computation of the model parameters during the domain scaling was carried out using the same MATLAB functions [40] as used in chapter 5 and [42].

6.5 Validations

6.5.1 Tilted straight line

The implementation of general Neumann boundary conditions controlling the inclination angle at the domain boundary was validated in simulations sketched

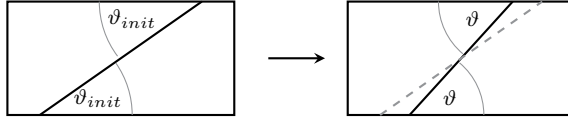


Figure 6.4: Validation of the general NBC for control of the inclination angle at the boundary - tilted line simulations (isotropic interface energy). In the simulations with inclination-dependent interface energy there was $\vartheta_{init} = \vartheta$

in Figure 6.4. Note that the volume was not conserved in these simulations. A slightly different approach had to be taken in the case with isotropic and anisotropic interface energy, as described below.

In the case with isotropic interface energy, the initial condition for the simulation was a tilted line, which was inclined under different angle ϑ_{init} than the imposed inclination angle ϑ . The simulation ran until the total energy converged (i.e. until the change in energy per time step was smaller than a threshold). The final state was expected to be a line aligned under the target angle ϑ . From linear fit of the final phase field contour, the resulting inclination angle was read out. A range of angles between 15° - 165° was probed, and the results were plotted in Figure 6.5a. As can be seen, a perfect match was achieved.

When validating the same with inclination-dependent interface energy, the methodology had to be modified slightly: the straight line was placed in its imposed position already in the initial condition, i.e. $\vartheta_{init} = \vartheta$. That was because once any curvature appeared in the straight line (which happened when the interface was forced to move by the boundary conditions), it began deforming and there remained no straight line. To assure that the tilted line be the equilibrium state of the system, the anisotropy function was always rotated so that the target inclination angle ϑ corresponded to the minimal interface energy. Only then the straight line could be immobile and the general Neumann BC could be validated in the same way like with the isotropic interface energy, i.e. simulation until energy convergence and linear fit of the contour. The target angle was observed very accurately in this case as well, as can be seen in Figure 6.5b.

6.6 Results

First, the methodology is used to determine the shape factor in isotropic heterogeneous nucleation as a proof-of-concept application.

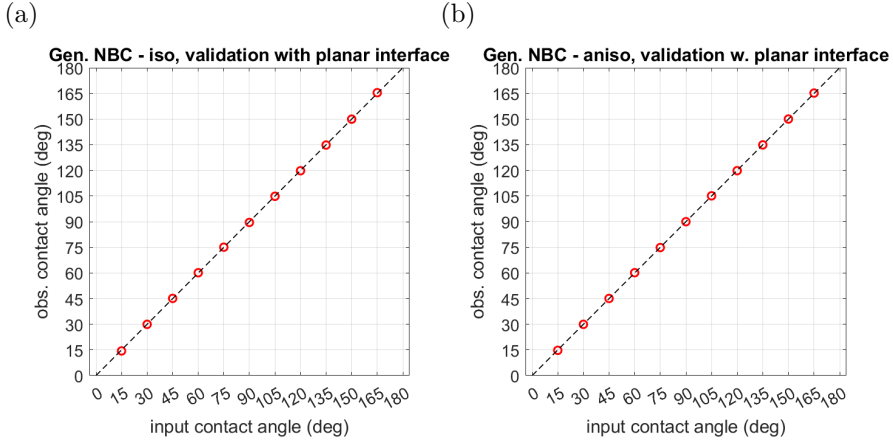


Figure 6.5: Results of tilted plane validation. In a) the result with isotropic interface, in b) with anisotropic one.

6.6.1 Particle on a plane (isotropic interface energy)

In heterogeneous nucleation with isotropic interface energy in 2D, the equilibrium shape is a circular segment and the shape factor as function of the tangent contact angle (wetting angle) ϑ (see Figure 6.2) is

$$S(\vartheta) = \frac{2\vartheta - \sin(2\vartheta)}{2\pi}. \quad (6.10)$$

A series of phase field simulations was run in the geometry as in Figure 6.2 with $\vartheta_L = \vartheta_R$ to assess the above dependence of shape factor on the wetting angle. See Table 6.2 for details on the simulation grid in the respective simulations. It is assumed, that the obtained shape is the equilibrium one, which is assured by conditional stopping of the simulation, when the total interface energy converged (i.e. its change in the new time step is below threshold).

The contact angles were the same as in the tilted plane validation, i.e. from $\vartheta = 15^\circ$ to $\vartheta = 165^\circ$ with a 15° step. The initial condition corresponded to the target circle segments to reduce the computation time. Using the equation (6.9) and taking into account that the non-dimensional area for a circle is $\hat{A}_{circle} = \pi$, the results in Figure 6.6 were obtained.

Firstly, it is interesting that the observed contact angles ϑ_{obs} differed from those imposed by the boundary conditions ϑ significantly more than in the tilted line validation. This can be seen in the Figure 6.6a, where the difference $\vartheta_{obs} - \vartheta$ was plotted. The angle difference was larger than 5° for 3 rather

Table 6.2: Simulation grid dimensions in individual simulations of a particle with isotropic interface energy on a plane in 2D. The grid aspect ratio was determined based on the expected shape aspect ratio.

ϑ	$N_x \times N_y$
15	546×42
30	382×51
45	308×64
60	261×75
75	226×87
90	198×99
105	176×111
120	162×121
135	152×129
150	145×135
165	141×139

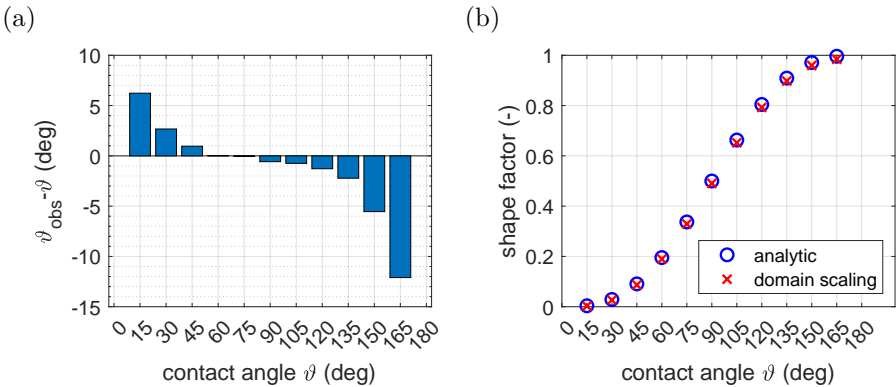


Figure 6.6: Results of the phase field simulation for determination of shape factor in heterogeneous nucleation with isotropic interface energy. In (a) the error in observed contact angles at the end of the simulation, in (b) the shape factor as obtained by domain scaling method.

inclined angles (i.e. near 0° or 180°). The deviation $\vartheta_{obs} - \vartheta$ did not depend on the phase field interface parameterization. In the base run, the interface width was $l_{IW} = 1 \times 10^{-9}$ m, with 7 points through the interface. The compared simulations probed the effect of a) increasing the domain area, while keeping the l_{IW} equal (effectively narrowing the physical interface width relative to the simulation initial condition) and of adding points to the interface (both actions refined the grid below the simulated initial condition) and both might improve phase field simulation accuracy in different regards. That did not happen in terms of the contact angles, though.

However, the shape factor determination was not affected heavily, because it turned out that there actually were very few points deviating from the expected circular shape and those were near the boundary. This is confirmed also by the obtained values of shape factor, which follow closely the analytic prediction. The different interface parametrization yielded slight improvement in the shape factor values, but not relevant in the current application.

6.6.2 Particle on a grain boundary (isotropic interface energy)

The present section investigates the theoretical case when the nucleus extends over the grain boundary and thus its wetting condition is unequal on the two sides.

The geometry of the problem is sketched in Figure 6.7. When the two sides are wetted differently, it implies different contact angles and thus radii of the equilibrium shapes. That necessarily implies also different curvatures $K_{L/R}$. The chemical potential μ (the driving force, see (2.1))

$$\mu = \sigma K, \quad (6.11)$$

over the whole stable shape must be a constant in order to have it in equilibrium. But for a constant σ that cannot be achieved.

Nevertheless, it is known that nucleation may happen on top of grain boundaries. Additionally, the nuclei in classical nucleation theory do not necessarily have the interface-energy minimizing shape, even though that one is the most likely. Hence, even if the shape is not in equilibrium, we assume that it could nucleate. Supposedly, it could survive by sliding to the lower-energy side of the grain boundary. Using the domain scaling procedure, the shape factor of the unknown compound shape can be quantified.

To reduce the simulation time, the initial condition was a shape combined from parts of the equilibrium shapes from both sides, connected by a tangent line to prevent dents in the initial shape (the initial condition was very similar to the

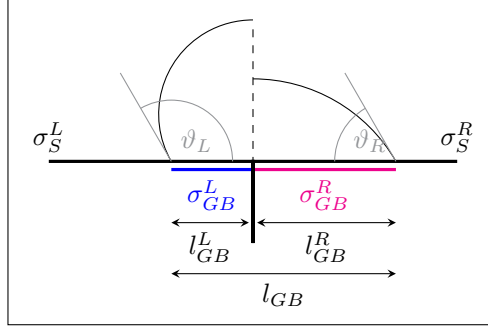


Figure 6.7: A particle on a grain boundary. The specific interface energies $\sigma_S^{L/R}$ belong to the substrate-solution interfaces and $\sigma_{GB}^{L/R}$ to the respective grain boundaries. The grain boundary lengths $l_{GB}^{L/R}$ and l_{GB} are indicated.

problem sketch in Figure 6.7, only with the tangent line). The initial condition can be seen in Figure 6.8, it is the one with steps (due to discretization in the simulation grid).

In the computation of the total grain boundary energy (meaning the substrate-particle interface), there will be two contributions now, $\sigma_{GB}^L = \sigma_S^L - \sigma_P \cos(\vartheta_L)$ and $\sigma_{GB}^R = \sigma_S^R - \sigma_P \cos(\vartheta_R)$. It turns out, that it is sufficient to assume only $\sigma_P, \vartheta_L, \vartheta_R$, because in the total free energy the above Young's equation can be applied as follows

$$\Delta G_\sigma = F(\eta, \nabla \eta) + l_L(\sigma_{GB}^L - \sigma_S^L) + l_R(\sigma_{GB}^R - \sigma_S^R) \quad (6.12)$$

$$= F(\eta, \nabla \eta) - \sigma_P[l_L \cos(\vartheta_L) - l_R \cos(\vartheta_R)]. \quad (6.13)$$

Depending on where exactly the grain boundary (between the grains in the substrate) is placed below the particle, the individual segments will have different length, i.e. it is not clear how to divide l_{GB} into the left and right segments l_L, l_R .

For this reason, three shape factors were determined for each single shape, which corresponded to the cases when

1. $l_L = l_{GB}, l_R = 0$, then $\Delta G_\sigma = F(\eta, \nabla \eta) - \sigma_P l_{GB} \cos(\vartheta_L)$,
2. $l_L = 0, l_R = l_{GB}$, then $\Delta G_\sigma = F(\eta, \nabla \eta) - \sigma_P l_{GB} \cos(\vartheta_R)$ and
3. $l_L = l_R = l_{GB}/2$, then $\Delta G_\sigma = F(\eta, \nabla \eta) - 0.5 \sigma_P l_{GB} [\cos(\vartheta_L) + \cos(\vartheta_R)]$

The first two are limiting cases, when the contact point is infinitesimally just behind the substrate grains grain boundary, hence the full substrate-particle grain boundary lays on the either higher- or lower-energy grain. In the last case, the substrate grain boundary is just in the middle between the contact points.

See Table !!!! for details on the simulation The contact angles ϑ_L, ϑ_R were input to the simulation. In the presented results, it was assumed that $\vartheta_L = 120^\circ$ and ϑ_R was varied between 30° - 90° .

The first observation from the simulations is that the shape evolves, but even when it stops evolving, it moves as a block towards the side which has lower grain boundary energy. For the time evolution of the phase field contours in different cases see Figure 6.8. The intuitively correct direction of motion is reproduced by the model, even though the system energy does not account for the grain boundary explicitly. The reason is that the curvature driving force acts towards the center of curvature. As can be seen in Figure 6.8, the side with greater contact angle is more curved. The flatter is the opposite side, the less is the curvature driving force balanced.

The velocity of the shape centroid in the x direction was obtained from linear fit through the x centroid coordinate in time, see Figure 6.9a. The result quantifies the above reasoning, as it can be seen that lower ϑ_R (i.e. flatter right side) were associated with faster translation to the right.

The computed shape factors of the compound shapes were plotted in Figure 6.9b with error bars indicating the possible span of values depending on the grain boundary position below the particle. The grain boundary energy contribution in the total energy of the particle seems to be a crucial factor for the nucleation probability. When the particle is sufficiently shifted to the lower-energy side, the deviation in shape may not cause dramatic increase in the nucleation barrier. In the opposite case (the particle is rather on the high-energy side), the nucleation can even be less likely than that of an isolated particle (homogeneous nucleation). In the extreme high-energy case for nearly all simulated ϑ_R , the nucleation on top of the boundary was less likely than simply nucleating only on the high-energy part of the substrate.

6.7 TODO Conclusion

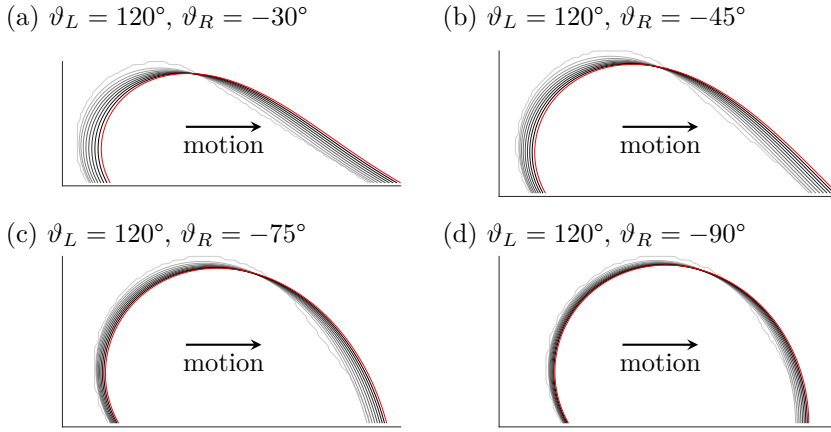


Figure 6.8: Time evolution of phase field contours in the simulation of a particle on a grain boundary. The time evolves from gray to black contours, the last contour in the simulation is red.

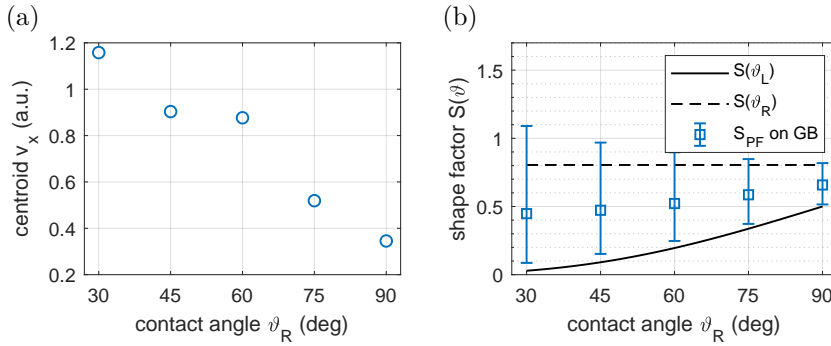


Figure 6.9: Results from the simulation of a particle on a grain boundary. In (a) the x-direction velocity of the shape centroid as function of the right contact angle ϑ_R and in (b) the shape factor corresponding to the shape at the end of the simulation (i.e. red contours from Figure 6.8).

Chapter 7

Analytic nucleation probability assessment and Monte Carlo simulations

7.1 Introduction

The method developed in this paper obtains anisotropy in nucleation barrier (and, eventually, the nucleation probability) as function of the interface energy anisotropy, bottom grain orientation and the nucleus orientation. The method is based on principles of classical nucleation theory. Then, in order to demonstrate the effect of the anisotropic barrier on the film texture, a Monte Carlo algorithm was developed and used to simulate growth and nucleation in a polycrystalline film. The aim of this paper is to qualitatively explore the implications of the anisotropic interface energy for the orientation selection during repeated nucleation in the polycrystalline growth.

The paper is organized in five main parts. Firstly, the necessary fundamentals are described in Section ?? and some theoretical novelties regarding the Winterbottom construction are introduced. In Section 7.2, the problem specification defines all parameters in the orientation-dependent Winterbottom construction to be solved and successively the shape factor-orientation maps are presented and explained. These are used as input in the Monte Carlo simulations described in Section 7.3, together with their results. The Section 7.4 applies the obtained insights to a peculiar case of texture evolution in experiment [2]

(electrodeposited nickel). There, a sudden change in texture occurred after thickness of $2\mu\text{m}$, supposedly due to nucleation. The nucleation brought in new orientations, which succeeded in the growth competition. Interestingly, the said film was deposited very slowly, hence the high nucleation rate is rather unexpected when viewed in the perspective of classical nucleation theory with isotropic interface energy. However, with the anisotropic interface energy included as worked out here, a qualitative explanation was found.

7.1.1 Terminology in heterogeneous nucleation

3D nucleation and 2D nucleation are terms used in classical nucleation theory to describe two different nucleation mechanisms on a plane in 3D space.

In 3D nucleation, the nuclei form as 3D clusters on the flat substrate and their interface energy is derived mostly from their curved surface. The possible edge and vortex energies are usually neglected. The clusters grow and coalesce.

In 2D nucleation, the nucleus is a mono-atomic step (usually assumed in a shape of a disc) on the (theoretically) atomically smooth surface. In the total nucleus interface energy, the edge energy cannot be neglected. The nuclei grow along the surface layer by layer.

These concepts can be reduced to 2D space, where the 3D nucleation is equivalent to 2D nucleation and the 2D nucleation to 1D nucleation. In order to simplify the terminology when describing the results from 2D space, the terms spatial and interfacial nucleation are introduced, which indicate the difference in the mechanism irrespective of the used dimension.

This paper only deals with the anisotropy in nucleation barriers of nuclei created in *spatial* nucleation. That is because it is not expected that the grain orientation could change during the *interfacial* nucleation, which is essentially a localized epitaxial growth. In the following, the *spatial nucleus* denotes a nucleus created in spatial nucleation.

7.1.2 Heterogeneous spatial nucleation and shape factor

Note that the formulas and their description in this section are given for 2D space, but they could easily be generalized to 3D.

Because nucleation is a thermally activated process, the probability P of finding the critical nucleus at a certain spot follows the Arrhenius relation

$$P \approx \exp\left(-\frac{\Delta G_c^*}{kT}\right), \quad (7.1)$$

where k is the Boltzmann constant, T absolute temperature and ΔG_c^* is the *critical nucleation barrier* (in J), which is to be overcome by the thermal fluctuations in order to form a critical nucleus. A nucleus with the critical area A_c is metastable. The nucleation barrier ΔG_c^* is the *nucleation work* [39] to be done in order to insert a critical nucleus. Subcritical nuclei dissolve, the supercritical ones grow.

In heterogeneous nucleation (i.e. nucleation on a wall), a shape factor $S \geq 0$ is the ratio of the heterogeneous nucleus area A_{het} to the area of the isolated particle A_{hom} (homogenous nucleus) generated at equivalent conditions. It can thus be written as a proportionality factor

$$A_{het} = S A_{hom}. \quad (7.2)$$

The force balance of the meeting interfaces determines the wetting, which decides the value of S . When $S = 0$, no spatial nucleus (here 2D nucleus) is inserted, because complete wetting occurs and only interfacial (1D) nucleation is possible.

Because it was shown in [36], that the nucleation barrier is proportional to the actual area of the nucleus, the shape factor relates the nucleation barriers too, hence

$$\Delta G_{het}^* = S \Delta G_{hom}^*. \quad (7.3)$$

The above implies, that knowing the homogeneous nucleation barrier and the shape factor for a particular heterogeneous nucleus allows to determine the heterogeneous nucleation barrier and also the relative difference in nucleation probability. This reduces the problem of heterogeneous nucleation probability to the determination of a shape factor, obtained as ratio of areas of heterogeneous and homogeneous nucleus.

It should be emphasized, that in the case of multiple possible shape solutions (like e.g. in Figure 2.2a), the Wulff shape of the first order (Figure 2.2b) was always assumed as the homogeneous nucleus in the shape factor determination. That choice was made because the nucleation barrier is proportional to the inserted nucleus area (see (7.4)), which implies that smaller nuclei have larger nucleation probability. The Wulff shape of the first order is the smallest one, hence the most likely to occur.

In 2D, the critical homogeneous nucleation barrier $(\Delta G_c^*)_{hom}$ depends on the scalar interface energy σ_0 from $\sigma(\theta) = \sigma_0 h(\theta)$ (i.e. as in (2.3)) and the bulk driving force for the phase transformation ΔG_V as

$$(\Delta G_c^*)_{hom} = \hat{A}_{hom} \frac{\sigma_0^2}{\Delta G_V}. \quad (7.4)$$

where $\hat{A}_{hom} = A_{hom}/R^2$ is a non-dimensional area of the nucleus, R being a radius of the nucleus. If the nucleus is a particle with anisotropic interface energy, then R is a generalized radius, a scalar factor scaling the area of the particle. In classical nucleation theory in 2D (with both isotropic and anisotropic interface energy [36]) it is simply

$$R = \frac{\sigma_0}{\Delta G_V} \quad (7.5)$$

In order to get a reasonable nucleation rate of $1 \text{ cm}^{-3}\text{s}^{-1}$ and larger, the homogeneous nucleation barrier ought to be $(\Delta G_c^*)_{hom} \leq 78 kT$, but at the same time it should be $(\Delta G_c^*)_{hom} \geq 10 kT$, because the nucleus radius then gets so small, that the applicability of the continuous approach of classical nucleation theory becomes questionable [57, pp.195].

Let the symbol

$$\beta = \hat{A}_{hom} \frac{\sigma_0^2}{\Delta G_V} \frac{1}{kT} \quad (7.6)$$

stand for the non-dimensional nucleation barrier, i.e. the nucleation barrier expressed in multiples of kT . Apparently, $10 \leq \beta \leq 78$, in order to observe a reasonable amount of nucleation describable by classical nucleation theory. Then, the homogeneous nucleation probability can be written as

$$P_{hom} = \omega \exp(-\beta) \quad (7.7)$$

and the heterogeneous one

$$P_{het} = \omega \exp(-\beta S). \quad (7.8)$$

The vibration frequency ω represents the number of nucleation attempts per unit of time (assumed to be a constant in this paper).

Note that β aggregates information about temperature, the driving force and the interface energy. In this paper, the temperature T and σ_0 are assumed to be constant. Consequently, when β varies, the bulk driving force ΔG_V is varied inversely, as can be seen from the equation (7.6). This way, the variations in β are also related to the deposition rate, because the higher the driving force, the higher the deposition rate.

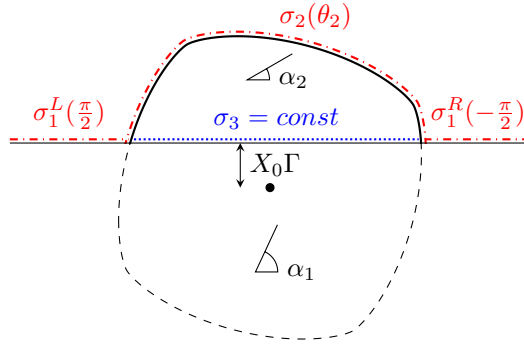


Figure 7.1: Winterbottom construction on a weak-anisotropy Wulff shape with indication of the distinct types of interfaces: red and dash-dotted line is the anisotropic solid-liquid interface and the blue and dotted line is the Read-Shockley grain boundary (independent on interface inclination).

7.2 Nucleation probability assessment

7.2.1 Problem statement

A polycrystalline film grows from a liquid parent phase. Nucleation during the film growth is expected, which then occurs on the same material, as is being deposited. In this system there are two distinct types of interfaces: the solid-liquid interface with inclination-dependent interface energy; and the grain boundary following the Read-Shockley dependence on misorientation (inclination-independent, though). Every grain has a particular crystallographic orientation (in 2D characterized by a single angle α). The grain orientation α coincides with the rotation of the solid-liquid interface energy anisotropy function (2.4).

A single nucleation event is always assumed to take place on a straight solid-liquid interface. The nucleus is assumed to take on an energy-minimizing equilibrium shape. Hence, in the case of multiple possible solutions, the one with the smallest area is selected.

A sketch of a single nucleation event is in Figure 7.1. The substrate is a plane, hence the orientation of its normal and the interface energy are equal on both sides of the particle. However, due to the problem geometry it is seen differently

in the polar coordinate systems associated with the left and right contact angle - the normal is $+\pi/2$ on the left and $-\pi/2$ on the right, hence $\sigma_1^L(\frac{\pi}{2}) = \sigma_1^R(-\frac{\pi}{2})$.

Specifically, the solid-liquid interface energy is

$$\sigma_{SL}(\theta) = \sigma_{SL}^0 h(\theta), \quad (7.9)$$

where $h(\theta)$ is the anisotropy function (2.4). The Read-Shockley grain boundary energy dependence is a function of disorientation $\Delta\alpha(\alpha_1, \alpha_2)$

$$\sigma_{GB}(\alpha_1, \alpha_2) = \begin{cases} \sigma_{GB}^0 \frac{\Delta\alpha(\alpha_1, \alpha_2)}{\Delta_{lim}} \ln\left(\frac{\Delta\alpha(\alpha_1, \alpha_2)}{\Delta_{lim}}\right) & \Delta\alpha \leq \Delta_{lim} \\ \sigma_{GB}^0 & \Delta\alpha > \Delta_{lim} \end{cases}, \quad (7.10)$$

with $\Delta_{lim} = 15^\circ$ used here. Note that due to the problem symmetry of order n , the Read-Shockley dependence must be periodic too, hence the common disorientation definition $\Delta\alpha = |\alpha_1 - \alpha_2|$ cannot be used. The periodicity can be achieved using *modulo with rounded division convention* [71]

$$\Delta\alpha(\alpha_1, \alpha_2) = \text{mod}(\alpha_1 - \alpha_2, 2\pi/n), \quad (7.11)$$

where $\text{mod}(x, y) = x - \text{ground}(x/y)$. This way, the disorientation is always within $-\pi/n \leq \Delta\alpha \leq \pi/n$ and the minimum of Read-Shockley appears at $k\pi/n$, where $k = -1, 0, 1$.

The bottom grain orientation is α_1 and the nucleus orientation is α_2 . The respective interface energies are expressed as

$$\sigma_1^L(\frac{\pi}{2}) = \sigma_1^R(-\frac{\pi}{2}) = \sigma_{SL}^0 h(\frac{\pi}{2} - \alpha_1) \quad (7.12)$$

$$\sigma_2(\theta_2) = \sigma_{SL}^0 h(\theta_2 - \alpha_2) \quad (7.13)$$

$$\sigma_3 = \sigma_{GB}(\alpha_1, \alpha_2). \quad (7.14)$$

Then, the wetting parameter Γ can be expressed as a function of the bottom grain and nucleus orientations

$$\Gamma(\alpha_1, \alpha_2) = \frac{\sigma_1^L(\frac{\pi}{2}) - \sigma_3(\alpha_1, \alpha_2)}{\sigma_{SL}^0} \quad (7.15)$$

$$= h(\frac{\pi}{2} - \alpha_1) - \frac{\sigma_{GB}(\alpha_1, \alpha_2)}{\sigma_{SL}^0}. \quad (7.16)$$

It was assumed that $\sigma_{GB}^0 = \sigma_{SL}^0 = 0.3 \text{ J/m}^2$.

With all above, the geometric problem is fully specified by the pair of orientations (α_1, α_2) , both of which are from the interval $0 \leq \alpha < 2\pi/n$. The top grain orientation α_2 specifies the rotation of the equilibrium shape and the wetting parameter (7.16) specifies where the truncating line passes.

7.2.2 Stability as function of the bottom grain orientation

If the stability conditions (2.12) and (2.14) do not hold for either of the two contact angles, the shape is not stable. The condition (2.12) is fulfilled by default in the (generalized) Winterbottom construction. The condition (2.14) is simplified by the assumption of the grain boundary being inclination independent, because then $\tilde{\sigma}_3 = \sigma_3$. Using the interface stiffness definition (2.2) and the interface energies (7.12), (7.14), the condition (2.14) can be written

$$h\left(\frac{\pi}{2} - \alpha_1\right) + h''\left(\frac{\pi}{2} - \alpha_1\right) > -\frac{\sigma_{GB}(\alpha_1, \alpha_2)}{\sigma_{SL}^0}, \quad (7.17)$$

which holds for any twice-differentiable anisotropy function $h(\theta)$. Apparently, the right-hand side is always negative and it is the term $h''(\frac{\pi}{2} - \alpha_1)$, which decides the stability. As stated before, the interface stiffness is only negative for forbidden angles, around maxima of the anisotropy function. Hence, the above condition may be violated only when the substrate normal is aligned with a forbidden angle. This conclusion stems from the problem geometry and energetics, it is independent of the form of anisotropy function $h(\theta)$.

After substitution of (2.5) into (2.14) and rearrangement, the second condition becomes

$$\cos\left[n\left(\frac{\pi}{2} - \alpha_1\right)\right] < \frac{1}{\Omega} \left(\frac{\sigma_{GB}(\alpha_1, \alpha_2)}{\sigma_{SL}^0} + 1 \right). \quad (7.18)$$

The right-hand side is always positive. Apparently, when the right-hand side is greater than 1, the triple junction configuration is stable for any bottom grain orientation α_1 . That certainly holds for weak anisotropies, i.e. when $\Omega \leq 1$. For stronger anisotropies $\Omega > 1$, the right-hand side may get smaller than 1 and some orientations α_1 then do not meet the stability condition. The stronger the anisotropy, the closer is the right-hand side to zero and the interval of unstable α_1 orientations is wider.

Effectively, the (3D) nucleation is blocked on high-energy crystal facets due to the strong anisotropy.

7.2.3 Shape factor-orientation maps

Here, the shape factor-orientation map is the 2D plot of the shape factor as function of the top and bottom grain orientation, i.e. $S(\alpha_1, \alpha_2)$. For isotropic nucleation, the solid-liquid interface had constant interface energy σ_{SL}^0 and the grain boundary followed the Read-Shockley dependence (7.10).

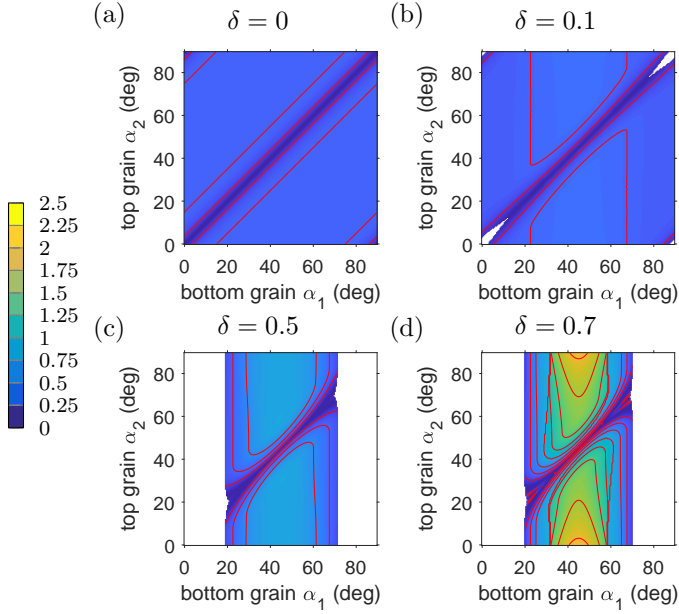


Figure 7.2: Shape factor-orientation maps for four different strengths of anisotropy in 4-fold symmetry (180x180 points). In (a) is the isotropic case, in (b)-(c) the anisotropic ones, the strength of anisotropy δ is indicated above. The white regions indicate the unstable orientations as by the condition (7.18). The levels are drawn with the increment of 0.25, like the colorbar spacing.

In anisotropic nucleation, the shape factor $S(\alpha_1, \alpha_2)$ was obtained from the generalized Winterbottom construction, with the wetting parameter $\Gamma(\alpha_1, \alpha_2)$ from (7.16). A solver was programmed in MATLAB, which found the possible solutions in the generalized Winterbottom construction and selected the one with the minimal area. It included all types of solutions discussed in this paper and it is available in Mendeley Data repository [41]. This solver was used to find $S(\alpha_1, \alpha_2)$ for all intended pairs of bottom and top grain orientations (α_1, α_2) .

Examples of the shape factor-orientation maps $S(\alpha_1, \alpha_2)$ for four different strengths of anisotropy in 4-fold symmetry are shown in Figure 7.2.

In Figure 7.2a, there is the map for the case of a particle with isotropic solid-liquid interface energy. There, the shape factor can be analytically determined, because the isolated equilibrium shape is a circle. Hence, the heterogeneous nucleus shape is a circular segment and from the basic geometric relations one

can write

$$S = \frac{\phi - \sin(\phi)}{2\pi}, \quad (7.19)$$

where ϕ is the central angle of the circular segment, which relates to the wetting parameter Γ (7.16) simply as

$$\phi = 2\cos(\Gamma). \quad (7.20)$$

Except for the regions of close orientations $\Delta\alpha \leq \Delta_{lim}$ (i.e. the diagonal and the corners of the map), there is constant $\Gamma = 0$, hence $\phi = \pi$ and $S = 0.5$ (i.e. the shape is a semicircle). For close orientations $\Delta\alpha \leq \Delta_{lim}$, the Read-Shockley grain boundary energy dependence implies smaller grain boundary energies (approaching 0 when the orientations are the same), which propagates through the equations for Γ , ϕ and eventually causes the drop of S to zero. That corresponds to wetting behavior (and larger nucleation probability).

The diagonal valley due to the misorientation dependence of the grain boundary energy is a feature common to all the maps.

Another common feature of the anisotropic maps in Figure 7.1b-d is that the low-energy bottom grain orientations (in the 4-fold case around $\alpha_1 \approx 45^\circ$, see Figure 7.1b) are associated with larger values of the shape factor, i.e. with a rather de-wetting behavior, where the equilibrium shapes are rather emerged than submerged. As a result, the nucleation probability is lower on the low-energy planes. That is understandable, because such planes are in an energetically convenient configuration and the nucleation event would disturb that. Nevertheless, together with the nuclei instability on high-energy planes, it implies that there is no simple rule to foresee, where the nucleation is most likely.

Apparently, the landscape in the shape factor-orientation map is more hilly with stronger anisotropy. For $\delta = 0.7$ in Figure 7.2d there even are regions $S(\alpha_1, \alpha_2) > 1$.

In Figure 7.2b and c, all points in the map correspond to the basic solution of truncated isolated Wulff shape, but in Figure 7.2d there are also inverted shape and emerged Wulff solutions. This variability in solutions determines the more complex landscape.

These shape factor-orientations maps were used as input to the Monte Carlo simulation of growing polycrystalline film, described in the following section.

7.3 Monte Carlo simulations

The purpose of this section is to qualitatively demonstrate the possible impact of anisotropy in nucleation barrier due to anisotropic solid-liquid interface energy on the texture evolution during film growth and compare it to the case with isotropic solid-liquid interface energy. The shape factor-orientation maps were used together with a Monte Carlo simulation of growing 2D polycrystalline film.

One of the common microstructures observed in films deposited by various deposition techniques features V-shaped grains in columns (seen in the cross-section). That one occurs when the grain boundary has significantly lesser mobility than the advancing surface, and at the same time some grains have a growth advantage in the competition. It can be explained by either anisotropy in interface energy or in the growth rate [69].

There were two main requirements specifying the developed model. Firstly, it was to have the capability to simulate a columnar growth of polycrystalline film in 2D, where the total surface energy is minimized in time by favouring low-energy grains in the competition (i.e. interface-energy minimizing texture). Secondly, it should support inclusion of the nucleation with anisotropic interface energy as introduced in the preceding sections.

The used programme was written in MATLAB and is available in Mendeley Data repository [41].

In the following subsections are subsequently described: the Monte Carlo method itself, the methodology and the results.

7.3.1 Algorithm description

The Monte Carlo model was inspired by [31, 32], but significantly modified.

The simulation was carried out on a fixed square grid, where every node (or pixel, abbreviated px) had a value between 0-50. The value 0 represented the parent solution and 1-50 represented the crystalline solid of different crystallographic orientations from the interval $\langle 0, 2\pi/n \rangle$. Each pixel could interact with its nearest and second nearest neighbors. The growth took place in the bottom-up direction, starting with a solid seed row, where random orientations were assigned to each pixel. In every column, there was one *growth site*, which was a liquid site having a solid neighbor on its bottom side, i.e. the first liquid site just above the deposit.

The simulation proceeded in iterations, one of which is described in a process

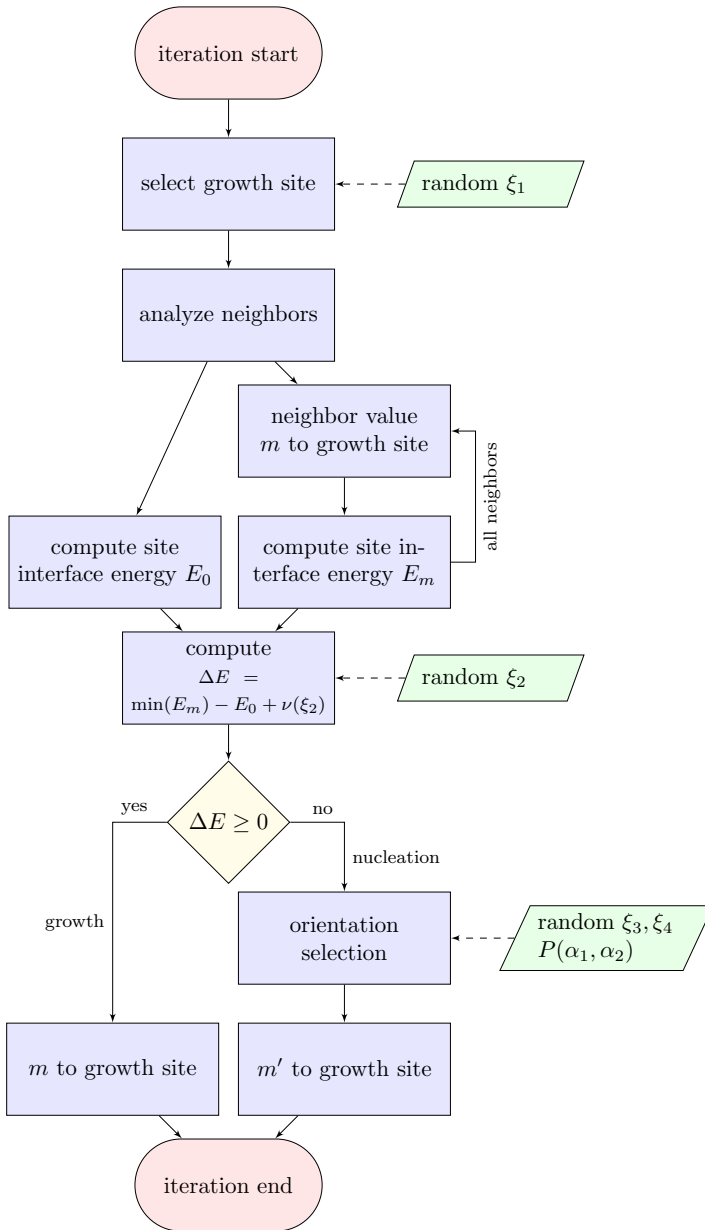


Figure 7.3: Process map of the Monte Carlo simulation with nucleation including anisotropic solid-liquid interface energy. In the model variant with no nucleation, the nucleation branch is omitted. In the model variant with isotropic nucleation, only ξ_3 is sampled and should the nucleation take place, the orientation is selected randomly.

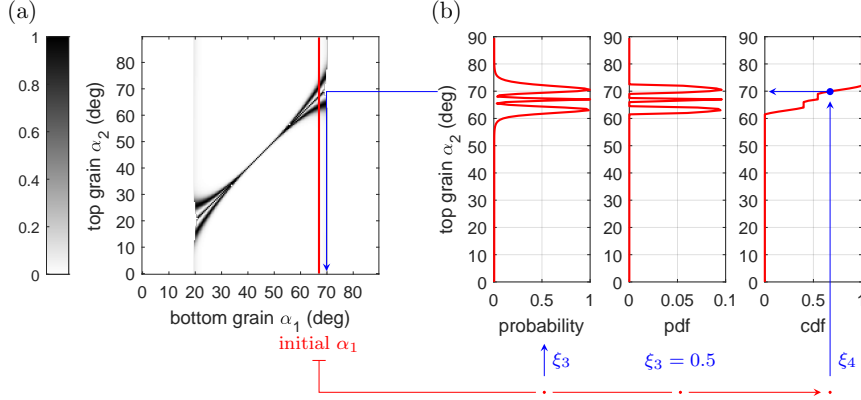


Figure 7.4: Single iteration of orientation selection algorithm. In (a) is the nucleation probability map $P(\alpha_1, \alpha_2) = \exp[(-10S(\alpha_1, \alpha_2))]$ for $n = 4$, $\delta = 0.7$. A slice at bottom grain orientation $\alpha_1 = 67^\circ$ was indicated as the initial α_1 . In (b) there is the respective slice of the probability map, from which the probability distribution function (pdf) and then the cumulative distribution function (cdf) of the top grain orientation are computed. The uniformly sampled ξ_3 is used in specification of the pdf (see text), here $\xi_3 = 0.5$ was used. Then, ξ_4 is used for sampling of the cdf to obtain the top grain orientation. The top grain orientation reached in this sampling is $\alpha_2 = 70^\circ$.

chart in Figure 7.3. Essentially, a growth site was first selected, its neighborhood analyzed and then it was decided whether either some neighbor value would be inserted to the growth site (the *growth* branch in the scheme) or whether a nucleation attempt would take place (the *nucleation* branch). The latter could be omitted to produce only anisotropic growth without nucleation.

In the neighborhood analysis, the site interface energy E_0 was first computed for the initial case (when the growth site was occupied by the liquid) as

$$E_0 = \sigma_S(\alpha_1) = \sigma_{SL}^0 h \left(\frac{\pi}{2} - \alpha_1 \right). \quad (7.21)$$

As can be seen, the assumed surface orientation in every growth site was $\theta = \frac{\pi}{2}$ (the growth direction). In this sense, the deposit is assumed to be flat. Secondly, the site interface energies $E_{m''}$ were computed for all the neighbor orientations m'' . In case of multiple different orientations m'' in the neighborhood, there would be multiple $E_{m''}$ site energies computed at this step as

$$E_{m''} = \sum_{i,nn} \sigma_i + w_{snn} \sum_{i,snn} \sigma_i + \sigma_S(\alpha_1). \quad (7.22)$$

The symbol σ_i stands for the interface energy between the individual nearest neighbors (nn) or second nearest neighbors (snn). All the interfacial energies were taken positive. The second nearest neighbors were included with the weight $0 < w_{snn} < 1$ depending on the order of symmetry n . For 4-fold symmetry it was $w_{snn} = 1/4.4 = 0.2273$ (see 7.3.2 for details).

Upon replacement of liquid by solid there occurs an energy change ΔE , which was computed using the lowest site energy of all the available orientations m'' , i.e.

$$\Delta E = \min(E_{m''}) - E_0 + \nu(\xi_2), \quad (7.23)$$

where the noise term $\nu(\xi_2)$ represents local energy fluctuations and is commented in more detail below. As indicated in the scheme, when it was $\Delta E \geq 0$, the growth proceeded with the orientation m'' with the minimal site energy. On the other hand, when it was $\Delta E < 0$, the nucleation trial took place and the orientation was determined using the orientation selection algorithm described below.

In growing bicrystal simulations (without the nucleation) it was validated that such growth algorithm mimics the columnar growth with interface-energy-minimizing textures sufficiently for the purpose of this study. Details about the validation simulations are provided in the 7.3.2.

The noise term $\nu(\xi_2)$ was relevant for the nucleation. Every time the growth site was not near a grain boundary (i.e. there was only single neighbor orientation m''), the only possible interfacial energy change was strictly zero, i.e. $\Delta E = 0$. That was because the interface energy between like orientations was zero, hence in this case $E_{m''} = E_0$. This energy change corresponded to growth (see the scheme in Figure 7.3), hence no nucleation could occur in these sites. Generally speaking, the nucleation is certainly not limited only to the grain boundaries intersecting the surface. In order to enable nucleation everywhere on the surface, the fluctuations $\nu(\xi_2)$ were added.

In absolute value, they were so small, that they did not affect the result of local energies comparison near the grain boundaries (i.e. in growth sites with multiple orientations m'' in the neighborhood). At the same time, the fluctuations had a finite value attaining the minus sign with a controlled probability (when $\Delta E < 0$, the nucleation trial occurred instead of growth). Specifically, the fluctuations were taken as

$$\nu(\xi_2) = a(\xi_2 - b), \quad (7.24)$$

where $a = 0.001\sigma_0$, $b = 0.25$ and $0 < \xi_2 < 1$ was sampled from the uniform distribution. Effectively, the parameter b controlled the density of nucleation attempts. With this particular parametrization, statistically every fourth growth site not adjacent to the grain boundary attempted to nucleate.

One nucleation attempt within the orientation selection algorithm is illustrated in Figure 7.4a-b. The orientation selection algorithm determined two things: i) whether anything nucleated and ii) with which orientation. Depending on the bottom grain orientation, there is a certain probability distribution for the top grain (nucleus) orientations, which derives from the nucleation probability map (see Figure 7.4a)

$$P(\alpha_1, \alpha_2) = \exp[-\beta S(\alpha_1, \alpha_2)] . \quad (7.25)$$

Should a random number drawn from uniform distribution be lower than the nucleation probability $P(\alpha_1, \alpha_2)$, the event takes place. This is the random number ξ_3 in the scheme in Figures 7.3 and 7.4. But after such sampling there possibly are multiple top grain orientations which could occur, i.e. such orientations α'_2 that $P(\alpha'_2) > \xi_3$ for given α_1 . Hence such probability density function (pdf) is used, which assigns zero nucleation probability to all α_2 orientations except for those α'_2 s. After computation of the corresponding cumulative distribution function (cdf), the top grain orientation can be sampled from the pdf created in the previous step (using random ξ_4 sampled from uniform distribution), as illustrated in Figure 7.4b.

Result of this iteration was either a new grain orientation or unsuccessful nucleation - that happened when the sampled $\xi_3 > P(\alpha_2)$ for all α_2 in the respective slice of the probability map. The growth site then remained liquid. Note though, that this was very unlikely for the demonstrative iteration in Figure 7.4, because it corresponds to high anisotropy and low nucleation barrier, which are strongly nucleation-favoring conditions. In general, however, the nucleation does not occur automatically, as can be seen in Figure 7.6, where the mean number of nucleation events clearly depends on the nucleation barrier β and the strength of anisotropy δ .

7.3.2 Validation of anisotropic growth

Let a planar surface in 3D be intersected by a grain boundary between two crystals with different surface energies. The in-plane capillary force acting on the triple junction line is equal to the difference in the respective surface energies and is independent of the anisotropic torque term [23].

The simulated bicrystal consisted of the maximum- and minimum-energy orientation for a given strength of anisotropy δ . With the anisotropy function (2.4) the maximal surface energy was thus $\sigma_{max} = \sigma_0(1 + \delta)$ and the minimal one $\sigma_{min} = \sigma_0(1 - \delta)$. The magnitude of in-plane force F_x on the junction is then

$$|F_x| = 2\sigma_0\delta . \quad (7.26)$$

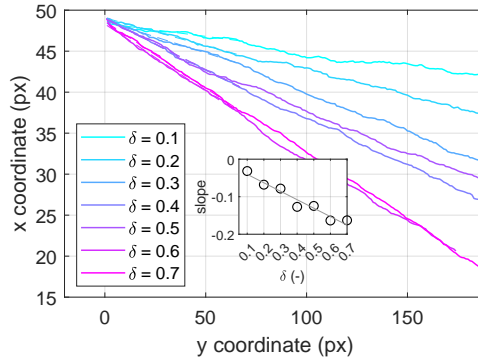


Figure 7.5: Mean trajectory of a triple point on the bicrystal surface during simulated growth for different strengths of anisotropy δ . The mean was taken from 30 runs in a system 100x200 px. The inset shows the slope of the trajectories and demonstrates that the greater was the anisotropy, the greater was the drag.

The sign of F_x is such to expand the low-energy half-plane on the expense of the high-energy one.

The simulations were carried out for a range of strengths of anisotropy δ . The second-nearest neighbor weight w_{snn} from (7.22) was optimized to observe a linear trend in the slope of the triple point trajectory during the simulation. There were always made 30 runs in a system 100x200 and the mean path was fitted by a straight line. The weight $w_{snn} = 1/4.4$ produced the trajectories as in the Figure 7.5. In the inset of this figure, the slopes were plotted as function of δ and the trend is certainly sufficiently linear for a qualitative study in this paper.

7.3.3 Methodology

In this study, three deposition scenarios were compared:

1. No nucleation (NN) - only anisotropic growth.
2. Isotropic nucleation (IN) - $S(\alpha_1, \alpha_2)$ as in Figure 7.2a.
3. Anisotropic nucleation (AN) - $S(\alpha_1, \alpha_2)$ as obtained by the generalized Winterbottom construction, e.g. like in Figure 7.2b-d. 4-fold symmetry was assumed.

Parameter	Values	Total
nucleation scenario	NN, IN, AN	3
initial condition	IC_A, IC_L, IC_H	3
strength of anisotropy δ	0.1, 0.3, 0.5, 0.7	4
non-dim. nucl. barrier β	10, (30), 50, 90	3 (4)

Table 7.1: Simulation conditions included in this study. Simulations at all combinations of the above parameters were run (except for those in parenthesis, which were combined only with some). In total, there were 116 simulation runs differing in these parameter combinations.

Because in the the anisotropic nucleation, the nucleation probability is a function of the bottom grain orientation, its manifestation depends on the initial texture, i.e. on the seed layer orientation distribution. For this reason, three different initial conditions were investigated, where the orientations were always drawn from uniform distribution, but from different domains:

1. IC_A: sampled from $\langle 0, 1 \rangle \frac{2\pi}{n}$, i.e. all orientations (theoretically, a deposition on amorphous substrate),
2. IC_L: sampled from $\langle 0.2, 0.8 \rangle \frac{2\pi}{n}$, i.e. in 4-fold symmetry centered around low-energy orientations ,
3. IC_H: sampled from $[\langle 0, 0.3 \rangle \cup \langle 0.7, 1 \rangle] \frac{2\pi}{n}$, i.e. in 4-fold symmetry centered around high-energy orientations.

The individual pixels in the seed layer were sampled independently, i.e. the intended grain size is 1 px. The conditions IC_H and IC_L both sample from the interval of orientations of width $0.6 \frac{2\pi}{n}$, which is wide enough to include at least part of both stable and unstable regions in both the conditions.

Additionally, the strength of anisotropy δ and the non-dimensional nucleation barrier β were varied. Specifically, all the different parameter values are summarized in Table 7.1.

A single simulation run took place in a rectangular system on a grid 1500x200. In order to gain better statistics on the through-thickness orientation evolution and the nucleation behavior, 10 repetitions were carried out and the results were either averaged or interpreted from one pseudo system 15000x200.

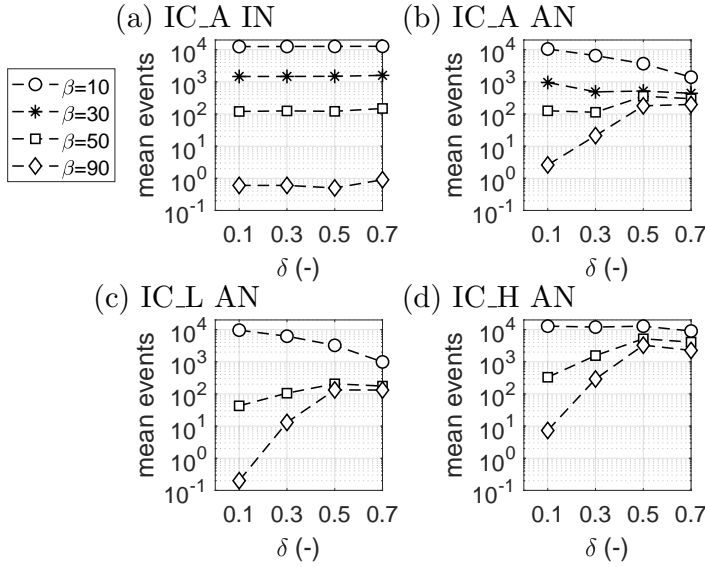


Figure 7.6: Mean number of nucleation events per single simulation run in the system 1500×200 for different initial conditions. The legend is common to all graphs, which all correspond to $n = 4, \delta = 0.5$. IC_A, IC_L and IC_H are the initial conditions (all orientations, low-energy orientations only and high-energy orientations only, respectively). IN and AN stand for the nucleation with isotropic and anisotropic solid-liquid interface energy, respectively.

7.3.4 Results

The presented results are based on analysis of 116 simulation runs, differing in the parameter combinations from Table 7.1.

In Figure 7.6, there is the mean of nucleation events (averaged over ten 1500×200 simulations) as a function of strength of anisotropy δ in series of nucleation barrier β and at different initial conditions. Figure 7.6a shows the result at initial condition IC_A, isotropic nucleation. In isotropic nucleation, the number of nucleation events was only dependent on the nucleation barrier β , not on the strength of anisotropy nor on the initial condition. Figure 7.6b shows the same initial condition (IC_A), but anisotropic nucleation. There, the number of nucleation events depends on both the strength of anisotropy δ and the nucleation barrier β . At small anisotropy, the dependence of mean events on β is similar to the isotropic nucleation. With increasing the strength of anisotropy, there is weaker dependence on β . It was observed, that even at otherwise

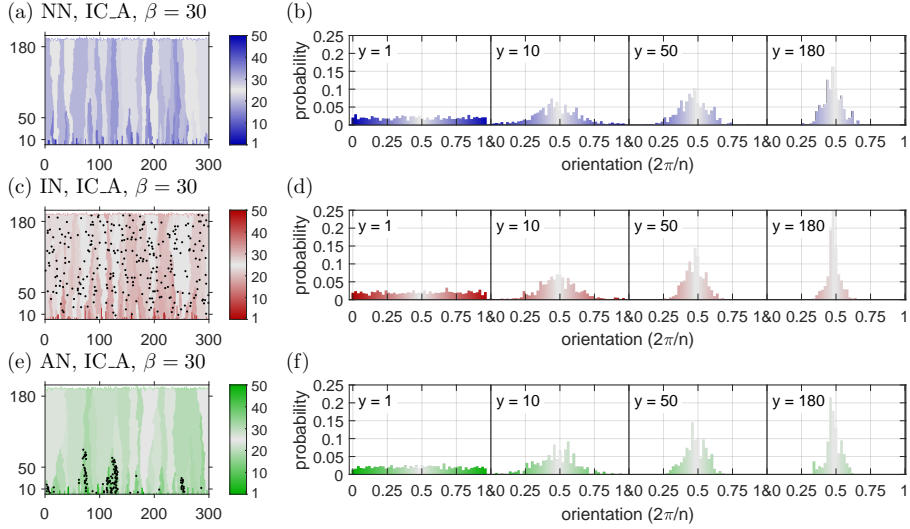


Figure 7.7: Deposits and their texture evolution in different nucleation scenarios and the initial condition IC_A, $\delta = 0.5$, $n = 4$ and $\beta = 30$. In (a), (b) is the no-nucleation scenario, in (c), (d) is isotropic nucleation and in (e), (f) is the anisotropic nucleation. In (a), (c) and (e) are the deposits, with the nucleation events indicated by black dots, and in (b), (d), (f) are the histograms of orientations in the indicated rows of the deposits. Light gray always corresponds to the low-energy orientations in both the deposits and histograms and the high-energy orientations are correspondingly color-coded in both plots of the same scenario.

prohibitively small nucleation barrier $\beta = 90$, hundreds of nucleation events occurred in the 1500×200 system for $\delta \geq 0.5$ and remained rather constant after increase to $\delta = 0.7$. On the other hand, at very low nucleation barrier $\beta = 10$, the mean events were decreasing when δ rose, approaching the same order of magnitude like in large nucleation barriers β . In Figure 7.6c, again the anisotropic nucleation is shown, now in the initial condition IC_L. With the seed layer bias towards low-energy orientations, the results are very similar to those in Figure 7.6b, only the numbers are slightly smaller. Larger difference was observed in Figure 7.6d, initial condition IC_H, anisotropic nucleation. With the seed layer centered around high-energy orientations, $10^3 - 10^4$ of events were observed even at very high nucleation barrier $\beta = 90$ for $\delta \geq 0.5$.

Figure 7.7 presents the resulting deposits and their texture evolution in the three deposition scenarios in IC_A at $\delta = 0.5$ and $\beta = 30$. The no-nucleation scenario in Figure 7.7a-b shows the bias towards the low-energy orientations

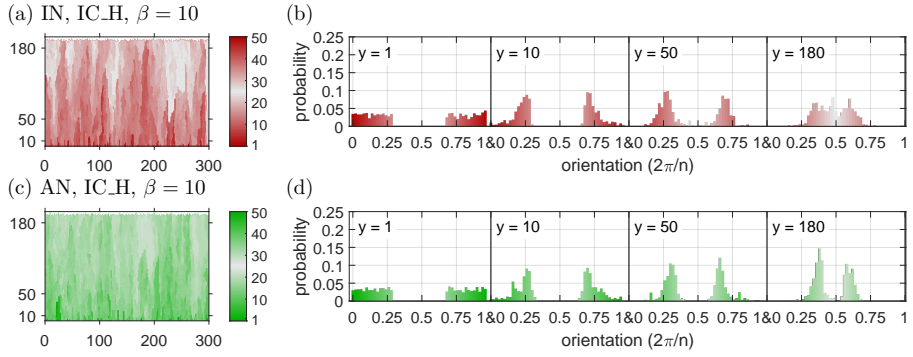


Figure 7.8: Deposits and their texture evolution in different nucleation scenarios and initial condition IC_H, $\delta = 0.5$ and $\beta = 10$. In (a), (b) is the isotropic nucleation scenario, in (c), (d) is anisotropic nucleation. The nucleation events are not shown, because they were too many. See caption of Figure 7.7 and the text for more details.

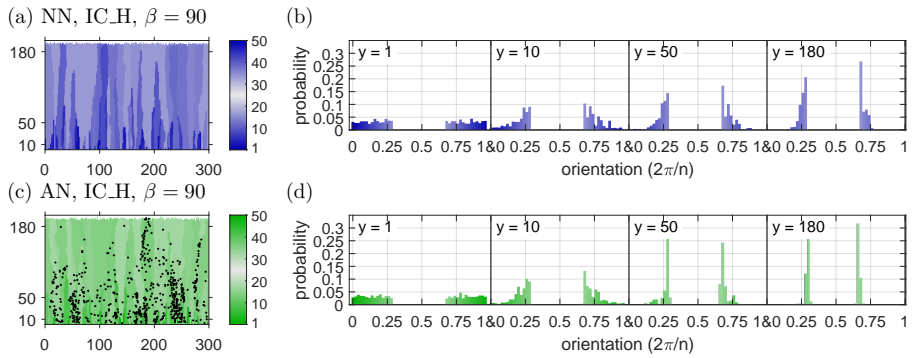


Figure 7.9: Deposits and their texture evolution in different nucleation scenarios and initial condition IC_H, $\delta = 0.5, n = 4$ and $\beta = 90$. In (a), (b) is the no-nucleation scenario, in (c), (d) is anisotropic nucleation. See caption of Figure 7.7 and the text for more details.

in the middle of the interval $(0, 1) \frac{2\pi}{4}$ with increasing film thickness. this is the desired and a characteristic feature of the model. All three deposition scenarios exhibit the columnar microstructure.

At this nucleation barrier β and initial condition, the mean number of nucleation events was comparable in the isotropic and anisotropic nucleation (see Figures 7.6a-b at $\delta = 0.5$). At first sight, the biggest difference between the isotropic and anisotropic nucleation scenarios is the spatial distribution of the nucleation events. While in the isotropic case (Figure 7.7c) the nucleation was uniform, in the anisotropic one (Figure 7.7e) it is clearly located only at specific grains, which were apparently favourably oriented for nucleation. There, nucleation occurred densely. This is mainly attributed to two factors: i) the stability condition prohibits nucleation on too high-energy-interface grains and ii) nucleation on the lowest-energy planes is the least probable of the allowed ones (and with strong enough anisotropy practically prohibited as well). Eventually, the nucleation took place on the bottom grain orientations near the edges of the stable orientations region, where the shape factor is closer to zero (see the map in Figure 7.2c, where it is also $\delta = 0.5$). The (nucleated) top grain orientation will mostly be close to the bottom grain orientation. The effect of nucleation on texture is such that the low-energy orientation texture is stronger near the film surface. This is probably because nucleation introduces single-pixel orientation inhomogeneities, which are easy for neighboring lower-energy grains to overgrow. The different spatial distribution of events in the isotropic and anisotropic nucleation scenarios affects the texture in the same way - i.e. in this case a mild increase in strength of the low-interface-energy texture.

On the other hand, the textures of scenarios with nucleation were not recognizable from the no-nucleation scenario when the mean number of events per simulation was in the order of magnitude 10^2 and smaller. In the initial condition IC_A, some effect is noticeable with 10^3 events per simulation (as in Figure 7.7) and above. Apparently, the effect of nucleation on texture will be stronger with more events taking place.

An example of deposits and texture evolution at high nucleation rate at $\beta = 10$ in isotropic and anisotropic nucleation scenario is in Figure 7.8 (as before, $\delta = 0.5, n = 4$). Note that the initial condition is IC_H, where the low-energy orientations are absent. Again, the mean number of nucleation events are comparable in the two scenarios. In the isotropic nucleation scenario (Figure 7.8a-b), some low-energy grains are eventually inserted (with equal probability as any other) and these would overtake given enough film thickness. Below the film surface (row 180, Figure 7.8b), the texture is already centered around the low-energy orientations with rather uniform distribution. On the other hand, in the anisotropic nucleation scenario (Figure 7.8c-d), the nucleation of low-energy grain is apparently much less likely than of other orientations.

This delays the introduction of the interface energy minimizing texture, as can be seen in Figure 7.8d, row 180, where the central minimum-energy orientations are still missing.

The anisotropic nature of nucleation thus imposed a different than interface energy minimizing texture, which is a very interesting observation. Note that the probability of minimum-energy grain insertion is non-zero, so in principle the interface-energy-minimizing texture under the surface is the expected terminal state. However, depending on the anisotropy and other conditions it may as well be unlikely within the practical deposition thicknesses.

Figure 7.9 presents the case of very high nucleation barrier $\beta = 90$, again in the initial condition IC_H (and $\delta = 0.5$, $n = 4$). There occurs nearly no nucleation in the isotropic nucleation scenario (on average less than 1 event per simulation), so it is identical to the no-nucleation scenario (shown in Figure 7.9a-b). As can be seen, the lowest-available-energy grains overtake as before, but there is no mechanism to introduce orientations absent in the seed layer. In the anisotropic nucleation scenario (Figure 7.9c-d), still about 10^3 of nucleation events took place despite the very high nucleation barrier β . That was possible because of the shape factor anisotropy - the local nucleation barrier $S(\alpha_1, \alpha_2)\beta$ was small enough for some orientations. However, the introduction of low-energy orientations did not take place, so the nucleation only supported the grains with initially-present lowest interface energy in the growth competition,

7.4 Comparison to experiment and discussion

The presented theory can be used to qualitatively explain some recent experimental results by Alimadadi et al. [2]. They studied the through-thickness texture evolution in Ni electrodeposited on amorphous substrate in four samples, each of which exhibited different dominant fiber texture. The only variables in the deposition were pH and deposition rate, the resulting thickness was different in every sample, but around 20 μm .

The sample deposited at the smallest rate of 0.533 nm/s (i.e. an order of magnitude smaller than the others, the current density being 0.2 A/dm²) exhibited sudden change of texture in the low thickness of 0-4 μm , as can be seen in Figure 7.10. The $\langle 100 \rangle$ texture in the nanocrystalline zone A below the 2 μm of thickness is gone in the pole figure of 2-4 μm , where the $\langle 110 \rangle$ component starts developing and later strengthens with increasing thickness. Very few grains reaching the surface could be traced back to the nanocrystalline zone A, which means that nucleation had to take place [2]. The nucleation was apparently anisotropic (with a bias towards $\langle 110 \rangle$). The combination of nuclei

density and their advantage in growth was able to set a completely new course to the texture evolution within a rather thin layer of the deposit.

In the other samples of Alimadadi, the initial texture contained the resulting dominant component, which gradually reinforced with thickness (similarly to how the sample in Figure 7.10 evolved from 2 μm on).

Interestingly, the nucleation in the discussed sample happened at very low growth rate, which in general implies high nucleation barriers. The nucleation barrier for the emerging nuclei had to be very small, though, because the nucleation took place regardless of the small driving force. The possibility of low nucleation barrier even with low driving force (given a convenient bottom grain orientation) was shown to be one of possible manifestations of anisotropic nucleation barrier (see Figure 7.9).

Detailed analysis of the possible competition between the interface-energy-minimization and strain-energy-minimization mechanisms of texture formation in this case is out of the scope of this paper. The sole fact that significant amount of anisotropic, growth-successful nuclei appeared at very low driving force is a peculiarity, which can be qualitatively explained by the presented results, though.

Possibly one mechanism sustained the texture by setting the rules for growth competition up to certain thickness. With the overtake of the other mechanism then, possibly the nuclei would suddenly have more chances in the growth competition. At the same time, the initial favourable-for-nucleation texture would still be in place, before overgrown by the nuclei.

An attempt to estimate the non-dimensional nucleation barrier β in the discussed experiment was made. However, with so small driving force, the effect of the (unknown) scaling interface energy σ_0 on the nucleation barrier is very large. The non-dimensional nucleation barrier β in multiples of kT then varied between 3 and 2950 for σ_0 equal to 0.1 and 1 J/m², respectively. The actual value of σ_0 cannot be reached, but if the nucleation barrier was so small due to the low σ_0 , a very high nucleation rate would be expected during the whole experiment. It would not explain the observed sudden change in the texture (supposedly due to nucleation) and the long columnar grains seen in this sample (see Figure 7.10) should not occur at all.

Alimadadi et. al [2] did not investigate in depth what mechanisms were responsible for the texture change in this sample. The hereby presented interpretation is extending their discussion and there are no points of disagreement.

Should the anisotropy function produce Wulff shape with facets, there would

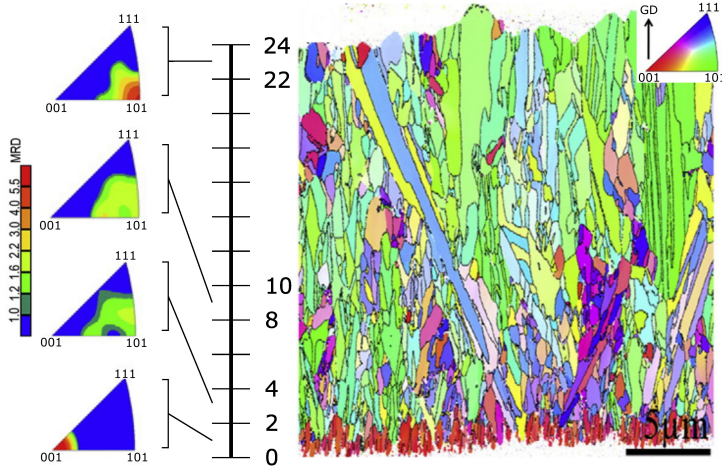


Figure 7.10: Experimental results of Ni electrodeposited on an amorphous substrate, adapted from [2]. On the right, an EBSD map of the deposit cross-section is shown, the inverse pole figure is in the top-right inset. The axis indicates the deposit thickness in μm . The pole figures on the left correspond to the indicated regions, their colorbar of MRD (Multiples of Random Distribution) is provided.

be no self-intersection of the Wulff plot, because that one is formed essentially by single orientation per facet. However, in such shapes, nearly all orientations are forbidden, i.e. with negative interface stiffness. We remind that not all the forbidden orientations are to fail the stability condition (7.17), but they are the candidates for doing so. The stability condition thus has possibly large implications for anisotropic nucleation in 2D space in general.

7.5 Conclusion

This chapter investigated implications of the anisotropy in interface energy for orientation selection in repeated nucleation during polycrystal deposition.

First, the wetting parameter Γ was expressed as a function of the top and bottom grain orientations in order to enable the generalized Winterbottom construction for each orientation combination. Novel solutions to the stable equilibrium shape were employed in very strong anisotropies. The shape factor-orientation maps were produced and used as input to the columnar growth simulation using the developed Monte Carlo method.

The obtained results essentially indicate that with stronger anisotropy, there is less effect of the non-dimensional homogeneous nucleation barrier on the nucleation rate. In a system with constant scalar interface energy σ_0 and temperature, that means lesser effect of the bulk driving force on nucleation behavior (see (7.6)).

On the other hand, the initial texture becomes significant or even leading factor. Depending on the initial texture, it was shown to be possible to either have no nucleation irrespective of the driving force (should the initial texture contain only forbidden orientations) or to have large nucleation rate even with very small driving forces. The latter option was speculated to be one of mechanisms leading the abrupt change in texture in one of samples in [2], the one shown in Figure 7.10 in this paper.

Three improvements of the generalized Winterbottom construction were worked out: (i) the new solutions of stable equilibrium shapes, originating from multiple self-intersecting Wulff plot occurring at very strong anisotropies, (ii) detailed description of the inverted shape solution in arbitrary orientation and (iii) the contact point stability condition for the nucleus as a function of both the top and bottom grain orientations. The latter is a strong influence on the model behavior. It masked the full orientation-shape factor map only to its part, where the nucleation is less probable, except for some areas near the edge of the stable angles interval. There, on the other hand, the nucleation barrier could be so small, that nucleation would proceed as well at very low driving forces.

The used MATLAB codes are available in a Mendeley Data repository [41].

Chapter 8

Conclusion

8.1 TODO Conclusion

8.2 TODO Outlook

The nucleus orientation sampling developed here could be used in a more sophisticated model of growing polycrystal to bring further insights. Other possible advancements include construction of the shape factor maps for 3D anisotropy function; coupling of the interface energy to local values of relevant fields, like adsorbent concentration (thus adding another dimension to the shape factor-orientation map) or include another anisotropy functions.

Appendix A

Functional derivative

The Allen-Cahn equation describing evolution of a non-conserved field $\xi(\mathbf{r})$ in a domain $\Omega \in \mathbb{R}^3$ with boundary $\partial\Omega$ can be written as

$$\frac{\partial \xi}{\partial t} = -L \frac{\delta F}{\delta \xi} \quad \text{in } \Omega \quad (\text{A.1})$$

$$\nabla \xi \cdot \mathbf{n} = 0 \quad \text{at } \partial\Omega, \quad (\text{A.2})$$

where L is a positive constant and the function $\frac{\delta F}{\delta \xi}$ stands for functional derivative of the free energy functional F . The latter expresses how much the energy changes when the function $\xi(\mathbf{r})$ is infinitesimally varied by addition of some test function multiplied by small number, i.e. multiplied by $\varepsilon g(\mathbf{r})$, where $0 < \varepsilon \ll 1$.

The functional is a map from some function space to real numbers and in our case $F[\xi(\mathbf{r})] = \int f(\mathbf{r}, \xi(\mathbf{r}), \nabla \xi(\mathbf{r})) dV$ with the integrand being energy density. The change in functional value depending on ε is called *functional variation* and is defined $\delta F = F[\xi(\mathbf{r}) + \varepsilon g(\mathbf{r})] - F[\xi(\mathbf{r})]$. The term $F[\xi(\mathbf{r}) + \varepsilon g(\mathbf{r})]$ can be seen as a function of ε and the functional derivative is a *functional* defined as

$$\frac{\delta F}{\delta \xi}[\xi, g] := \left[\frac{d}{d\varepsilon} F[\xi + \varepsilon g] \right]_{\varepsilon=0} = \lim_{\varepsilon \rightarrow 0} \frac{F[\xi(\mathbf{r}) + \varepsilon g(\mathbf{r})] - F[\xi(\mathbf{r})]}{\varepsilon} \quad (\text{A.3})$$

The functional F is *differentiable* when the derivative A.3 exists and can be written in form of integral

$$\left[\frac{d}{d\varepsilon} F[\xi + \varepsilon g] \right]_{\varepsilon=0} = \int_{\Omega} \frac{\delta F}{\delta \xi}(\mathbf{r}) g(\mathbf{r}) dV \quad (\text{A.4})$$

the kernel of which $\frac{\delta F}{\delta \xi}(\mathbf{r})$ is the *function* appearing in the Allen-Cahn equation. The expression for $\frac{\delta F}{\delta \xi}(\mathbf{r})$ can be obtained using Taylor expansion of $F[\xi(\mathbf{r}) + \varepsilon g(\mathbf{r})]$ in $\varepsilon = 0$, which will be shown first in the case of an 1D system to illustrate the procedure.

The functional is $F[\xi(x)] = \int_a^b f(x, \xi, \xi') dx$, where the integration limits a, b are constant and $\xi = \xi(x), \xi' = \frac{d\xi}{dx}(x)$. The functional derivative is then

$$\begin{aligned} \frac{\delta F}{\delta \xi}[\xi, g] &= \lim_{\varepsilon \rightarrow 0} \frac{1}{\varepsilon} \int_a^b [f(x, \xi + \varepsilon g, \xi' + \varepsilon g') - f(x, \xi, \xi')] dx = \\ &= \lim_{\varepsilon \rightarrow 0} \frac{1}{\varepsilon} \int_a^b \left[\frac{\partial f}{\partial \xi} \varepsilon g + \frac{\partial f}{\partial \xi'} \varepsilon g' + \mathcal{O}(\varepsilon^2) \right] dx = \\ &= \int_a^b \left(\frac{\partial f}{\partial \xi} g + \frac{\partial f}{\partial \xi'} g' \right) dx = \\ &= \int_a^b \left(\frac{\partial f}{\partial \xi} - \frac{\partial}{\partial x} \frac{\partial f}{\partial \xi'} \right) g dx + \left[\frac{\partial f}{\partial \xi'} g \right]_a^b \end{aligned} \quad (\text{A.5})$$

In the last equation sign per partes technique was used.

So far there was no assumption on test function $g(x)$, but in the simplest case the end points of ξ are fixed, i.e. $g(a) = g(b) = 0$, which removes the second term and allows to write

$$\frac{\delta F}{\delta \xi}(x) = \frac{\partial f}{\partial \xi} - \frac{\partial}{\partial x} \frac{\partial f}{\partial \xi'}. \quad (\text{A.6})$$

If the left-hand side is replaced by zero, we obtain *Euler-Lagrange* equation, solution to which minimizes the functional F .

Now, in the case of functional in 3D space $F[\xi(\mathbf{r})] = \int_{\Omega} f(\mathbf{r}, \xi(\mathbf{r}), \nabla \xi(\mathbf{r})) d^3r$ we must realize that dependence of the integrand on a vector variable means dependence on its components, i.e. $f(\mathbf{r}, \xi(\mathbf{r}), \nabla \xi(\mathbf{r})) = f(x_1, x_2, x_3, \xi, \partial_1 \xi, \partial_2 \xi, \partial_3 \xi)$, where $\partial_i = \frac{\partial}{\partial x_i}$. The functional derivative is then derived in a way analogous to the previous case, but now there is one term in the Taylor expansion per each gradient component. Before the derivation we define the following vector field

$$\begin{aligned} \frac{\partial f}{\partial (\nabla \xi)} &= \frac{\partial f}{\partial (\partial_1 \xi)} \mathbf{i} + \frac{\partial f}{\partial (\partial_2 \xi)} \mathbf{j} + \frac{\partial f}{\partial (\partial_3 \xi)} \mathbf{k} = \\ &= \frac{\partial f}{\partial (\frac{\partial \xi_p}{\partial x})} \mathbf{i} + \frac{\partial f}{\partial (\frac{\partial \xi_p}{\partial y})} \mathbf{j} + \frac{\partial f}{\partial (\frac{\partial \xi_p}{\partial z})} \mathbf{k} \end{aligned} \quad (\text{A.7})$$

And we proceed to the functional derivative

$$\begin{aligned}
 \frac{\delta F}{\delta \xi}[\xi, g] &= \lim_{\varepsilon \rightarrow 0} \frac{1}{\varepsilon} \int_{\Omega} [f(x_i, \xi + \varepsilon g, \partial_i(\xi + \varepsilon g)) - f(x_i, \xi, \partial_i \xi)] d^3 r = \\
 &= \lim_{\varepsilon \rightarrow 0} \frac{1}{\varepsilon} \int_{\Omega} \left[\frac{\partial f}{\partial \xi} \varepsilon g + \sum_{i=1}^3 \frac{\partial f}{\partial (\partial_i \xi)} \varepsilon \partial_i g + \mathcal{O}(\varepsilon^2) \right] d^3 r = \\
 &= \int_{\Omega} \left[\frac{\partial f}{\partial \xi} g + \frac{\partial f}{\partial (\nabla \xi)} \cdot \nabla g \right] d^3 r \\
 &= \int_{\Omega} \left[\frac{\partial f}{\partial \xi} - \nabla \cdot \frac{\partial f}{\partial (\nabla \xi)} \right] g d^3 r + \int_{\partial \Omega} g \frac{\partial f}{\partial (\nabla \xi)} \cdot d\mathbf{n}
 \end{aligned} \tag{A.8}$$

In the last equation there was used Stokes' theorem¹ in combination with the rule for divergence of product of vector and scalar field². Hence, in order to null the surface integral in equation A.8, either the boundary values must be fixed (Dirichlet BCs) or the following boundary condition (so called *natural BC*) must be satisfied

$$\frac{\partial f}{\partial (\nabla \xi_p)} \cdot \mathbf{n} = 0. \tag{A.9}$$

Different choice of the boundary conditions will interfere with minimization of the functional. The safest option is when the interface does not come near the boundary.

¹with scalar field $f(\mathbf{r})$ and vector field $\mathbf{F}(\mathbf{r})$ the Stokes theorem gives: $\int_{\Omega} \nabla \cdot (\mathbf{F}f) = \int_{\partial \Omega} f \mathbf{F} \cdot d\mathbf{n}$, where \mathbf{n} is a vector normal to the domain boundary
² $\nabla \cdot (\mathbf{F}f) = (\nabla \cdot \mathbf{F})f + \mathbf{F} \cdot (\nabla f)$

Appendix B

Supporting derivations in Moelans' model

Appendix C

Model parameters determination - best practices

The multi-phase field model by Moelans [47] is sensitive to how exactly the values of the parameters m, κ, γ are assigned in systems with anisotropic interface energy. In the model variants with variable interface width (IWvG and IWvK), it is important to assure that no interface becomes too narrow, so that grid pinning is prevented. Otherwise, the kinetics is no longer accurately reproduced by the implementation. The best practices in parameters determination described in this section were implemented in MATLAB functions, which were published in dataset [40], distributed under GPLv3 license.

C.1 Polynomial expressions for determination of γ

Interface energy and width are non-analytic functions of the parameter γ (equations (4.6) and (4.7) in the main text). In models IWc and IWvG with non-uniform interface energy, γ varies in space and depends on physical input (local interface energy σ) and chosen interface width. Assuming that κ, m and σ are known, $g(\gamma)$ is computed using equation (4.6) and must be inverted in order to obtain γ . For numeric convenience, functions $g^2 \rightarrow 1/\gamma$ and $1/\gamma \rightarrow f_{0,c}$ were fitted by polynomials using the tabulated values from [59]. The same approach was taken in [47]. Note that in one of the following subsections an alternative algorithm for determination of parameters in IWc is proposed. The values of $f_{0,c}(\gamma), g(\gamma)$ were tabulated and published in [59] in the range

$0.52 \leq \gamma \leq 40$. However, the polynomials used in both [47, 59] did not describe the functions along the whole tabulated range. For inconvenient input, that resulted in a loss of control over the interface properties (even negative values of γ were obtained).

To improve the parameters determination, the functions $g^2 \rightarrow 1/\gamma$ and $1/\gamma \rightarrow f_{0,c}$ were fitted again so that all γ values from the interval $0.52 \leq \gamma \leq 40$ were reliably available. The new polynomials show good agreement along the given interval and their coefficients are listed in Table C.1.

C.2 IWvG

This parameters determination algorithm [59] requires input of initializing interface energy σ_{init} , and width l_{init} which are assigned to interface with value $\gamma = 1.5$. There, the analytic relations between the model parameters are valid and the (constant) parameters κ, m can be computed:

$$\kappa = \frac{3}{4}\sigma_{init}l_{init} \quad , \quad m = 6\frac{\sigma_{init}}{l_{init}}. \quad (C.1)$$

These are then used in equation (4.6) with individual interface energies $\sigma_{i,j}$ to determine $g^2(\gamma_{i,j})$ and further $\gamma_{i,j}$ (using the first polynomial from Table C.1). However, because the said polynomial was only fitted in the interval $0.52 \leq \gamma \leq 40$ (values tabulated in [59]), it is important to choose the value of σ_{init} such, that none of the interface energies $\sigma_{i,j}$ should be described by $\gamma_{i,j}$ out of the interval. From equation (4.6) with substituted $\sqrt{\kappa m}$ from C.1 we show that the values do not leave the above interval when σ_{init} complies with the following two inequalities

$$\frac{\sigma_{max}}{g(40)}\sqrt{\frac{2}{9}} \leq \sigma_{init} \leq \frac{\sigma_{min}}{g(0.52)}\sqrt{\frac{2}{9}}, \quad (C.2)$$

where $\sigma_{min}, \sigma_{max}$ are minimal and maximal interface energy present in the system. Additionally, in order to fulfill these conditions, it must be satisfied that

$$\frac{\sigma_{min}}{\sigma_{max}} \geq \frac{g(0.52)}{g(40)} = \frac{0.1}{0.76} = 0.129, \quad (C.3)$$

which sets the maximal anisotropy in interface energy for which all $\gamma_{i,j}$ s may be determined in IWvG based on the values tabulated in [59].

Control over the width of the narrowest interface (with user-defined width l_{min}) is obtained when the parameters are determined in two steps as follows:

1. values of κ, m are calculated from equations (C.1) using appropriate σ_{init} together with l_{min}

Table C.1: Coefficients of the new polynomials used in the parameters determination algorithm (IWc and IWvG models). Based on fitting of the numeric values given in [59]. The polynomial of order N $p_N(x)$ is defined here together with its coefficients as $p_N(x) = \sum_{i=0}^N a_i x^{N-i}$. See text for details of use in the respective models.

	order	a_0	a_1	a_2	a_3	a_4	a_5	a_6
$g^2 \rightarrow \frac{1}{\gamma}$	6	-5.73008	18.8615	-23.0557	7.47952	8.33568	-8.01224	2.00013
$\frac{1}{\gamma} \rightarrow \sqrt{f_{0,c}}$	5	-0.072966	0.35784	-0.68325	0.63578	-0.48566	0.53703	
$g\sqrt{f_{0,c}} \rightarrow \frac{1}{\gamma}$	6	103.397	-165.393	105.3469	-44.55661	24.7348	-11.25718	1.999642

2. values of κ, m are recalculated from equations (C.1) with the same σ_{init} and interface width $l_{calib} = l_{min} \sqrt{8f_{0,c}(\gamma_{min})}$, where γ_{min} corresponds to the lowest value of all the $\gamma_{i,j}$ obtained in the previous step, i.e. to the interface with the largest interface energy σ_{max} .

After the second step, the interface with maximal interface energy will have the width l_{min} and all the other interfaces will have it equal or larger.

The other interface widths can be expressed

$$l_{i,j} = \frac{\sigma_{i,j}}{m} \frac{1}{g(\gamma_{i,j}) \sqrt{f_{0,c}(\gamma_{i,j})}} \quad (C.4)$$

C.3 IWc

The iterative parameters determining procedure assuring the constant interface width is described in [47]. The procedure requires initializing value of interface energy σ_{init} , which has decisive role for the parameters values. For inconvenient choice of σ_{init} , some of the parameters $\gamma_{i,j}$ may get out of range of applicability of the polynomials in Table C.1. Systematic investigation revealed that the value $\sigma_{init} = (\sigma_{max} + \sigma_{min})/2$ prevents occurrence of such effects for anisotropies $\sigma_{min}/\sigma_{max} \geq 0.03$.

Here we propose a simplified, yet equivalent single-step procedure. We assume constant interface width l and an initializing interface energy σ_{init} , for which $\gamma = 1.5$ and thus the analytic relations between the model parameters hold. As in the original iterative algorithm, the barrier height is computed

$$m = 6 \frac{\sigma_{init}}{l}. \quad (C.5)$$

Then, the gradient energy coefficient $\kappa_{i,j}$ can be expressed from both equations (4.7) and (4.8), hence we can write

$$\kappa_{i,j} = f_{0,c}(\gamma_{i,j}) m l^2 = \sigma_{i,j} l \frac{\sqrt{f_{0,c}(\gamma_{i,j})}}{g(\gamma_{i,j})}, \quad (C.6)$$

from where we obtain

$$g(\gamma_{i,j}) \sqrt{f_{0,c}(\gamma_{i,j})} = \frac{\sigma_{i,j}}{m l} = \frac{\sigma_{i,j}}{6 \sigma_{init}}. \quad (C.7)$$

In the last equation, m was substituted from (C.5). We denote $G(\gamma_{i,j}) = g(\gamma_{i,j}) \sqrt{f_{0,c}(\gamma_{i,j})}$. This function $\gamma \rightarrow G$ can be evaluated from the data tabulated in [59] and its inverse function $G \rightarrow \frac{1}{\gamma}$ was fitted by 6-th order

polynomial producing the coefficients in the last row of Table C.1. Apparently, evaluation of this polynomial in points $\sigma_{i,j}/6\sigma_{init}$ produces the searched $1/\gamma_{i,j}$. The gradient energy coefficients are then best computed as in C.6, where m was substituted from C.5:

$$\kappa_{i,j} = 6f_{0,c}(\gamma_{i,j})\sigma_{init}l. \quad (C.8)$$

Here, the fitted polynomial $\frac{1}{\gamma} \rightarrow \sqrt{f_{0,c}}$ is used to obtain the values of $f_{0,c}(\gamma_{i,j})$.

Similarly like in IWcG model, there are conditions limiting suitable values of σ_{init}

$$\frac{\sigma_{max}}{6G(40)} \leq \sigma_{init} \leq \frac{\sigma_{min}}{6G(0.52)}, \quad (C.9)$$

where $G(0.52) \approx 0.0069$, $G(40) \approx 0.4065$. Also must be satisfied

$$\frac{\sigma_{min}}{\sigma_{max}} \geq \frac{G(0.52)}{G(40)} = 0.017. \quad (C.10)$$

The main advantage of the proposed algorithm is that no iterations are needed for parameters determination. In the original algorithm the number of iteration steps is uncertain (tens of repetitions are not exceptional though) and sometimes the results may not converge due to reasons tedious to debug. Obtaining each parameter in a single step thus provides better control over the process and simplifies the implementation. Moreover, the permissible values of σ_{init} and the maximal anisotropy $\sigma_{min}/\sigma_{max}$ are clearly defined.

Also, it should be noted that when σ_{init} is chosen close to the upper limit in the inequality C.9, the determined $\gamma_{i,j}$ s are rather closer to value 0.52 (corresponding to long-tailed interfaces). When σ_{init} is near the bottom limit, the values of γ_{max} are close to the value 40 and γ_{min} are much larger than in the previous case. Near the limiting anisotropy $\sigma_{min}/\sigma_{max} \approx 0.017$, the values always are $\gamma_{max} \approx 40$ and $\gamma_{min} \approx 0.52$. It is especially near the limits of admissible σ_{init} , where the original iterative parameters assignment strategy is not always reliable when compared to the proposed one.

C.4 IWvK

When $\gamma = const = 1.5$, the analytic relations between the model parameters hold (i.e. equations (4.8)-(4.10)). Then, the minimal interface width l_{min} is controlled when

$$m = 6 \frac{\sigma_{min}}{l_{min}} \quad (C.11)$$

and

$$\kappa_{i,j} = \frac{9}{2} \frac{\sigma_{i,j}^2}{m}. \quad (C.12)$$

Interface width of an interface i - j can then be computed as

$$l_{i,j} = 6 \frac{\sigma_{i,j}}{m} . \quad (\text{C.13})$$

Appendix D

Implementation of finite difference method

D.1 General information

The 2D system was discretized into a rectangular equidistant grid and rearranged into a single column vector as indicated in figure D.1. The differential operators were represented by finite-difference matrices left-multiplying the column vectors standing for field variables present on the grid. The finite-difference matrices are block matrices, where each block is a square matrix acting on a single column in the rearranged system.

Let the system be a matrix with n rows and m columns. All blocks are matrices with dimensions $n \times n$ and they are ordered in $m \times m$ grid giving rise to an $mn \times mn$ sparse finite-difference matrix .

The finite-difference matrix can perform linear combination of arbitrary points in the system in each grid point. It takes various form depending on the boundary conditions. However, it is always a toeplitz block matrix.

Second-order accurate centered finite-difference scheme in space and first-order in time (i.e. the Euler method) were used.

In the following sections, the symbol \mathbb{O} stands for $n \times n$ block matrix of zeros and \mathbb{I} for $n \times n$ identity matrix (i.e. matrix with ones in the diagonal and zeros otherwise). The finite difference method is abbreviated as FD in the following. In the finite-difference matrices below, some elements may be highlighted in red. These are the elements, which are involved in the boundary conditions.

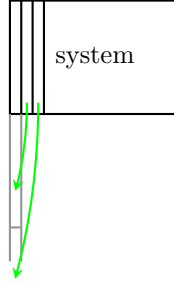


Figure D.1: Rearrangement of the matrix representing the system before application of the discrete differential operators.

D.2 Ghost nodes in Neumann boundary condition

D.2.1 Zero Neumann BCs

Neumann boundary conditions were implemented using ghost nodes. Ghost nodes are hypothetical nodes adjacent to the boundary nodes, in which the values can be specified using the given boundary condition. In order to have the derivatives in the boundary nodes second-order-accurate, centered difference can be used using the known values at ghost nodes. In the case $\nabla\eta \cdot \mathbf{n} = 0$ we can write at the left boundary edge (i.e. $x = 0$), where $(i, j) = (0, j)$

$$\begin{aligned} \frac{\partial\eta}{\partial x} = 0 \quad \text{at } x = 0 \quad \Rightarrow \quad \forall j \in m+1 \quad (\Delta_x\eta)_{0j} = \frac{\eta_{1j} - \eta_{-1j}}{h} = 0 \quad \Rightarrow \quad \eta_{1j} = \eta_{-1j} \\ \frac{\partial\eta}{\partial y} = 0 \quad \text{at } x = 0 \quad \Rightarrow \quad \forall i \in n+1 \quad (\Delta_y\eta)_{0j} = \frac{\eta_{ij+1} - \eta_{ij-1}}{h} \end{aligned} \quad (\text{D.1})$$

The first equation provides the value at the ghost node. In order to have the centered difference in the respective direction zero at the boundary, apparently the value must be equal to the value in the neighbour on the opposite side.

D.2.2 General Neumann BCs

The boundary condition defining the inclination angle θ at the boundary is $\nabla\eta \cdot \mathbf{n} = |\nabla\eta| \cos(\theta)$. This expression implies at the left boundary $(i, j) = (0, j)$ that $\frac{\partial\eta}{\partial x} = |\nabla\eta| \cos(\theta)$ and $\frac{\partial\eta}{\partial y} = |\nabla\eta| \sin(\theta)$. By replacing the partial derivatives $\frac{\partial}{\partial x}, \frac{\partial}{\partial y}$ with finite differences Δ_x, Δ_y the values in ghost node $(-1, j)$ can be

expressed as

$$\forall j \in m+1 \quad (\Delta_x \eta)_{0j} = \frac{\eta_{1j} - \eta_{-1j}}{2h} = |\nabla \eta|_{0,j} \cos(\theta) \quad (\text{D.2})$$

$$\implies \quad \eta_{-1j} = \eta_{1j} - 2h|\nabla \eta|_{0j} \cos(\theta). \quad (\text{D.3})$$

At the right boundary $(i, j) = (n, j)$ the ghost nodes $(n+1, j)$ are

$$\forall j \in m+1 \quad (\Delta_x \eta)_{nj} = \frac{\eta_{n+1j} - \eta_{n-1j}}{2h} = |\nabla \eta|_{nj} \cos(\theta) \quad (\text{D.4})$$

$$\implies \quad \eta_{n+1j} = \eta_{n-1j} + 2h|\nabla \eta|_{nj} \cos(\theta). \quad (\text{D.5})$$

And at the bottom and top, respectively, using the same principles we obtain

$$\forall i \in n+1 \quad \eta_{i,-1} = \eta_{i,1} - 2h|\nabla \eta|_{i,0} \cos(\theta) \quad (\text{D.6})$$

$$\forall i \in n+1 \quad \eta_{i,m+1} = \eta_{i,m-1} + 2h|\nabla \eta|_{i,m} \cos(\theta). \quad (\text{D.7})$$

Important observation is that the general Neumann BC indeed reduces to the zero condition for $\theta = 90^\circ$ and that the values at the ghost nodes are always derived from the neighbour on the opposite side.

D.3 First-order derivatives in FD

The centered finite difference was used with stencil $\begin{bmatrix} -1 & 0 & 1 \end{bmatrix}$ for x-direction

derivative and $\begin{bmatrix} 1 \\ 0 \\ -1 \end{bmatrix}$ for y-direction derivative.

D.3.1 Periodic boundary conditions

For the y-direction derivative the FD matrix is

$$\frac{\partial}{\partial y} \approx \Delta_y = \frac{1}{2h} \begin{pmatrix} Y & \emptyset & \emptyset & \dots & \emptyset & \emptyset \\ \emptyset & Y & \emptyset & \dots & \emptyset & \emptyset \\ \emptyset & \emptyset & Y & \dots & \emptyset & \emptyset \\ \vdots & \vdots & \vdots & \ddots & \vdots & \vdots \\ \emptyset & \emptyset & \emptyset & \dots & Y & \emptyset \\ \emptyset & \emptyset & \emptyset & \dots & \emptyset & Y \end{pmatrix} \quad (\text{D.8})$$

with

$$\mathbb{Y} = \begin{pmatrix} 0 & 1 & 0 & 0 & \dots & 0 & 0 & -1 \\ -1 & 0 & 1 & 0 & \dots & 0 & 0 & 0 \\ 0 & -1 & 0 & 1 & \dots & 0 & 0 & 0 \\ \vdots & \vdots & \vdots & \ddots & \vdots & \vdots & \vdots & \vdots \\ 0 & 0 & 0 & 0 & \dots & -1 & 0 & 1 \\ 1 & 0 & 0 & 0 & \dots & 0 & -1 & 0 \end{pmatrix} \quad (\text{D.9})$$

In the x-direction, the finite difference matrix is

$$\frac{\partial}{\partial x} \approx \Delta_x = \frac{1}{2h} \begin{pmatrix} \mathbb{O} & \mathbb{I} & \mathbb{O} & \mathbb{O} & \dots & \mathbb{O} & \mathbb{O} & -\mathbb{I} \\ -\mathbb{I} & \mathbb{O} & \mathbb{I} & \mathbb{O} & \dots & \mathbb{O} & \mathbb{O} & \mathbb{O} \\ \mathbb{O} & -\mathbb{I} & \mathbb{O} & \mathbb{I} & \dots & \mathbb{O} & \mathbb{O} & \mathbb{O} \\ \vdots & \vdots & \vdots & \ddots & \vdots & \vdots & \vdots & \vdots \\ \mathbb{O} & \mathbb{O} & \mathbb{O} & \mathbb{O} & \dots & -\mathbb{I} & \mathbb{O} & \mathbb{I} \\ \mathbb{I} & \mathbb{O} & \mathbb{O} & \mathbb{O} & \dots & \mathbb{O} & -\mathbb{I} & \mathbb{O} \end{pmatrix}. \quad (\text{D.10})$$

D.3.2 Neumann boundary conditions

The FD matrices are equal in both cases of the zero and general NBC, but in the case of the general NBC the following vector must be added at the left and right boundary $|\nabla\eta| \begin{bmatrix} \cos(\theta) \\ \sin(\theta) \end{bmatrix}$ and the following one at the bottom and top boundary $|\nabla\eta| \begin{bmatrix} -\sin(\theta) \\ \cos(\theta) \end{bmatrix}$.

For the y-direction the FD matrix is the same as for the periodic boundary conditions in the block structure (equation D.32), and the block matrix \mathbb{Y} is only modified in its first and last row as

$$\mathbb{Y} = \begin{pmatrix} 0 & 0 & 0 & 0 & \dots & 0 & 0 & 0 \\ -1 & 0 & 1 & 0 & \dots & 0 & 0 & 0 \\ 0 & -1 & 0 & 1 & \dots & 0 & 0 & 0 \\ \vdots & \vdots & \vdots & \ddots & \vdots & \vdots & \vdots & \vdots \\ 0 & 0 & 0 & 0 & \dots & -1 & 0 & 1 \\ 0 & 0 & 0 & 0 & \dots & 0 & 0 & 0 \end{pmatrix} \quad (\text{D.11})$$

For the x-direction with Neumann boundary conditions

$$\frac{\partial}{\partial x} \approx \Delta_x = \frac{1}{2h} \begin{pmatrix} \mathbb{O} & \mathbb{O} & \mathbb{O} & \mathbb{O} & \dots & \mathbb{O} & \mathbb{O} & \mathbb{O} \\ -\mathbb{I} & \mathbb{O} & \mathbb{I} & \mathbb{O} & \dots & \mathbb{O} & \mathbb{O} & \mathbb{O} \\ \mathbb{O} & -\mathbb{I} & \mathbb{O} & \mathbb{I} & \dots & \mathbb{O} & \mathbb{O} & \mathbb{O} \\ \vdots & \vdots & \vdots & \ddots & \vdots & \vdots & \vdots & \vdots \\ \mathbb{O} & \mathbb{O} & \mathbb{O} & \mathbb{O} & \dots & -\mathbb{I} & \mathbb{O} & \mathbb{I} \\ \mathbb{O} & \mathbb{O} & \mathbb{O} & \mathbb{O} & \dots & \mathbb{O} & \mathbb{O} & \mathbb{O} \end{pmatrix} \quad (\text{D.12})$$

D.3.3 Mixed boundary conditions

In 2D system there are only two options when combining periodic and Neumann BCs: the periodic boundary is either parallel to x or y axis. The periodic boundary must always lay opposite to another periodic boundary. In a system with mixed boundaries the finite difference matrices in the x and y direction are combined from the above options so that the BCs are met at the corresponding boundary.

D.4 Laplacian in 2D

5-point stencil $\begin{array}{c|c|c} 0 & 1 & 0 \\ \hline 1 & -4 & 1 \\ \hline 0 & 1 & 0 \end{array}$ approximates 2D laplacian $\nabla^2 u = u_{xx} + u_{yy}$ on an bi-equidistant grid with spacing h in a grid point (i, j) as

$$(\nabla^2 u)_{ij}^{5p} = u_{ij,xx} + u_{ij,yy} = \frac{1}{h^2} (-4u_{ij} + u_{i-1j} + u_{i+1j} + u_{ij-1} + u_{ij+1}) + \mathcal{O}(h^4) \quad (\text{D.13})$$

9-point stencil (denoted 9p8) $\begin{array}{c|c|c} 1 & 1 & 1 \\ \hline 1 & -8 & 1 \\ \hline 1 & 1 & 1 \end{array}$ is expressed in a grid point (i, j) as

$$\begin{aligned} (\nabla^2 u)_{ij}^{9p8} = \frac{1}{3h^2} & (-8u_{ij} + u_{i-1j} + u_{i+1j} + u_{ij-1} + u_{ij+1} + \\ & + u_{i+1j+1} + u_{i-1j-1} + u_{i-1j+1} + u_{i+1j-1}) + \mathcal{O}(h^4) \end{aligned} \quad (\text{D.14})$$

9-point stencil (denoted 9p20) $\begin{array}{c|c|c} 1 & 4 & 1 \\ \hline 4 & -20 & 4 \\ \hline 1 & 4 & 1 \end{array}$ is expressed in a grid point (i, j) as

$$(\nabla^2 u)_{ij}^{9p20} = \frac{1}{6h^2} [-20u_{ij} + 4(u_{i-1j} + u_{i+1j} + u_{ij-1} + u_{ij+1}) + u_{i+1j+1} + u_{i-1j-1} + u_{i-1j+1} + u_{i+1j-1}] + \mathcal{O}(h^4) \quad (D.15)$$

The above formulas are derived from Taylor expansions of the values of function u at the points adjacent to (i, j) assuming the small displacement h in both x and y direction.

The above formulas are represented by matrix, which carries the weighted summation of the function values for each point similarly to the first-order derivatives. Below, the matrices are shown in detail depending on the BCs.

D.4.1 Periodic boundary conditions

For 5p stencil the blocks are unit matrix \mathbb{I} , zero matrix \mathbb{O} and the following matrix \mathbb{D}_P^{5p} (the red elements are the top-bottom periodic condition)

$$\mathbb{D}_P^{5p} = \begin{pmatrix} -4 & 1 & 0 & 0 & \dots & 0 & 0 & \textcolor{red}{1} \\ 1 & -4 & 1 & 0 & \dots & 0 & 0 & 0 \\ 0 & 1 & -4 & 1 & \dots & 0 & 0 & 0 \\ \vdots & \vdots & \vdots & \vdots & \ddots & \vdots & \vdots & \vdots \\ 0 & 0 & 0 & 0 & \dots & 1 & -4 & 1 \\ \textcolor{red}{1} & 0 & 0 & 0 & \dots & 0 & 1 & -4 \end{pmatrix}. \quad (D.16)$$

and the finite-difference matrix \mathbb{L}_P^{5p} is ordered as follows (red elements are the left-right periodic boundary condition)

$$\mathbb{L}_P^{5p} = \frac{1}{h^2} \begin{pmatrix} \mathbb{D}_P^{5p} & \mathbb{I} & \mathbb{O} & \mathbb{O} & \dots & \mathbb{O} & \mathbb{O} & \textcolor{red}{\mathbb{I}} \\ \mathbb{I} & \mathbb{D}_P^{5p} & \mathbb{I} & \mathbb{O} & \dots & \mathbb{O} & \mathbb{O} & \mathbb{O} \\ \mathbb{O} & \mathbb{I} & \mathbb{D}_P^{5p} & \mathbb{I} & \dots & \mathbb{O} & \mathbb{O} & \mathbb{O} \\ \vdots & \vdots & \vdots & \vdots & \ddots & \vdots & \vdots & \vdots \\ \mathbb{O} & \mathbb{O} & \mathbb{O} & \mathbb{O} & \dots & \mathbb{I} & \mathbb{D}_P^{5p} & \mathbb{I} \\ \textcolor{red}{\mathbb{I}} & \mathbb{O} & \mathbb{O} & \mathbb{O} & \dots & \mathbb{O} & \mathbb{I} & \mathbb{D}_P^{5p} \end{pmatrix} \quad (D.17)$$

For 9p20 stencil the blocks are a Toeplitz matrix \mathbb{D}_P^{9p20} , a Toeplitz matrix \mathbb{A} and a zero matrix \mathbb{O} . These are defined

$$\mathbb{D}_P^{9p20} = \begin{pmatrix} -20 & 4 & 0 & 0 & \dots & 0 & 0 & \textcolor{red}{4} \\ 4 & -20 & 4 & 0 & \dots & 0 & 0 & 0 \\ 0 & 4 & -20 & 4 & \dots & 0 & 0 & 0 \\ \vdots & \vdots & \vdots & \vdots & \ddots & \vdots & \vdots & \vdots \\ 0 & 0 & 0 & 0 & \dots & 4 & -20 & 4 \\ \textcolor{red}{4} & 0 & 0 & 0 & \dots & 0 & 4 & -20 \end{pmatrix} \quad (\text{D.18})$$

$$\mathbb{A} = \begin{pmatrix} 4 & 1 & 0 & 0 & \dots & 0 & 0 & \textcolor{red}{1} \\ 1 & 4 & 1 & 0 & \dots & 0 & 0 & 0 \\ 0 & 1 & 4 & 1 & \dots & 0 & 0 & 0 \\ \vdots & \vdots & \vdots & \vdots & \ddots & \vdots & \vdots & \vdots \\ 0 & 0 & 0 & 0 & \dots & 1 & 4 & 1 \\ \textcolor{red}{1} & 0 & 0 & 0 & \dots & 0 & 1 & 4 \end{pmatrix} \quad (\text{D.19})$$

and arranged

$$\mathbb{L}_P^{9p20} = \frac{1}{6h^2} \begin{pmatrix} \mathbb{D}_P^{9p20} & \mathbb{A} & \mathbb{O} & \mathbb{O} & \dots & \mathbb{O} & \mathbb{O} & \textcolor{red}{\mathbb{A}} \\ \mathbb{A} & \mathbb{D}_P^{9p20} & \mathbb{A} & \mathbb{O} & \dots & \mathbb{O} & \mathbb{O} & \mathbb{O} \\ \mathbb{O} & \mathbb{A} & \mathbb{D}_P^{9p20} & \mathbb{A} & \dots & \mathbb{O} & \mathbb{O} & \mathbb{O} \\ \vdots & \vdots & \vdots & \vdots & \ddots & \vdots & \vdots & \vdots \\ \mathbb{O} & \mathbb{O} & \mathbb{O} & \mathbb{O} & \dots & \mathbb{A} & \mathbb{D}_P^{9p20} & \mathbb{A} \\ \textcolor{red}{\mathbb{A}} & \mathbb{O} & \mathbb{O} & \mathbb{O} & \dots & \mathbb{O} & \mathbb{A} & \mathbb{D}_P^{9p20} \end{pmatrix} \quad (\text{D.20})$$

D.4.2 Neuman boundary conditions

For both zero and general NBCs the FD matrices are equal. Because the value at ghost nodes is either equal or derived from value of neighbour on the opposite side, the laplacian stencil behaves at the Neumann boundary as in Figure D.2.

The 5p stencil finite-difference matrix \mathbb{L}_N^{5p} with Neuman BC is composed of 4 different blocks: tridiagonal \mathbb{D}_N^{5p} , unit matrix \mathbb{I} , $2\mathbb{I}$ and zero matrix \mathbb{O} . These

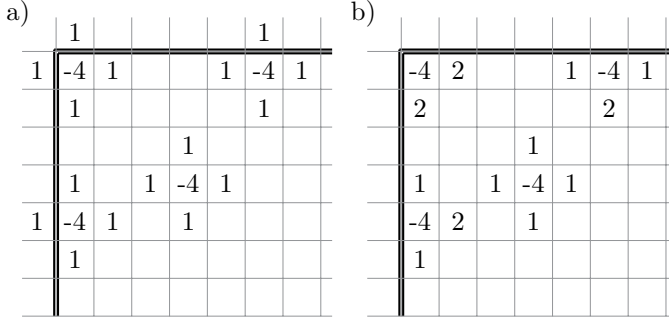


Figure D.2: Effect of Neuman BC on the 5pt laplacian stencil on the boundary points. Ghost points are outside the simulation domain but they can be accounted for thanks to knowing their value from equation D.1.

are:

$$\mathbb{D}_N^{5p} = \begin{pmatrix} -4 & \color{red}{2} & 0 & 0 & \dots & 0 & 0 & 0 \\ 1 & -4 & 1 & 0 & \dots & 0 & 0 & 0 \\ 0 & 1 & -4 & 1 & \dots & 0 & 0 & 0 \\ \vdots & \vdots & \vdots & \vdots & \ddots & \vdots & \vdots & \vdots \\ 0 & 0 & 0 & 0 & \dots & 1 & -4 & 1 \\ 0 & 0 & 0 & 0 & \dots & 0 & \color{red}{2} & 4 \end{pmatrix} \quad (\text{D.21})$$

(D.22)

and are ordered as follows

$$\mathbb{L}_N^{5p} = \frac{1}{h^2} \begin{pmatrix} \mathbb{D}_N^{5p} & \color{red}{2\mathbb{I}} & \mathbb{O} & \mathbb{O} & \dots & \mathbb{O} & \mathbb{O} & \mathbb{O} \\ \mathbb{I} & \mathbb{D}_N^{5p} & \mathbb{I} & \mathbb{O} & \dots & \mathbb{O} & \mathbb{O} & \mathbb{O} \\ \mathbb{O} & \mathbb{I} & \mathbb{D}_N^{5p} & \mathbb{I} & \dots & \mathbb{O} & \mathbb{O} & \mathbb{O} \\ \vdots & \vdots & \vdots & \vdots & \ddots & \vdots & \vdots & \vdots \\ \mathbb{O} & \mathbb{O} & \mathbb{O} & \mathbb{O} & \dots & \mathbb{I} & \mathbb{D}_N^{5p} & \mathbb{I} \\ \mathbb{O} & \mathbb{O} & \mathbb{O} & \mathbb{O} & \dots & \mathbb{O} & \color{red}{2\mathbb{I}} & \mathbb{D}_N^{5p} \end{pmatrix} \quad (\text{D.23})$$

In case of general NBC in 5-point stencil there must always be added or subtracted the term $2h|\nabla\eta|_{ij}\cos(\theta)$, where (i, j) are the boundary points. At the left and bottom boundary it is subtracted, at the right and top it is added.

The 9p20 stencil finite-difference matrix \mathbb{L}_N^{9p20} with Neuman BC is composed of 4 different blocks: tridiagonal \mathbb{D}_N^{9p20} , tridiagonal \mathbb{B} , $2\mathbb{B}$ and zero matrix \mathbb{O} . These

are

$$\mathbb{D}_N^{9p20} = \begin{pmatrix} -20 & \textcolor{red}{8} & 0 & 0 & \dots & 0 & 0 & 0 \\ 4 & -20 & 4 & 0 & \dots & 0 & 0 & 0 \\ 0 & 4 & -20 & 4 & \dots & 0 & 0 & 0 \\ \vdots & \vdots & \vdots & \vdots & \ddots & \vdots & \vdots & \vdots \\ 0 & 0 & 0 & 0 & \dots & 4 & -20 & 4 \\ 0 & 0 & 0 & 0 & \dots & 0 & \textcolor{red}{8} & -20 \end{pmatrix} \quad (\text{D.24})$$

$$\mathbb{B} = \begin{pmatrix} 4 & \textcolor{red}{2} & 0 & 0 & \dots & 0 & 0 & 0 \\ 1 & 4 & 1 & 0 & \dots & 0 & 0 & 0 \\ 0 & 1 & 4 & 1 & \dots & 0 & 0 & 0 \\ \vdots & \vdots & \vdots & \vdots & \ddots & \vdots & \vdots & \vdots \\ 0 & 0 & 0 & 0 & \dots & 1 & 4 & 1 \\ 0 & 0 & 0 & 0 & \dots & 0 & \textcolor{red}{2} & 4 \end{pmatrix} \quad (\text{D.25})$$

and are ordered as follows

$$\mathbb{L}_N^{9p20} = \frac{1}{6h^2} \begin{pmatrix} \mathbb{D}_N^{9p20} & \textcolor{red}{2}\mathbb{B} & \mathbb{O} & \mathbb{O} & \dots & \mathbb{O} & \mathbb{O} & \mathbb{O} \\ \mathbb{B} & \mathbb{D}_N^{9p20} & \mathbb{B} & \mathbb{O} & \dots & \mathbb{O} & \mathbb{O} & \mathbb{O} \\ \mathbb{O} & \mathbb{B} & \mathbb{D}_N^{9p20} & \mathbb{B} & \dots & \mathbb{O} & \mathbb{O} & \mathbb{O} \\ \vdots & \vdots & \vdots & \vdots & \ddots & \vdots & \vdots & \vdots \\ \mathbb{O} & \mathbb{O} & \mathbb{O} & \mathbb{O} & \dots & \mathbb{B} & \mathbb{D}_N^{9p20} & \mathbb{B} \\ \mathbb{O} & \mathbb{O} & \mathbb{O} & \mathbb{O} & \dots & \mathbb{O} & \textcolor{red}{2}\mathbb{B} & \mathbb{D}_N^{9p20} \end{pmatrix} \quad (\text{D.26})$$

In case of general NBC in 9-point stencil the term $2h|\nabla\eta|_{ij}\cos(\theta)$ must be added or subtracted (depending on the boundary) correspondingly to the stencil, e.g. at the left boundary

$$\frac{1}{6h^2} \begin{array}{c|c|c} 1 & 4 & 1 \\ \hline 4 & -20 & 4 \\ \hline 1 & 4 & 1 \end{array} \rightarrow \frac{1}{6h^2} \left[\begin{array}{c|c|c} 0 & 4 & 2 \\ \hline 0 & -20 & 8 \\ \hline 0 & 4 & 2 \end{array} - 2h\cos(\theta)(|\nabla\eta|_{0,j+1} + |\nabla\eta|_{0,j-1} + 4|\nabla\eta|_{0,j}) \right] \quad (\text{D.27})$$

or e.g. at the top boundary

$$\frac{1}{6h^2} \begin{array}{c|c|c} 1 & 4 & 1 \\ \hline 4 & -20 & 4 \\ \hline 1 & 4 & 1 \end{array} \rightarrow \frac{1}{6h^2} \left[\begin{array}{c|c|c} 0 & 0 & 0 \\ \hline 4 & -20 & 4 \\ \hline 2 & 8 & 2 \end{array} + 2h\cos(\theta)(|\nabla\eta|_{i+1,M} + |\nabla\eta|_{i-1,M} + 4|\nabla\eta|_{i,M}) \right] \quad (\text{D.28})$$

D.4.3 Mixed boundary conditions

Imagine the system with BCs as indicated in figure D.3. The action of the finite

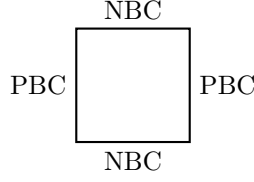


Figure D.3: Layout of the mixed boundaries. NBC and PBC stand for Neumann and periodic boundary conditions, respectively.

difference matrix in the y-direction is given by the structure of the individual block matrices and the x-direction by the arrangement of the blocks in the large matrix.

Specifically, with the periodic BCs present in the x-direction, the structure of the large matrix is as with periodic BCs only the diagonal block matrix. Showing on the example of the 5pt laplacian approximation with mixed BCs as in the figure D.3

$$\mathbb{L}_{PN}^{5p} = \frac{1}{h^2} \begin{pmatrix} \mathbb{D}_N^{5p} & \mathbb{I} & \mathbb{O} & \mathbb{O} & \dots & \mathbb{O} & \mathbb{O} & \textcolor{red}{\mathbb{I}} \\ \mathbb{I} & \mathbb{D}_N^{5p} & \mathbb{I} & \mathbb{O} & \dots & \mathbb{O} & \mathbb{O} & \mathbb{O} \\ \mathbb{O} & \mathbb{I} & \mathbb{D}_N^{5p} & \mathbb{I} & \dots & \mathbb{O} & \mathbb{O} & \mathbb{O} \\ \vdots & \vdots & \vdots & \vdots & \ddots & \vdots & \vdots & \vdots \\ \mathbb{O} & \mathbb{O} & \mathbb{O} & \mathbb{O} & \dots & \mathbb{I} & \mathbb{D}_N^{5p} & \mathbb{I} \\ \textcolor{red}{\mathbb{I}} & \mathbb{O} & \mathbb{O} & \mathbb{O} & \dots & \mathbb{O} & \mathbb{I} & \mathbb{D}_N^{5p} \end{pmatrix} \quad (\text{D.29})$$

In the 9p20 scheme the finite difference matrix is

$$\mathbb{L}_{PN}^{9p20} = \frac{1}{6h^2} \begin{pmatrix} \mathbb{D}_N^{9p20} & \mathbb{A} & \mathbb{O} & \mathbb{O} & \dots & \mathbb{O} & \mathbb{O} & \textcolor{red}{\mathbb{A}} \\ \mathbb{A} & \mathbb{D}_N^{9p20} & \mathbb{A} & \mathbb{O} & \dots & \mathbb{O} & \mathbb{O} & \mathbb{O} \\ \mathbb{O} & \mathbb{A} & \mathbb{D}_N^{9p20} & \mathbb{A} & \dots & \mathbb{O} & \mathbb{O} & \mathbb{O} \\ \vdots & \vdots & \vdots & \vdots & \ddots & \vdots & \vdots & \vdots \\ \mathbb{O} & \mathbb{O} & \mathbb{O} & \mathbb{O} & \dots & \mathbb{A} & \mathbb{D}_N^{9p20} & \mathbb{A} \\ \textcolor{red}{\mathbb{A}} & \mathbb{O} & \mathbb{O} & \mathbb{O} & \dots & \mathbb{O} & \mathbb{A} & \mathbb{D}_N^{9p20} \end{pmatrix} \quad (\text{D.30})$$

D.5 Anisotropic driving force terms

In phase field method, usually it is better to keep the interface away from the domain boundary as the boundary conditions often impose specific, non-physical behavior of the interface. In the case of general NBC and the intended use for

the energy assessment, the proximity of interface to the domain boundary is deliberate.

In the implementation of the inclination-dependent model, the anisotropic driving force terms are calculated from numeric derivatives of various fields. Care must be taken to each of the numerical derivative in order to assure the control over the interface inclination at the domain boundary.

When the interface inclination is fixed, the anisotropic driving force terms have fixed value (Dirichlet BC). Some of these fields are numerically differentiated again. However, their values at the ghost nodes are unknown (to be used in centered finite difference), hence one-sided FD scheme must be used at the boundaries. In order to keep second-order accuracy at the boundaries, the

following backward $\begin{array}{|c|} \hline 1/2 \\ \hline -2 \\ \hline 3/2 \\ \hline \end{array}$ and forward $\begin{array}{|c|} \hline -3/2 \\ \hline 2 \\ \hline -1/2 \\ \hline \end{array}$ FD schemes were used at the bottom and top boundary, respectively.

For the x-direction derivative the FD matrix is

$$\frac{\partial}{\partial x} \approx \Delta_x = \frac{1}{2h} \begin{pmatrix} -3\mathbb{I} & 4\mathbb{I} & -\mathbb{I} & \mathbb{O} & \dots & \mathbb{O} & \mathbb{O} & \mathbb{O} \\ -\mathbb{I} & \mathbb{O} & \mathbb{I} & \mathbb{O} & \dots & \mathbb{O} & \mathbb{O} & \mathbb{O} \\ \mathbb{O} & -\mathbb{I} & \mathbb{O} & \mathbb{I} & \dots & \mathbb{O} & \mathbb{O} & \mathbb{O} \\ \vdots & \vdots & \vdots & \ddots & \vdots & \vdots & \vdots & \vdots \\ \mathbb{O} & \mathbb{O} & \mathbb{O} & \mathbb{O} & \dots & -\mathbb{I} & \mathbb{O} & \mathbb{I} \\ \mathbb{O} & \mathbb{O} & \mathbb{O} & \dots & \mathbb{O} & \mathbb{I} & -4\mathbb{I} & 3\mathbb{I} \end{pmatrix}. \quad (\text{D.31})$$

For the y-direction derivative the FD matrix is

$$\frac{\partial}{\partial y} \approx \Delta_y = \frac{1}{h} \begin{pmatrix} \mathbb{Y} & \mathbb{O} & \mathbb{O} & \dots & \mathbb{O} & \mathbb{O} \\ \mathbb{O} & \mathbb{Y} & \mathbb{O} & \dots & \mathbb{O} & \mathbb{O} \\ \mathbb{O} & \mathbb{O} & \mathbb{Y} & \dots & \mathbb{O} & \mathbb{O} \\ \vdots & \vdots & \vdots & \ddots & \vdots & \vdots \\ \mathbb{O} & \mathbb{O} & \mathbb{O} & \dots & \mathbb{Y} & \mathbb{O} \\ \mathbb{O} & \mathbb{O} & \mathbb{O} & \dots & \mathbb{O} & \mathbb{Y} \end{pmatrix} \quad (\text{D.32})$$

with

$$\mathbb{Y} = \begin{pmatrix} -3/2 & 2 & -1/2 & 0 & \dots & 0 & 0 & 0 \\ -1 & 0 & 1 & 0 & \dots & 0 & 0 & 0 \\ 0 & -1 & 0 & 1 & \dots & 0 & 0 & 0 \\ \vdots & \vdots & \vdots & \ddots & \vdots & \vdots & \vdots & \vdots \\ 0 & 0 & 0 & 0 & \dots & -1 & 0 & 1 \\ 0 & 0 & 0 & 0 & \dots & 1/2 & -2 & 3/2 \end{pmatrix} \quad (\text{D.33})$$

Appendix E

Volume conservation using Lagrange multipliers

E.1 Phase field equations under equality constraint - Lagrange multipliers

In multivariate calculus, the method of Lagrange multipliers is used to find extrema of a multivariate function under equality constraint, i.e. on a subset of its domain. For example, the extrema of the function $f(x, y)$ over the subset of the domain defined as $g(x, y) = 0$ can be found by analysis of the so-called Lagrange function $\mathcal{L}(x, y, \lambda) = f(x, y) - \lambda g(x, y)$, where λ is the Lagrange multiplier. The critical points are found by solving the set of equations

$$\frac{\partial \mathcal{L}}{\partial x} = 0, \quad \frac{\partial \mathcal{L}}{\partial y} = 0, \quad \frac{\partial \mathcal{L}}{\partial \lambda} = 0. \quad (\text{E.1})$$

Similar principles can be generalized in functional calculus. Let's have a functional of free energy $F[\phi] = \int f(\phi, \nabla \phi) dV$ with equality constraint $G[\phi] =$

$\int g(\phi)dV = 0$. The Lagrangian now takes the form

$$\Lambda[\phi, \lambda] = F[\phi] - \lambda G[\phi] \quad (\text{E.2})$$

$$= \int f(\phi, \nabla\phi) - \lambda g(\phi)dV \quad (\text{E.3})$$

$$= \int l(\phi)dV, \quad (\text{E.4})$$

where $l(\phi)$ is the lagrangian energy density and $\lambda(t)$ is the Lagrange multiplier. It is a function of time, because its value is related to the state of the evolving system. When the phase field $\phi(\mathbf{r})$ evolves due to governing equations

$$\frac{\partial\phi}{\partial t} = \frac{\delta\Lambda}{\delta\phi}, \quad (\text{E.5})$$

the equality constraint $G[\phi] = \int g(\phi)dV = 0$ will hold throughout the simulation. The constraint can e.g. impose some conservation law¹, or enforce local sum of values of phase fields in a multi-phase field model like in all multi-phase field models in the legacy of [63].

The governing equations then read

$$\frac{\delta\Lambda}{\delta\phi} = \frac{\delta F}{\delta\phi} - \lambda(t) \frac{\partial g}{\partial\phi}, \quad (\text{E.6})$$

where it was assumed that the constraint is only functional of the phase field, not of its gradient. It can be seen that an additional term appeared, originating from the constraint.

Multiple constraints $G_1[\phi] = 0, G_2[\phi] = 0, \dots, G_p[\phi] = 0$ can be imposed on the system, each of which has its Lagrange multiplier $\lambda_1, \lambda_2, \dots, \lambda_p$. The Lagrangian is then

$$\Lambda[\phi, \lambda_1, \lambda_2, \dots, \lambda_p] = F[\phi] - \sum_i \lambda_i G_i[\phi], \quad (\text{E.7})$$

which leads to constrained governing equation

$$\frac{\delta\Lambda}{\delta\phi} = \frac{\delta F}{\delta\phi} - \sum_i \lambda_i(t) \frac{\partial g_i}{\partial\phi}, \quad (\text{E.8})$$

where $g_i(\phi)$ is the kernel of i -th constraint $G_i[\phi] = \int g_i(\phi)dV$.

¹typically volume, but e.g. in [21, 22] electric charge and behavior of other physical quantities were controlled by Lagrange multipliers

E.2 Lagrange multipliers for volume conservation in multi-phase field models

This approach allows to mathematically enforce certain behavior of the evolving fields. Volume conservation in Allen-Cahn equation is a typical application.

Moelans' model is a multi phase field model with non-conserved fields and with curvature-driven interfaces motion. Inspired by [52], an extension of this model is hereby proposed, which allows to conserve volume of selected phase fields.

The model by Nestler et al. [52] is an extension of a phase field model which differs from the Moelans' one in several aspects. The main difference is that the sum of all the phase fields locally is equal to 1, which allows to interpret them as order parameters in the strict mathematical sense. However, this comes with a cost - this model property is imposed using a suitable Lagrange multiplier, which introduces new terms in the governing equation(s). Moreover, every model extension must be such that this property is preserved. Nestler's model also differs in the double obstacle potential and in the choice of the non-local gradient term.

E.2.1 Concept - single conserved phase field

The simulated system over the domain Ω consists of n phase fields $\vec{\eta} = (\eta_1, \dots, \eta_n)$ and is described by the free energy functional F with free energy density $f(\vec{\eta}, \nabla \vec{\eta})$ being also function of the phase fields gradients $\nabla \vec{\eta} = (\nabla \eta_1, \dots, \nabla \eta_n)$ as is usual in phase field method

$$F = \int_{\Omega} f(\vec{\eta}, \nabla \vec{\eta}) dV \quad (\text{E.9})$$

The volume V_i occupied by i -th grain η_i in the domain Ω can be expressed in Moelans' model as

$$V_i = \int_{\Omega} \Phi_i(\vec{\eta}) dV, \quad (\text{E.10})$$

where $\Phi_i(\vec{\eta})$ is the i -th grain expressed using the special interpolation function [50]

$$\Phi_i(\vec{\eta}) = \frac{\eta_i^2}{\sum_k \eta_k^2}. \quad (\text{E.11})$$

The equality constraint $G = 0$ which conserves volume of η_i can be formulated as

$$G = \int \Phi_i(\vec{\eta}) dV - V_i^0, \quad (\text{E.12})$$

where V_i^0 is the initial volume of the phase field. Because the constant V_i^0 plays no role in the governing equation, it will be disregarded. The volume conservation is ensured by deriving the governing equations from Lagrangian

$$\Lambda[\vec{\eta}] = \int f(\vec{\eta}, \nabla \vec{\eta}) - \lambda(t) \Phi_i(\vec{\eta}) dV, \quad (\text{E.13})$$

leading to equation for any p -th phase field

$$\frac{\partial \eta_p}{\partial t} = \frac{\delta \Lambda}{\delta \eta_p} \quad (\text{E.14})$$

$$= \frac{\delta F}{\delta \eta_p} - \lambda(t) \frac{\partial \Phi_i}{\partial \eta_p}. \quad (\text{E.15})$$

Expression for the Lagrange multiplier $\lambda(t)$ is obtained from the constraint itself, as the volume conservation of η_i implies

$$\frac{dV_i}{dt} = 0 = \frac{\partial}{\partial t} \int \Phi_i(\vec{\eta}) dV \quad (\text{E.16})$$

$$= \int \frac{\partial \Phi_i}{\partial t} dV \quad (\text{E.17})$$

$$= \int \sum_{k=1}^n \frac{\partial \Phi_i}{\partial \eta_k} \frac{\partial \eta_k}{\partial t} dV \quad (\text{E.18})$$

$$= -L \int \sum_{k=1}^n \frac{\partial \Phi_i}{\partial \eta_k} \left[\frac{\delta F}{\delta \eta_k} - \lambda(t) \frac{\partial \Phi_i}{\partial \eta_k} \right] dV. \quad (\text{E.19})$$

In the last equation, $\lambda(t)$ can already be taken out of the integral as it is not function of space, allowing to write

$$\lambda(t) = \frac{\int \sum_{k=1}^n \frac{\partial \Phi_i}{\partial \eta_k} \frac{\delta F}{\delta \eta_p} dV}{\int \sum_{k=1}^n \left(\frac{\partial \Phi_i}{\partial \eta_k} \right)^2 dV}. \quad (\text{E.20})$$

As can be seen, the expression is notably more complicated than in the original model by Nestler. One reason is that the interpolation function $\Phi(\vec{\eta})$ is a function of all the phase fields, whereas in Nestler the interpolation function $p_k = p_k(\eta_k)$ only. The second reason is that in Nestler's model the volume evolution can be expressed as $dV_i/dt = \partial \eta_i / \partial t$. In comparison to Nestler's model, the first complication adds the sum over all phase fields to the integrals and the second adds the term $\partial \Phi_i / \partial \eta_k$.

E.2.2 Multiple conserved phase fields

Hereby the case when all the phase fields are conserved is discussed. With n phase fields that implies $n - 1$ constraints $G_i = \int \Phi_i(\vec{\eta}) dV = 0$ as the n -th phase field must be conserved as well when all the others are. Without the loss of generality it is assumed that the n -th phase field does not have its constraint. The Lagrangian is

$$\Lambda[\vec{\eta}] = \int_{\Omega} f(\vec{\eta}, \nabla \vec{\eta}) - \sum_{l=1}^{n-1} \lambda_l(t) \Phi_l(\vec{\eta}) dV, \quad (\text{E.21})$$

with $\lambda_l(t)$ being the Lagrange multiplier corresponding to l -th phase field.

Each governing equation can then be written in the form

$$\frac{\partial \eta_p}{\partial t} = \frac{\delta \Lambda}{\delta \eta_p} \quad (\text{E.22})$$

$$= \frac{\delta F}{\delta \eta_p} - \sum_{l=1}^{n-1} \lambda_l(t) \frac{\partial \Phi_l}{\partial \eta_p}. \quad (\text{E.23})$$

The individual Lagrange multipliers are determined from equation analogical to (E.16), i.e. for arbitrary i

$$\frac{dV_i}{dt} = 0 = \int \sum_{k=1}^n \frac{\partial \Phi_i}{\partial \eta_k} \frac{\partial \eta_k}{\partial t} dV \quad (\text{E.24})$$

$$= -L \int \sum_{k=1}^n \frac{\partial \Phi_i}{\partial \eta_k} \left[\frac{\delta F}{\delta \eta_k} - \sum_{l=1}^{n-1} \lambda_l(t) \frac{\partial \Phi_l}{\partial \eta_k} \right] dV. \quad (\text{E.25})$$

This equation can be rearranged to give

$$\int \sum_{k=1}^n \frac{\partial \Phi_i}{\partial \eta_k} \frac{\delta F}{\delta \eta_k} dV = \sum_{l=1}^{n-1} \lambda_l(t) \int \sum_{k=1}^n \frac{\partial \Phi_i}{\partial \eta_k} \frac{\partial \Phi_l}{\partial \eta_k} dV, \quad (\text{E.26})$$

which is a linear equation for $n - 1$ variables $\lambda_l(t)$. Because such equation can be written for every i of the $n - 1$ constrained phase fields, it is a system of linear algebraic equations which can be compactly described using the following notation

$$b_i = \int \sum_{k=1}^n \frac{\partial \Phi_i}{\partial \eta_k} \frac{\delta F}{\delta \eta_k} dV \quad (\text{E.27})$$

$$A_{il} = \int \sum_{k=1}^n \frac{\partial \Phi_i}{\partial \eta_k} \frac{\partial \Phi_l}{\partial \eta_k} dV, \quad (\text{E.28})$$

where b_i is a component of a vector \mathbf{b} and A_{il} is a component of the matrix \mathbf{A} . Denoting the vector with variables $\boldsymbol{\lambda}$, the system of $n - 1$ equations for $n - 1$ variables can be written

$$\mathbf{A}\boldsymbol{\lambda} = \mathbf{b}. \quad (\text{E.29})$$

Evaluation of this system is computationally very expensive, because in every component of both \mathbf{b} and \mathbf{A} there is the sum over all n phase fields. Moreover, it must be evaluated at every time step and it is expected, that all the components of \mathbf{A} are non-zero. Even though the matrix is symmetric, the model does not seem to be practical for use in simulations with many conserved grains.

Bibliography

- [1] F. Abdeljawad, S. M. Foiles, A. P. Moore, A. R. Hinkle, C. M. Barr, N. M. Heckman, K. Hattar, and B. L. Boyce. “The role of the interface stiffness tensor on grain boundary dynamics”. In: *Acta Materialia* 158 (Oct. 2018), pp. 440–453. ISSN: 1359-6454. DOI: 10.1016/J.ACTAMAT.2018.06.025. URL: <https://www-sciencedirect-com.kuleuven.ezproxy.kuleuven.be/science/article/pii/S1359645418304932>.
- [2] H. Alimadadi, A. B. Fanta, T. Kasama, M. A. Somers, and K. Pantleon. “Texture and microstructure evolution in nickel electrodeposited from an additive-free Watts electrolyte”. In: *Surface and Coatings Technology* 299 (Aug. 2016), pp. 1–6. ISSN: 02578972. DOI: 10.1016/j.surfcoat.2016.04.068.
- [3] H. Alt, C. Knauer, and C. Wenk. “Comparison of Distance Measures for Planar Curves”. In: *Algorithmica* 38.1 (Jan. 2004), pp. 45–58. ISSN: 0178-4617. DOI: 10.1007/s00453-003-1042-5. URL: <http://link.springer.com/10.1007/s00453-003-1042-5>.
- [4] J. Amblard, I. Epelboin, M. Froment, and G. Maurin. “Inhibition and nickel electrocrystallization”. In: *Journal of Applied Electrochemistry* 9 (2 Mar. 1979), pp. 233–242. ISSN: 0021-891X. DOI: 10.1007/BF00616093.
- [5] W. Bao, W. Jiang, D. J. Srolovitz, and Y. Wang. “Stable Equilibria of Anisotropic Particles on Substrates: A Generalized Winterbottom Construction”. In: *SIAM Journal on Applied Mathematics* 77 (6 Jan. 2017), pp. 2093–2118. ISSN: 0036-1399. DOI: 10.1137/16M1091599.
- [6] I. Bellemans, N. Moelans, and K. Verbeken. “Phase-Field Modelling in Extractive Metallurgy”. In: *Critical Reviews in Solid State and Materials Sciences* 0 (0 2017), pp. 1–38. ISSN: 1040-8436. DOI: 10.1080/10408436.2017.1397500.
- [7] G. Bellettini and M. Paolini. “Anisotropic motion by mean curvature in the context of finsler geometry”. In: *Hokkaido Mathematical Journal* 25.3 (1996), pp. 537–566. ISSN: 03854035. DOI: 10.14492/hokmj/1351516749.

- [8] M. Beneš. “Diffuse-interface treatment of the anisotropic mean-curvature flow”. In: *Applications of Mathematics* 48.6 (2003), pp. 437–453. ISSN: 08627940. DOI: 10.1023/B:APOM.0000024485.24886.b9.
- [9] V. V. Bulatov, B. W. Reed, and M. Kumar. “Grain boundary energy function for fcc metals”. In: *Acta Materialia* 65 (2014), pp. 161–175. ISSN: 13596454. DOI: 10.1016/j.actamat.2013.10.057. URL: <http://dx.doi.org/10.1016/j.actamat.2013.10.057>.
- [10] W. K. Burton, N. Cabrera, and F. C. Frank. “The Growth of Crystals and the Equilibrium Structure of their Surfaces”. In: *Philosophical Transactions of the Royal Society A: Mathematical, Physical and Engineering Sciences* 243.866 (1951), pp. 299–358. ISSN: 1364-503X. DOI: 10.1098/rsta.1951.0006.
- [11] J. Cahn and D. Hoffman. “A vector thermodynamics for anisotropic surfaces—II. Curved and faceted surfaces”. In: *Acta Metallurgica* 22.10 (Oct. 1974), pp. 1205–1214. ISSN: 00016160. DOI: 10.1016/0001-6160(74)90134-5. URL: <https://linkinghub.elsevier.com/retrieve/pii/0001616074901345>.
- [12] L. Chen, H. W. Zhang, L. Y. Liang, Z. Liu, Y. Qi, P. Lu, J. Chen, and L. Q. Chen. “Modulation of dendritic patterns during electrodeposition: A nonlinear phase-field model”. In: *Journal of Power Sources* 300 (2015), pp. 376–385. ISSN: 03787753. DOI: 10.1016/j.jpowsour.2015.09.055. URL: <http://dx.doi.org/10.1016/j.jpowsour.2015.09.055>.
- [13] L.-Q. Chen and W. Yang. “Computer simulation of the domain dynamics of a quenched system with a large number of nonconserved order parameters: The grain-growth kinetics”. In: *Physical Review B* 50 (21 Dec. 1994), pp. 15752–15756. ISSN: 0163-1829. DOI: 10.1103/PhysRevB.50.15752. URL: <https://link.aps.org/doi/10.1103/PhysRevB.50.15752>.
- [14] V. Consonni, G. Feullet, and P. Gergaud. “The flow stress in polycrystalline films: Dimensional constraints and strengthening effects”. In: *Acta Materialia* 56 (20 Dec. 2008), pp. 6087–6096. ISSN: 1359-6454. DOI: 10.1016/J.ACTAMAT.2008.08.019.
- [15] S. Daubner, P. W. Hoffrogge, M. Minar, and B. Nestler. “Triple junction benchmark for multiphase-field and multi-order parameter models”. In: *Computational Materials Science* 219 (Feb. 2023). ISSN: 09270256. DOI: 10.1016/j.commatsci.2022.111995.
- [16] J. M. Debievre, A. Karma, F. Celestini, and R. Guérin. “Phase-field approach for faceted solidification”. In: *Physical Review E* 68.4 (2003), pp. 1–13. ISSN: 1063651X. DOI: 10.1103/PhysRevE.68.041604. arXiv: 0302368 [cond-mat].

- [17] J. Eggleston, G. McFadden, and P. Voorhees. “A phase-field model for highly anisotropic interfacial energy”. In: *Physica D: Nonlinear Phenomena* 150.1-2 (Mar. 2001), pp. 91–103. ISSN: 01672789. DOI: 10.1016/S0167-2789(00)00222-0. URL: <https://linkinghub.elsevier.com/retrieve/pii/S0167278900002220>.
- [18] M. Fleck, L. Mushongera, D. Pilipenko, K. Ankit, and H. Emmerich. “On phase-field modeling with a highly anisotropic interfacial energy”. In: *The European Physical Journal Plus* 126.10 (Oct. 2011), p. 95. ISSN: 2190-5444. DOI: 10.1140/epjp/i2011-11095-7. URL: <http://link.springer.com/10.1140/epjp/i2011-11095-7>.
- [19] H. Garcke, B. Stoth, and B. Nestler. “Anisotropy in multi-phase systems: a phase field approach”. In: *Interfaces and Free Boundaries* 1.2 (1999), pp. 175–198. ISSN: 1463-9963. DOI: 10.4171/IFB/8. URL: <http://www.ems-ph.org/doi/10.4171/IFB/8>.
- [20] L. Gránásy, T. Pusztai, D. Saylor, and J. A. Warren. “Phase Field Theory of Heterogeneous Crystal Nucleation”. In: *Physical Review Letters* 98 (3 Jan. 2007), p. 035703. ISSN: 0031-9007. DOI: 10.1103/PhysRevLett.98.035703. URL: <https://link.aps.org/doi/10.1103/PhysRevLett.98.035703>.
- [21] J. E. Guyer, W. J. Boettinger, J. A. Warren, and G. B. McFadden. “Phase field modeling of electrochemistry. I. Equilibrium”. In: *Physical Review E* 69 (2 Feb. 2004), p. 021603. ISSN: 1539-3755. DOI: 10.1103/PhysRevE.69.021603. URL: <https://link.aps.org/doi/10.1103/PhysRevE.69.021603>.
- [22] J. E. Guyer, W. J. Boettinger, J. A. Warren, and G. B. McFadden. “Phase field modeling of electrochemistry. II. Kinetics”. In: *Physical Review E* 69 (2 Feb. 2004), p. 021604. ISSN: 1539-3755. DOI: 10.1103/PhysRevE.69.021604. URL: <http://arxiv.org/abs/cond-mat/0308179><http://dx.doi.org/10.1103/PhysRevE.69.021604><https://link.aps.org/doi/10.1103/PhysRevE.69.021604>.
- [23] D. W. Hoffman and J. W. Cahn. “A vector thermodynamics for anisotropic surfaces. I. Fundamentals and application to plane surface junctions”. In: *Surface Science* 31.C (1972), pp. 368–388. ISSN: 00396028. DOI: 10.1016/0039-6028(72)90268-3.
- [24] C. A. Johnson. “Generalization of the Gibbs-Thomson equation”. In: *Surface Science* 3 (5 Dec. 1965), pp. 429–444. ISSN: 0039-6028. DOI: 10.1016/0039-6028(65)90024-5.

- [25] A. Jokisaari, P. Voorhees, J. Guyer, J. Warren, and O. Heinonen. “Benchmark problems for numerical implementations of phase field models”. In: *Computational Materials Science* 126 (Jan. 2017), pp. 139–151. ISSN: 0927-0256. DOI: 10.1016/J.COMMATSCI.2016.09.022. URL: <https://www.sciencedirect.com/science/article/pii/S0927025616304712>.
- [26] A. Kazaryan, Y. Wang, and S. Dregia. “Generalized phase-field model for computer simulation of grain growth in anisotropic systems”. In: *Physical Review B - Condensed Matter and Materials Physics* 61.21 (2000), pp. 14275–14278. ISSN: 1550235X. DOI: 10.1103/PhysRevB.61.14275. arXiv: 9912044 [cond-mat].
- [27] W. E. Kingston. *The Physics of Powder Metallurgy: A Symposium Held at Bayside, LI, New York, August 24-26, 1949*. McGraw-Hill, 1951, p. 143.
- [28] R. Kobayashi. “Modeling and numerical simulations of dendritic crystal growth”. In: *Physica D* 63 (1993), pp. 410–423. ISSN: 01672789. DOI: 10.1016/0167-2789(93)90120-P.
- [29] R. Kobayashi and Y. Giga. “On Anisotropy and Curvature Effects for Growing Crystals”. In: *Japan Journal of Industrial and Applied Mathematics* 18.2 (2001), pp. 207–230. ISSN: 09167005. DOI: 10.1007/BF03168571.
- [30] V. Kozlov and L. P. Bicelli. “Texture formation of electrodeposited fcc metals”. In: *Materials Chemistry and Physics* 77 (1 Jan. 2003), pp. 289–293. ISSN: 02540584. DOI: 10.1016/S0254-0584(02)00004-4.
- [31] D. Li and J. Szpunar. “A Monte Carlo simulation approach to the texture formation during electrodeposition—I. The simulation model”. In: *Electrochimica Acta* 42 (1 Jan. 1997), pp. 37–45. ISSN: 00134686. DOI: 10.1016/0013-4686(96)00164-8.
- [32] D. Li and J. Szpunar. “A Monte Carlo simulation approach to the texture formation during electrodeposition—II. Simulation and experiment”. In: *Electrochimica Acta* 42 (1 Jan. 1997), pp. 47–60. ISSN: 00134686. DOI: 10.1016/0013-4686(96)00158-2.
- [33] Li Zhu and Chun-qiang Zhu. “Application of Hausdorff distance in image matching”. In: *2014 IEEE Workshop on Electronics, Computer and Applications*. 3. IEEE, May 2014, pp. 97–100. ISBN: 978-1-4799-4565-8. DOI: 10.1109/IWECA.2014.6845566. URL: <http://ieeexplore.ieee.org/document/6845566/>.
- [34] I. Loginova, J. Ågren, and G. Amberg. “On the formation of Widmanstätten ferrite in binary Fe–C – phase-field approach”. In: *Acta Materialia* 52.13 (Aug. 2004), pp. 4055–4063. ISSN: 13596454. DOI: 10.1016/j.actamat.2004.05.033. URL: <https://linkinghub.elsevier.com/retrieve/pii/S1359645404002952>.

- [35] N. Ma, Q. Chen, and Y. Wang. "Implementation of high interfacial energy anisotropy in phase field simulations". In: *Scripta Materialia* 54.11 (June 2006), pp. 1919–1924. ISSN: 1359-6462. DOI: 10.1016/J.SCRIPMAT.2006.02.005. URL: <https://www.sciencedirect.com/science/article/pii/S1359646206001266>.
- [36] A. Mariaux and M. Rappaz. "Influence of anisotropy on heterogeneous nucleation". In: *Acta Materialia* 59 (3 2011), pp. 927–933. ISSN: 1359-6454. DOI: 10.1016/j.actamat.2010.10.015.
- [37] R. A. Marks and A. M. Glaeser. "Equilibrium and stability of triple junctions in anisotropic systems". In: *Acta Materialia* 60.1 (2012), pp. 349–358. ISSN: 1359-6454. DOI: 10.1016/j.actamat.2011.09.043. URL: <http://dx.doi.org/10.1016/j.actamat.2011.09.043>.
- [38] G. B. McFadden, A. A. Wheeler, R. J. Braun, S. R. Coriell, and R. F. Sekerka. "Phase-field models for anisotropic interfaces". In: *Physical Review E* 48.3 (Sept. 1993), pp. 2016–2024. ISSN: 1063-651X. DOI: 10.1103/PhysRevE.48.2016. URL: <https://link.aps.org/doi/10.1103/PhysRevE.48.2016>.
- [39] A. Milchev. *Electrocrystallization: fundamentals of nucleation and growth*. Kluwer Academic Publishers, 2002. ISBN: 1-4020-7090-X. DOI: 10.1007/b113784.
- [40] M. Minar. "Benchmarking of different strategies to include anisotropy in a curvature-driven multi-phase-field model". In: *Mendeley Data, v2* (2022). DOI: 10.17632/5wrv3ky9pp.2. URL: <http://dx.doi.org/10.17632/5wrv3ky9pp.2>.
- [41] M. Minar. "Influence of surface energy anisotropy on nucleation and crystallographic texture of polycrystalline deposits". In: *Mendeley Data, v1* (2023). DOI: 10.17632/bsdff8shbz.1.
- [42] M. Minar and N. Moelans. "Benchmarking of different strategies to include anisotropy in a curvature-driven multi-phase-field model". In: *Physical Review Materials* 6 (10 Oct. 2022), p. 103404. ISSN: 2475-9953. DOI: 10.1103/PhysRevMaterials.6.103404. URL: <https://link.aps.org/doi/10.1103/PhysRevMaterials.6.103404>.
- [43] M. Minar and N. Moelans. "Influence of surface energy anisotropy on nucleation and crystallographic texture of polycrystalline deposits". In: *Computational Materials Science* 231 (Jan. 2024), p. 112575. ISSN: 0927-0256. DOI: 10.1016/J.COMMATSCI.2023.112575. URL: <https://www.sciencedirect.com/science/article/abs/pii/S0927025623005694>.
- [44] M. Minar and N. Moelans. "See Supplemental material at xxx for the best practices in parameters determination in Moelans' model and for further details on the implementation." In: *Phys.Rev.Mat.* (2022).

- [45] H. Miura. “Anisotropy function of kinetic coefficient for phase-field simulations: Reproduction of kinetic Wulff shape with arbitrary face angles”. In: *Journal of Crystal Growth* 367 (2013), pp. 8–17. ISSN: 00220248. DOI: 10.1016/j.jcrysgro.2013.01.014. URL: <http://dx.doi.org/10.1016/j.jcrysgro.2013.01.014>.
- [46] E. Miyoshi, T. Takaki, M. Ohno, and Y. Shibuta. “Accuracy evaluation of phase-field models for grain growth simulation with anisotropic grain boundary properties”. In: *ISIJ International* 60.1 (2020), pp. 160–167. ISSN: 09151559. DOI: 10.2355/isijinternational.ISIJINT-2019-305.
- [47] N. Moelans, B. Blanpain, and P. Wollants. “Quantitative analysis of grain boundary properties in a generalized phase field model for grain growth in anisotropic systems”. In: *Physical Review B - Condensed Matter and Materials Physics* 78.2 (2008). ISSN: 10980121. DOI: 10.1103/PhysRevB.78.024113.
- [48] N. Moelans, F. Spaepen, and P. Wollants. “Grain growth in thin films with a fibre texture studied by phase-field simulations and mean field modelling”. In: *Philosophical Magazine* 90.1-4 (2010), pp. 501–523. ISSN: 14786435. DOI: 10.1080/14786430902998129.
- [49] N. Moelans, F. Spaepen, and P. Wollants. “Grain growth in thin films with a fibre texture studied by phase-field simulations and mean field modelling”. In: *Philosophical Magazine* 90.1-4 (2010), pp. 501–523. ISSN: 14786435. DOI: 10.1080/14786430902998129.
- [50] N. Moelans. “A quantitative and thermodynamically consistent phase-field interpolation function for multi-phase systems”. In: *Acta Materialia* 59.3 (2011), pp. 1077–1086. ISSN: 13596454. URL: <http://dx.doi.org/10.1016/j.actamat.2010.10.038>.
- [51] N. Moelans, F. Wendler, and B. Nestler. “Comparative study of two phase-field models for grain growth”. In: *Computational Materials Science* 46.2 (2009), pp. 479–490. ISSN: 0927-0256. DOI: 10.1016/j.commatsci.2009.03.037. URL: <http://dx.doi.org/10.1016/j.commatsci.2009.03.037>.
- [52] B. Nestler, F. Wendler, M. Selzer, B. Stinner, and H. Garcke. “Phase-field model for multiphase systems with preserved volume fractions”. In: *Physical Review E - Statistical, Nonlinear, and Soft Matter Physics* 78 (1 2008), pp. 1–7. ISSN: 15393755. DOI: 10.1103/PhysRevE.78.011604.
- [53] C. B. Nielsen, A. Horsewell, and M. J. Østergård. “On texture formation of nickel electrodeposits”. In: *Journal of Applied Electrochemistry* 27 (7 1997), pp. 839–845. ISSN: 0021891X. DOI: 10.1023/A:1018429013660.

- [54] D. L. Olmsted, S. M. Foiles, and E. A. Holm. "Survey of computed grain boundary properties in face-centered cubic metals: I. Grain boundary energy". In: *Acta Materialia* 57.13 (2009), pp. 3694–3703. ISSN: 13596454. DOI: 10.1016/j.actamat.2009.04.007. URL: <http://dx.doi.org/10.1016/j.actamat.2009.04.007>.
- [55] N. A. Pangarov. "On the crystal orientation of electrodeposited metals". In: *Electrochimica Acta* 9 (6 1964), pp. 721–726. ISSN: 00134686. DOI: 10.1016/0013-4686(64)80060-8.
- [56] N. Pangarov. "The crystal orientation of electrodeposited metals". In: *Electrochimica Acta* 7 (1 Jan. 1962), pp. 139–146. ISSN: 00134686. DOI: 10.1016/0013-4686(62)80023-1.
- [57] D. A. Porter, K. E. Easterling, and K. E. Easterling. *Phase Transformations in Metals and Alloys (Revised Reprint)*. third. CRC Press, Feb. 2009. ISBN: 9780429112256. DOI: 10.1201/9781439883570. URL: <https://www.taylorfrancis.com/books/9781439883570>.
- [58] A. A. Rasmussen, J. A. Jensen, A. Horsewell, and M. A. Somers. "Microstructure in electrodeposited copper layers; the role of the substrate". In: *Electrochimica Acta* 47 (1-2 Sept. 2001), pp. 67–74. ISSN: 00134686. DOI: 10.1016/S0013-4686(01)00583-7.
- [59] H. Ravash, J. Vleugels, and N. Moelans. "Three-dimensional phase-field simulation of microstructural evolution in three-phase materials with different interfacial energies and different diffusivities". In: *Journal of Materials Science* 52.24 (Dec. 2017), pp. 13852–13867. ISSN: 0022-2461. DOI: 10.1007/s10853-017-1465-z. URL: <http://link.springer.com/10.1007/s10853-017-1465-z>.
- [60] H. Salama, J. Kundin, O. Shchyglo, V. Mohles, K. Marquardt, and I. Steinbach. "Role of inclination dependence of grain boundary energy on the microstructure evolution during grain growth". In: *Acta Materialia* 188 (2020), pp. 641–651. ISSN: 13596454. DOI: 10.1016/j.actamat.2020.02.043. URL: <https://doi.org/10.1016/j.actamat.2020.02.043>.
- [61] J. Sanchez and E. Arzt. "Effects of grain orientation on hillock formation and grain growth in aluminum films on silicon substrates". In: *Scripta Metallurgica et Materialia* 27 (3 Aug. 1992), pp. 285–290. ISSN: 0956-716X. DOI: 10.1016/0956-716X(92)90513-E.
- [62] P. Sonnweber-Ribic, P. Gruber, G. Dehm, and E. Arzt. "Texture transition in Cu thin films: Electron backscatter diffraction vs. X-ray diffraction". In: *Acta Materialia* 54 (15 Sept. 2006), pp. 3863–3870. ISSN: 13596454. DOI: 10.1016/j.actamat.2006.03.057.

- [63] I. Steinbach, F. Pezzolla, B. Nestler, M. Sedlberg, R. G. J. Ptieler, and J. L. L. Rezende. “A phase field concept for multiphase systems”. In: *Physica D* 94 (1996), pp. 135–147. URL: [https://doi.org/10.1016/0167-2789\(95\)00298-7](https://doi.org/10.1016/0167-2789(95)00298-7).
- [64] J. E. Taylor and J. W. Cahn. “Diffuse interfaces with sharp corners and facets: Phase field models with strongly anisotropic surfaces”. In: *Physica D: Nonlinear Phenomena* 112.3-4 (Feb. 1998), pp. 381–411. ISSN: 01672789. DOI: 10.1016/S0167-2789(97)00177-2. URL: <https://linkinghub.elsevier.com/retrieve/pii/S0167278997001772>.
- [65] C. Thompson. “Texture evolution during grain growth in polycrystalline films”. In: *Scripta Metallurgica et Materialia* 28 (2 Jan. 1993), pp. 167–172. ISSN: 0956-716X. DOI: 10.1016/0956-716X(93)90557-9.
- [66] S. Torabi, J. Lowengrub, A. Voigt, and S. Wise. “A new phase-field model for strongly anisotropic systems”. In: *Proceedings of the Royal Society A: Mathematical, Physical and Engineering Sciences* 465.2105 (2009), pp. 1337–1359. ISSN: 14712946. DOI: 10.1098/rspa.2008.0385.
- [67] G. I. Tóth, T. Pusztai, and L. Gránásy. “Consistent multiphase-field theory for interface driven multidomain dynamics”. In: *Physical Review B - Condensed Matter and Materials Physics* 92.18 (2015), pp. 1–19. ISSN: 1550235X. DOI: 10.1103/PhysRevB.92.184105. arXiv: 1508.04311.
- [68] O. Tschukin, A. Silberzahn, M. Selzer, P. G. K. Amos, D. Schneider, and B. Nestler. “Concepts of modeling surface energy anisotropy in phase - field approaches”. In: *Geothermal Energy* (2017). ISSN: 2195-9706. DOI: 10.1186/s40517-017-0077-9.
- [69] F. Wendler, C. Mennerich, and B. Nestler. “A phase-field model for polycrystalline thin film growth”. In: *Journal of Crystal Growth* 327.1 (2011), pp. 189–201. ISSN: 00220248. DOI: 10.1016/j.jcrysgro.2011.04.044. URL: <http://dx.doi.org/10.1016/j.jcrysgro.2011.04.044>.
- [70] A. A. Wheeler. “Phase-field theory of edges in an anisotropic crystal”. In: *Proceedings of the Royal Society A: Mathematical, Physical and Engineering Sciences* 462.2075 (2006), pp. 3363–3384. ISSN: 14712946. DOI: 10.1098/rspa.2006.1721.
- [71] Wikipedia. *Modulo*. 2023. (Visited on 05/11/2023).
- [72] W. L. Winterbottom. “Equilibrium shape of a small particle in contact with a foreign substrate”. In: *Acta Metallurgica* 15 (2 1967), pp. 303–310. ISSN: 00016160. DOI: 10.1016/0001-6160(67)90206-4.
- [73] G. Wulff. “XXV. Zur Frage der Geschwindigkeit des Wachstums und der Auflösung der Krystallflächen”. In: *Zeitschrift für Kristallographie - Crystalline Materials* 34 (1-6 Dec. 1901), pp. 449–530. ISSN: 2196-7105. DOI: 10.1524/zkri.1901.34.1.449.

- [74] V. Yadav and N. Moelans. “Comparison of coarsening behaviour in non-conserved and volume-conserved isotropic two-phase grain structures”. In: *Scripta Materialia* 146 (2018), pp. 142–145. ISSN: 13596462. DOI: 10.1016/j.scriptamat.2017.11.023. URL: <https://doi.org/10.1016/j.scriptamat.2017.11.023>.
- [75] V. Yadav and N. Moelans. “Investigation on the existence of a ‘Hillert regime’ in normal grain growth”. In: *Scripta Materialia* 142 (Jan. 2018), pp. 148–152. ISSN: 1359-6462. DOI: 10.1016/J.SCRIPTAMAT.2017.08.036. URL: <https://www-sciencedirect-com.kuleuven.ezproxy.kuleuven.be/science/article/pii/S1359646217305006>.
- [76] V. Yadav, L. Vanherpe, and N. Moelans. “Effect of volume fractions on microstructure evolution in isotropic volume-conserved two-phase alloys: A phase-field study”. In: *Computational Materials Science* 125 (2016), pp. 297–308. ISSN: 09270256. DOI: 10.1016/j.commatsci.2016.08.037. URL: <http://dx.doi.org/10.1016/j.commatsci.2016.08.037>.
- [77] R. K. P. Zia, J. E. Avron, and J. E. Taylor. “The summertop construction: Crystals in a corner”. In: *Journal of Statistical Physics* 50 (3-4 Feb. 1988), pp. 727–736. ISSN: 0022-4715. DOI: 10.1007/BF01026498.

List of publications

First-author publications

[42] Minar, M., Moelans, N. (2022). Benchmarking of different strategies to include anisotropy in a curvature-driven multi-phase-field model. *Physical Review Materials*, 6(10), 103404.

<https://doi.org/10.1103/PhysRevMaterials.6.103404>

[43] Minar, M., Moelans, N. (2024). Influence of surface energy anisotropy on nucleation and crystallographic texture of polycrystalline deposits. *Computational Materials Science*, 231, 112575.

<https://doi.org/10.1016/J.COMMATSCI.2023.112575>

Collaborations

[15] Daubner, S., Hoffrogge, P. W., Minar, M., Nestler, B. (2023). Triple junction benchmark for multiphase-field and multi-order parameter models. *Computational Materials Science*, 219, 111995.

<https://doi.org/10.1016/J.COMMATSCI.2022.111995>